PB-230 851

# SULFATION KINETICS IN SULFUR DIOXIDE ABSORPTION FROM STACK GASSES

Stanford University

Prepared for:

Public Health Service

June 1972

DISTRIBUTED BY:

NTIS

National Technical Information Service
U. S. DEPARTMENT OF COMMERCE
5285 Port Royal Road, Springfield Va. 22151

# SULFATION KINETICS IN SULFUR DIOXIDE ABSORPTION FROM STACK GASES

ENVIRONMENTAL PROTECTION AGENCY

JUNE 1972



175

PB 230 851

# SULFATION KINETICS IN SULFUR DIOXIDE ABSORPTION FROM STACK GASES

Prepared by

PROCESS METALLURGY GROUP

DEPARTMENT OF MINERAL ENGINEERING

STANFORD UNIVERSITY

Stanford, California 94305

Grant No. AP 00876

Principal Investigator:

Prof. Robert W. Bartlett

Reproduced by
NATIONAL TECHNICAL
INFORMATION SERVICE
U S Department of Commerce
Springfield VA 22151

ENVIRONMENTAL PROTECTION AGENCY

Technical Center

Research Triangle Park, North Carolina

June, 1972

This report was furnished to the Environmental Protection Agency by Stanford University in Fulfillment of Grant Number AP 00876. The contents of this report are reproduced herein as received from the grantee. The opinions, findings, and conclusions are those of the authors and not necessarily those of the Environmental Protection Agency. Mention of company or product names does not constitute endorsement by the Environmental Protection Agency.

## ACKNOWLEDGMENTS

This investigation was conducted by Professor Robert W. Bartlett, principal investigator, Mr. N. Gopala Krishnan and Mr. Michel Van Hecke, research assistants and graduate students in the Process Metallurgy Group of the Department of Mineral Engineering at Stanford University. Electron beam microprobe examinations were conducted by Dr. Charles Taylor and the scanning electron microscopy was performed by Mr. Loren Anderson.

At the conclusion of this project Dr. Robert M. Bethea, Office of Engineering Analysis, Control Systems Division, Office of Air Programs, was the project officer.

CONTENTS


| | Page |
|---|---|
| LIST OF FIGURES | vii |
| LIST OF TABLES | xii |
| SUMMARY | xiii |
| INTRODUCTION | 1 |
| Background | 1 |
| Thermodynamic Considerations | 4 |
| Experimental Methods | 7 |
| References | 11 |
| KINETICS OF SULFATION OF ALKALIZED ALUMINA ($Na_2O \cdot Al_2O_3$) | 12 |
| Introduction | 12 |
| Preparation of Alkalized Alumina | 13 |
| Experimental | 15 |
| Results | 16 |
| Discussion of Results | 34 |
| Conclusions | 38 |
| Nomenclature | 40 |
| References | 41 |
| KINETICS OF SULFATION OF REDUCED ALUNITE ($K_2O \cdot 3Al_2O_3$) | 42 |
| Introduction | 42 |
| Materials and Experimental Method | 43 |
| Optimum Hydrogen Reduction of Alunite and Sorbent Regeneration | 43 |
| Sulfation Experimental Results | 48 |
| Temperature | 48 |
| Sulfur Dioxide Concentration | 50 |
| Oxygen Concentration | 53 |
| Water Vapor | 53 |
| Pellet Size | 56 |
| Discussion of Rate Mechanism Below 300°C - Sulfation of $K_2O$ | 56 |
| Discussion of Rate Mechanism Above 300°C - Sulfation of $K_2O$ and $Al_2O_3$ | 63 |
| Combined Rate Equation | 72 |

CONTENTS (continued)


| | Page |
|---|---|
| Conclusions | 72 |
| Nomenclature | 74 |
| References | 75 |
| KINETICS OF SULFATION OF ATLANTIC OCEAN MANGANESE NODULES | 76 |
| Introduction | 76 |
| Properties of Blake Plateau Atlantic Manganese Nodules | 77 |
| Experimental Procedure | 79 |
| Results and Discussion | 80 |
| Absorption Time Curves and Sorption Capacity | 80 |
| Extraction of Cu, Ni and Co | 85 |
| Experimental Kinetics | 85 |
| Particle Size and Pore Diffusion | 93 |
| Water Vapor | 93 |
| Oxygen | 95 |
| Conclusion | 99 |
| Nomenclature | 101 |
| References | 102 |
| KINETICS OF SULFATION OF RED MUD SOLID WASTE FROM THE BAYER ALUMINA PROCESS | 103 |
| Introduction | 103 |
| Properties and Preparation of the Red Mud Sorbent | 104 |
| Experimental | 105 |
| Discussion of Results | 106 |
| References | 117 |
| DIMENSIONLESS PLOTS FOR MICROGRAIN MODELS OF REACTING POROUS SOLIDS WITH APPROXIMATIONS TO A SIMPLE LOGARITHMIC CONVERSION OF THE SOLIDS | 118 |
| Introduction | 118 |
| Kinetic Equations and Micrograin Size Distributions | 121 |
| The Gates-Gaudin-Schuhmann Distribution | 122 |
| Log-Normal Distributions | 125 |
| Normal Distributions | 130 |

CONTENTS (continued)


| | Page |
|---|---|
| Computed Fractional Conversions for Porous Solids. . . . . | 134 |
| Uniform Micrograins and the Gates-Gaudin-Schuhmann Micrograin Size Distribution . . . . . | 135 |
| Log-Normal Micrograin Size Distribution . . . . . | 140 |
| Normal Micrograin Size Distributions. . . . . | 143 |
| Nomenclature . . . . . | 148 |
| References . . . . . | 151 |
| APPENDIX. MASS AND HEAT TRANSFER DURING SULFATION. . . . . | 152 |
| Estimation of Effective Diffusion Coefficient. . . . . | 152 |
| Estimation of Effectiveness Factor for Pore Diffusion. . . . | 153 |
| Estimation of Temperature Effect on Effectiveness Factor . . | 154 |
| Nomenclature . . . . . | 156 |
| References . . . . . | 157 |

LIST OF FIGURES


| Figure | | Page |
|---|---|---|
| 1-1 | Gibbs Free Energy of Formation of Selected Sulfites. . . | 5 |
| 1-2 | Gibbs Free Energy of Formation of Selected Sulfates. . . | 6 |
| 1-3 | Schematic Diagram of Closed Loop Thermogravimetric Apparatus With Recording Electrobalance. . . . . | 9 |
| 1-4 | Schematic Diagram of Flow-Through Thermogravimetric Apparatus With McBain Balance. . . . . | 10 |
| 2-1 | Extent of Sulfite and Sulfate Formation at 300°C In 0.003 atm $SO_2$ (dry). . . . . | 17 |
| 2-2 | Absorption of $SO_2$ by Alkalized Alumina At Various Temperatures; With 0.003 atm $SO_2$ (dry); Also With 0.003 atm $SO_2$ and 0.024 atm Water Vapor. . . . . | 18 |
| 2-3 | Nucleation of $Na_3Al(SO_4)_3$ at 600°C in 0.003 atm $SO_2$(dry) | 20 |
| 2-4 | Absorption of $SO_2$ by Alkalized Alumina at 300°C; With 0.024 atm Water Vapor and Various Concentrations of $SO_2$. . . . . | 21 |
| 2-5 | Absorption of $SO_2$ by Alkalized Alumina at 400°C; With 0.024 atm Water Vapor and Various Concentrations of $SO_2$. . . . . | 22 |
| 2-6 | Absorption of $SO_2$ by Alkalized Alumina at 500°C; With 0.024 atm Water Vapor and Various Concentrations of $SO_2$. . . . . | 23 |
| 2-7 | Scanning Electron Micrographs of the Pellet Surfaces After Reaction at 300°C With (a) 0.003 atm $SO_2$ and 0.024 atm Water Vapor and (b) 0.003 atm $SO_2$ (dry). . . | 24 |
| 2-8 | Effect of Pellet Size on the Absorption of $SO_2$ by Alkalized Alumina in 0.003 atm $SO_2$ (dry) at 300°C and 500°C. . . . . | 27 |

LIST OF FIGURES (continued)


| Figure | | Page |
|---|---|---|
| 2-9 | Plot of $\log(1-F_{Na})$ vs. Time; with Various Concentrations of $SO_2$ at 300°C. | 28 |
| 2-10 | Plot of $\log(1-F_{Na})$ vs. Time; with Various Concentrations of $SO_2$ at 400°C. | 29 |
| 2-11 | Plot of $\log(1-F_{Na})$ vs. Time; with Various Concentrations of $SO_2$ at 500°C. | 30 |
| 2-12 | First Order Dependency of the Rate on $p_{SO_2}$ | 32 |
| 2-13 | Arrhenius Plot of the Experimental Rate Constant for the Formation of $Na_2SO_4$ from Alkalized Alumina | 33 |
| 2-14 | Plot of $\log(1-F_{Al})$ vs. Time; at 500°C with Various Concentrations of $SO_2$ | 35 |
| 3-1 | Absorption of $SO_2$ by Alunite (Reduced or Calcined at 800°C for 60 min); with 0.003 atm $SO_2$ and 0.024 atm Water Vapor at 500°C | 45 |
| 3-2 | Absorption of $SO_2$ by Alunite (Reduced at Various Temperatures for 120 min); with 0.003 atm $SO_2$ and 0.024 atm Water Vapor at 500°C | 46 |
| 3-3 | Absorption of $SO_2$ by Alunite (Reduced at 800°C for Various Periods); with 0.003 atm $SO_2$ and 0.024 atm Water Vapor at 500°C | 47 |
| 3-4 | Absorption of $SO_2$ by Reduced Alunite at Various Temperatures; with 0.003 atm $SO_2$ and 0.024 atm Water Vapor. | 49 |
| 3-5a | Absorption of $SO_2$ by Reduced Alunite at 200°C; with 0.024 atm Water Vapor and Various Concentrations of $SO_2$. | 51 |
| 3-5b | Absorption of $SO_2$ by Reduced Alunite at 500°C; with 0.024 atm Water Vapor and Various Concentrations of $SO_2$. | 52 |

LIST OF FIGURES (continued)


| Figure | | Page |
|---|---|---|
| 3-6 | Effect of Oxygen Partial Pressure on the Absorption of $SO_2$; with 0.003 atm $SO_2$ (dry) at 500°C . . . . . | 54 |
| 3-7 | Effect of Water Vapor on the Absorption of $SO_2$; with 0.003 atm $SO_2$ and Various Partial Pressures of Water Vapor at 200°C and 500°C . . . . . | 55 |
| 3-8 | Plot of $\log_e(1-F_{K_2O})$ vs. Time; with 0.003 atm $SO_2$ and 0.024 atm Water Vapor at Various Temperatures. . . . . | 58 |
| 3-9 | Plot of $\log_e(1-F_{K_2O})$ vs. Time; with Various Concentrations of $SO_2$ and 0.024 atm Water Vapor at 200°C. . . . | 59 |
| 3-10 | Plot of Experimental Rate Constant for the Sulfation of $K_2O$ vs. $p_{SO_2}$ . . . . . | 60 |
| 3-11 | Plot of $\log_e(k_{K_2O}A_o)$ vs. 1/T . . . . . | 62 |
| 3-12 | Contribution by Sulfation of Alumina Towards the Observed Weight Gain; with 0.003 atm $SO_2$ and 0.024 atm Water Vapor at 500°C . . . . . | 65 |
| 3-13 | Plot of $\log_e(1-F_{Al_2O_3})$ vs. Time; with 0.003 atm $SO_2$ and 0.024 atm Water Vapor at 300°C, 400°C, and 500°C . | 66 |
| 3-14 | Plot of $\log_e(1-F_{Al_2O_3})$ vs. Time; with Various Concentrations of $SO_2$ and 0.024 atm Water Vapor at 500°C . . | 67 |
| 3-15 | First Order Dependency of the Rate of Sulfation of Alumina on $p_{SO_2}$. . . . . | 68 |
| 3-16 | Plot of $\log_e(k_{Al_2O_3}A_o)$ vs. 1/T. . . . . | 69 |
| 3-17 | Calculation of $k'_{Al_2O_3}$ by the Second Method at 500°C . . | 71 |
| 4-1 | Sulfur Absorption Curve of Manganese Nodules at 500°C. . | 81 |
| 4-2 | Sulfur Absorption Curve of Manganese Nodules at 300°C. . | 84 |
| 4-3 | Plot of log(I-F) vs. Time at 400°C for Different $SO_2$ Partial Pressures. . . . . | 87 |
| 4-4 | Plot of log(I-F) vs. Time at 500°C for Different $SO_2$ Partial Pressures. . . . . | 88 |

LIST OF FIGURES (continued)


| Figure | | Page |
|---|---|---|
| 4-5 | Plot of log(1-F) vs. Time at 600°C for Different $SO_2$ Partial Pressures. . . . . | 89 |
| 4-6 | Determination of the Experimental Rate Constant at 400, 500 and 600°C . . . . . | 90 |
| 4-7 | Arrhenius Plot of the Experimental Rate Constant and Initial Rate Constant. . . . . | 91 |
| 4-8 | Initial Rate As Function of Sulfur Dioxide Partial Pressure at 300, 400, 500 and 600°C. . . . . | 92 |
| 4-9 | Fractional Reaction vs. Time at 500°C for Different Particle Sizes . . . . . | 94 |
| 4-10 | Scanning Electron Micrographs of Specimens Completely Sulfated in Dry and Wet Gas Mixtures . . . . . | 96 |
| 4-11 | Oxygen Effect on the Reaction Rate at 400°C. . . . . | 98 |
| 5-1 | Recycle Reactor. . . . . | 107 |
| 5-2 | Sulfur Absorption Curve of Dry Red Mud at 300°C. . . . . | 109 |
| 5-3 | Sulfur Absorption Curve of Dry Red Mud at 400°C . . . . | 110 |
| 5-4 | Sulfur Absorption Curve of Dry Red Mud at 500°C. . . . . | 111 |
| 5-5 | Sorption Capacity After 24 Hours for 300, 400 and 500°C. | 113 |
| 5-6 | Calcium and Sulfur Fluorescent X-ray Images from a Partially Reacted Specimen. . . . . | 115 |
| 6-1 | Log-Normal Probability Plots of Arbitrary and Experimental Micrograin Size Distributions . . . . . | 127 |
| 6-2 | Volume Distributions of Solids for Arbitrary Log-Normal Volume Distributions of Micrograin Radii. . . . | 128 |
| 6-3 | Normal Probability Plots of Micrograin Size Distributions. . . . . | 132 |
| 6-4 | Volume Distributions of Solids for Arbitrary Normal Number Distributions of Micrograin Radii . . . . . | 133 |

LIST OF FIGURES (continued)


| Figure | | Page |
|---|---|---|
| 6-5 | Aggregate Reaction Curves for Uniform Micrograin Size and the Gates-Gaudin-Schuhmann Distribution. . . . . | 136 |
| 6-6 | Aggregate Reaction Curves for Uniform Micrograin Size and the Gates-Gaudin-Schuhmann Distribution. . . . . | 137 |
| 6-7 | Aggregate Reaction Curves for Uniform Micrograin Size and the Gates-Gaudin-Schuhmann Distribution. . . . . | 138 |
| 6-8 | Logarithmic Plot of Aggregate Reaction Curves for Uniform and GGS Distribution . . . . . | 139 |
| 6-9 | Aggregate Conversion by Surface Chemical Reaction for Log-Normal Distributions of Micrograin Sizes . . . . . | 142 |
| 6-10 | Logarithmic Plot of Conversion by Surface Chemical Reaction for Log-Normal Distributions of Micrograin Sizes. . . . . | 143 |
| 6-11 | Aggregate Conversion by Surface Chemical Reaction for Normal Distributions of Micrograin Sizes . . . . . | 146 |
| 6-12 | Logarithmic Plot of Conversion by Surface Chemical Reaction for Normal Distributions of Micrograin Sizes. . | 147 |

LIST OF TABLES


| Table | | Page |
|---|---|---|
| 2-1 | Chemical Analysis of Grace-USBM Alkalized Alumina. . . . | 14 |
| 3-1 | Properties of Alunite Reduced in Hydrogen. . . . . | 48 |
| 4-1 | Weight Percentage of the Major Components in Blake Plateau Nodules as Equivalent Oxides and as Metals. . . . | 77 |
| 4-2 | Weight Percentage of the Major Components in Pacific Nodules as Equivalent Oxides and Metals. . . . . | 83 |
| 4-3 | Summary of Experiments in the Presence of Water Vapor Using -14+20 Mesh Nodules. . . . . | 95 |
| 5-1 | Chemical Composition of the Dry Red Mud Used in this Study. | 104 |
| 6-1 | Fractional Conversion Equations for Porous Solids with Various Micrograin Size Distributions. . . . . | 123 |
| 6-2 | Summary of Log-Normal Size Distributions Shown in Figures 1 and 2. . . . . | 129 |
| 6-3 | Summary of Normal Distributions of Micrograin Radii; See Figures 3 and 4. . . . . | 131 |

## SUMMARY

The sulfation kinetics of four porous solids with potential as dry sorbents for $SO_2$ in stack gases were investigated using a thermogravimetric method. Supplementary information was obtained by electron beam microprobe analysis, scanning electron microscopy, chemical analyses, surface area measurements and X-ray diffraction. Sulfur dioxide concentrations typical of flue gases and somewhat higher, 0.001 to 0.03 atm, were used. The effect of temperature, sulfur dioxide pressure, oxygen pressure, water vapor and particle size were studied. Particle size had negligible effect within the particle size range studied (< 10 mesh). Therefore, pore diffusion was not a rate controlling mechanism in any of these studies.

Because alkalized alumina had been previously studied, it was investigated as a base-line material and additional kinetic data were obtained. The primary reaction product is sodium sulfate (I), but at higher temperatures and after a nucleation delay, further sulfation results in the formation of sodium aluminum sulfate ($Na_3Al(SO_4)_3$). The present kinetic study is limited to the formation of sodium sulfate. The rate of formation of sodium sulfate is proportional to the sulfur dioxide concentration and is independent of the oxygen partial pressure in the range studied.

The sulfation rate is also proportional to the unreacted fraction of $Na_2O$ in the sorbent, and hence, the rate decreases exponentially approaching complete sulfation asymptotically. The experimental

activation energy for the formation of $Na_2SO_4$ is 2000 cal.mole$^{-1}$. The rate of sulfation is controlled by a surface chemical reaction. The proposed slow rate controlling step is the formation of sodium sulfite which subsequently oxidizes to sodium sulfate rather quickly. This explains the zero order rate dependence on oxygen, and also the appearance of a small amount of sulfite in the initial stages of the reaction without further accumulation. In the absence of water vapor (below 1%), a marked decrease in the rate occurs after about 20% of the reaction. This decrease appears to be caused by the blocking of micropores by the reaction product as indicated by the marked reduction in surface area.

Alunite is a naturally occurring hydrated potassium aluminum sulfate. After reduction in a step identical with the sorbent regeneration the residual material is porous and reactive with $SO_2$.

Preliminary experiments on the reduction of alunite with hydrogen showed that the optimum reduction is obtained at 800°C after 60 minutes. Sulfur is removed as $H_2S$ and can be recovered using the Claus Process. The sulfur dioxide absorption experiments showed that the alunite thus reduced has a high absorption capacity and high absorption rates. The initial rate of absorption at 300°C with 0.003 atm $SO_2$ is $5.6 \times 10^{-4}$ g of S per gram of sorbent and the initial rate increases only slightly with temperature. The maximum absorption capacity is 0.05 g of S per gram of sorbent below 300°C, and this is increased to 0.19 g of S per gram of sorbent above 300°C. These values are comparable to those of alkalized alumina.

The sulfation kinetics of reduced alunite were investigated at temperatures from 100 to 600°C. Below 300°C, the primary reaction product is potassium sulfate, $K_2SO_4$. The formation of $K_2SO_4$ is proportional to

the sulfur dioxide concentration and is independent of oxygen partial pressure. The sulfation rate is also proportional to the unreacted fraction of $K_2O$ in the sorbent. A chemical reaction sequence, similar to that proposed for alkalized alumina, with formation of potassium sulfite as the rate controlling step is proposed.

Above 300°C, sulfation of both $K_2O$ and $Al_2O_3$ occurs. Early in the reaction period $K_2SO_4$ is produced, but later a new phase, $K_3Al(SO_4)_3$, appears. As the sulfation nears completion, a third phase, $KAl(SO_4)_2$ appears, and this phase is identical with dehydrated alunite.

The rate of sulfation of $K_2O$ is faster than that of $Al_2O_3$, which enabled a separation of the $K_2O$ and $Al_2O_3$ sulfation kinetics. The rate of sulfation of alumina is also proportional to the unreacted fraction of alumina that can be sulfated. This rate is proportional to the sulfur dioxide concentration and to the square root of oxygen partial pressure.

The absence of small amounts of water vapor (below 1%) causes a marked decrease in the rate of sulfation in the later stages at low temperatures. An experimental activation energy of only 800 $cal.mole^{-1}$ was found for the sulfation of potassium oxide. The experimental activation energy for the sulfation of alumina is 9600 $cal.mole^{-1}$.

The reaction kinetics of manganese nodules from the Blake Plateau off the Coast of South Carolina were investigated. The sorption capacity of the nodules between 400°C and 600°C was 0.52 to 0.56 g of nodule. This is in stoichiometric agreement with the main metallic components, manganese, iron and calcium, indicating their complete sulfation. This fact was substantiated by wet chemical analyses and powder X-ray diffraction.

For sulfation experiments at 300°C no final uptake was obtained.

At this temperature, manganese sulfates fast, but the other oxides, hematite and calcite, were reacting much slower. Water vapor accelerates the rates.

The rate of reaction between 400 and 600°C was proportional to both the partial pressure of $SO_2$ and the unreacted solid fraction. Temperature only slightly affected the rates. The activation energy was 1.6 kcal $mole^{-1}$. The oxygen dependency was zero order up to about 40% solid conversion, at 400°C. At this point, the rate decreased slightly with decreasing oxygen concentration. Water vapor had little effect at the higher temperatures.

Leaching completely sulfated manganese nodules during 2 1/2 hours in boiling water gave extractions of 82% nickel, 99% copper, and 97% cobalt. Hydrolysis made the solution slightly acidic. Much of the manganese but little of the iron was extracted. This shows that the reaction of manganese nodules with $SO_2$ from power plant gases can be effectively used both for removing $SO_2$ from stack gases and for subsequent extraction of the contained nickel, cobalt and copper. This may eventually be economic for coastal power plants.

The sorption kinetics of $SO_2$ by dry red mud, the waste product from the Bayer alumina process, were investigated. At 300°C, the sulfation rate is rapid but the sorption capacity is low. At 400°C and 500°C, sorption capacity increases with the $SO_2$ pressure in a complex manner.

In these studies the solid reaction rate was frequently observed to be proportional to the remaining unreacted solid. A result of this is a logarithmic decrease of the remaining unreacted fraction of solids with time. This is superficially analogous with a first order homogeneous reaction with a limited initial amount of reactant. However,

in this case the reaction is heterogeneous and more complex. Various micrograin size distribution models for porous solids were constructed and fractional conversions of the solids (aggregates of micrograins) by a surface chemical reaction rate mechanism were computed and compared with the empirical logarithmic plots of fractional conversion. Good agreement with the experimental logarithmic plots was obtained for expected natural distributions of micrograin sizes.

# INTRODUCTION

## BACKGROUND

Approximately 30,000,000 tons of sulfur dioxide are emitted annually in the United States. The sources are varied but non-ferrous smelters, sulfuric acid plants, petroleum refineries and coke-making plants are significant sources. Over half of the emissions result from the combustion of fossil fuels, primarily coal, in power generating stations. Over 95% of the sulfur effluent in stack gas is in the form of $SO_2$. The concentration in stack gas depends primarily on the sulfur concentration of the fuel and secondarily on combustion practice. Most stack gases contain between 0.05% and 0.3% $SO_2$ by weight.

A large variety of processes for reducing $SO_2$ emissions have been considered. These may be grouped into processes to remove sulfur from the fuels and processes to remove sulfur dioxide from the stack gases prior to discharge. The stack gas removal processes can be further categorized into wet scrubbing processes, including slurry processes, and dry processes, which involve either adsorption or absorption reactions between the combustion gases and a solid sorbent without appreciable loss of the stack gas buoyancy. This is an advantage in dispersing the final effluent from the stack. Some processes involve periodic regeneration of the sorbent coupled with release of the sulfur, usually as $SO_2$, $SO_3$, $H_2S$ or COS, in an enriched stream that can be more economically processed to recover sulfur or a sulfur compound. Other processes are directed toward discard of the sulfur laden sorbent by using inexpensive sorbent materials. This is the primary advantage of limestone and dolomite.

Among the dry sorption processes are chemical reactions between $SO_2$ and several metal oxides to form sulfites

$$MO + SO_2 \rightarrow MSO_3$$

or sulfates

$$MO + SO_2 + \frac{1}{2} O_2 \rightarrow MSO_4.$$

These absorption reactions are generally irreversible at stack gas discharge temperature, but in a few cases the loaded absorbent can be regenerated by heating to a higher temperature where the reverse of the previous equation occurs. However, most metal oxide sorbents require reduction if regeneration is to occur at reasonable temperatures, where sintering and an extreme loss of specific surface and chemical reactivity will not occur. Reduction by hydrogen or carbon monoxide obtained from methane or other fuels may be employed,

$$4H_2 + MSO_4 \rightarrow MO + H_2S + 3H_2O$$

$$4CO + MSO_4 \rightarrow MO + COS + 3CO_2$$

Application of a particular absorbent may be limited by low absorption capacity, slow reaction kinetics or inadequate resistance to attrition or breakage during handling. Attrition is important for the processes requiring regeneration but less so when it is planned to discard the absorbent after the first loading.

The purpose of the present study was to determine the detailed $SO_2$ reaction kinetics and sorption capacity of four materials that are promising absorbents. The criteria for selection of the materials were: availability in large quantities, known or expected high absorption

capacities, low cost or potential low cost and high specific surfaces, which is usually a necessary but not sufficient condition to obtain adequately fast reaction kinetics. These criteria mandated consideration of certain minerals and mineral by-products and waste products.

The absorbents studied were: (1) alkalized alumina ($Na_2O \cdot Al_2O_3$), a material developed as a sulfur dioxide absorbent by the U.S. Bureau of Mines; (2) reduced alunite ($K_2O \cdot 3Al_2O_3$), the product made by reducing the natural mineral alunite in a process identical with regeneration of the sulfate-laden absorbent; (3) sea bed manganese nodules obtained from the Blake Plateau in the Atlantic Ocean off South Carolina; and (4) dried Red Mud, the waste product from the Bayer Process extraction of alumina from bauxite. Previously published experimental kinetic studies on alkalized alumina served as a base line for the present experiments. The kinetics of sulfation of this material have been extended both experimentally and analytically.

Alkalized alumina and reduced alunite would require a sorption/regeneration process system. Manganese nodules and red mud can be regenerated and reused but they also may be economic throw-away sorbents. Approximately 6,000,000 tons of red mud are generated annually in the United States and Jamaica and this constitutes a major solid waste disposal problem. Many billions of tons of manganese nodules exist, but at the present time ocean mining technology is poorly developed. Published alunite reserves in the Western United States exceed 14 million tons and a very large new deposit was recently discovered near Cedar City, Utah.

The format of this report is to consider each of the four absorbent materials and a general discussion of micrograin models for reacting porous solids in separate chapters.

## THERMODYNAMIC CONSIDERATIONS

Standard free energies of the formation of sulfites from several metal oxides contained in the absorbent materials investigated are plotted as a function of temperature in Figure 1. The results were computed using the standard enthalphy, entropy and heat capacity data for the compounds, taken from the Tracor report.[1] Mixed compounds of two or more oxides or two or more sulfites are not considered. The free energy of mixing is expected to be small and should not significantly change the conclusions drawn from considering the compounds separately. Under standard conditions, a partial pressure of sulfur dioxide at one atmosphere, most of the sulfites are unstable above 300°C (573°K). The sulfites of the major metal oxide constituents not shown have positive free energies. The sulfites of sodium and potassium are strong exceptions. If the partial pressure of $SO_2$ is 0.001 atm (0.01%), which is not unreasonable for the concentration in a relatively clean stack gas, then the tendency for dissociation of the sulfite is greater and the negative free energy ($-\Delta G^o$) must be greater than the indicated stability limit. Both sodium sulfite and potassium sulfite meet this criterion and are stable.

Free energy data for the formation of sulfates from the oxides are shown in Figure 2. Results were computed using data from the Tracor report and in the case of manganese, from Kubaschewski, Evans and Alcock[2]. The sulfates are more stable than the corresponding sulfites. However, the sulfates of nickel, copper, manganese, iron and aluminum will show some reversibility (thermal dissociation) on heating above 500 or 600°C. The sulfates of sodium, potassium and calcium are too stable to be regenerated by thermal dissociation and reduction would be required.

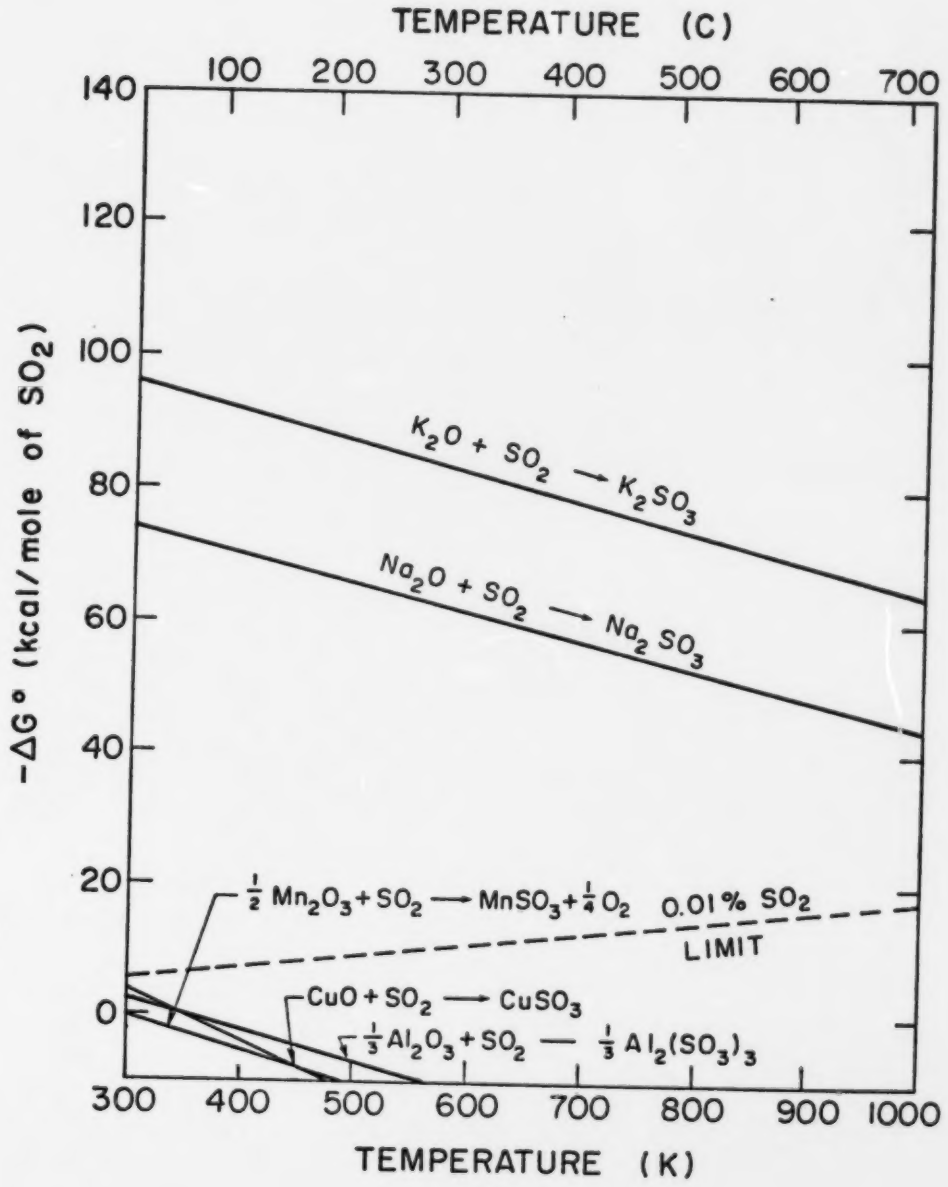


Figure 1. Gibbs free energy of formation of selected sulfites.

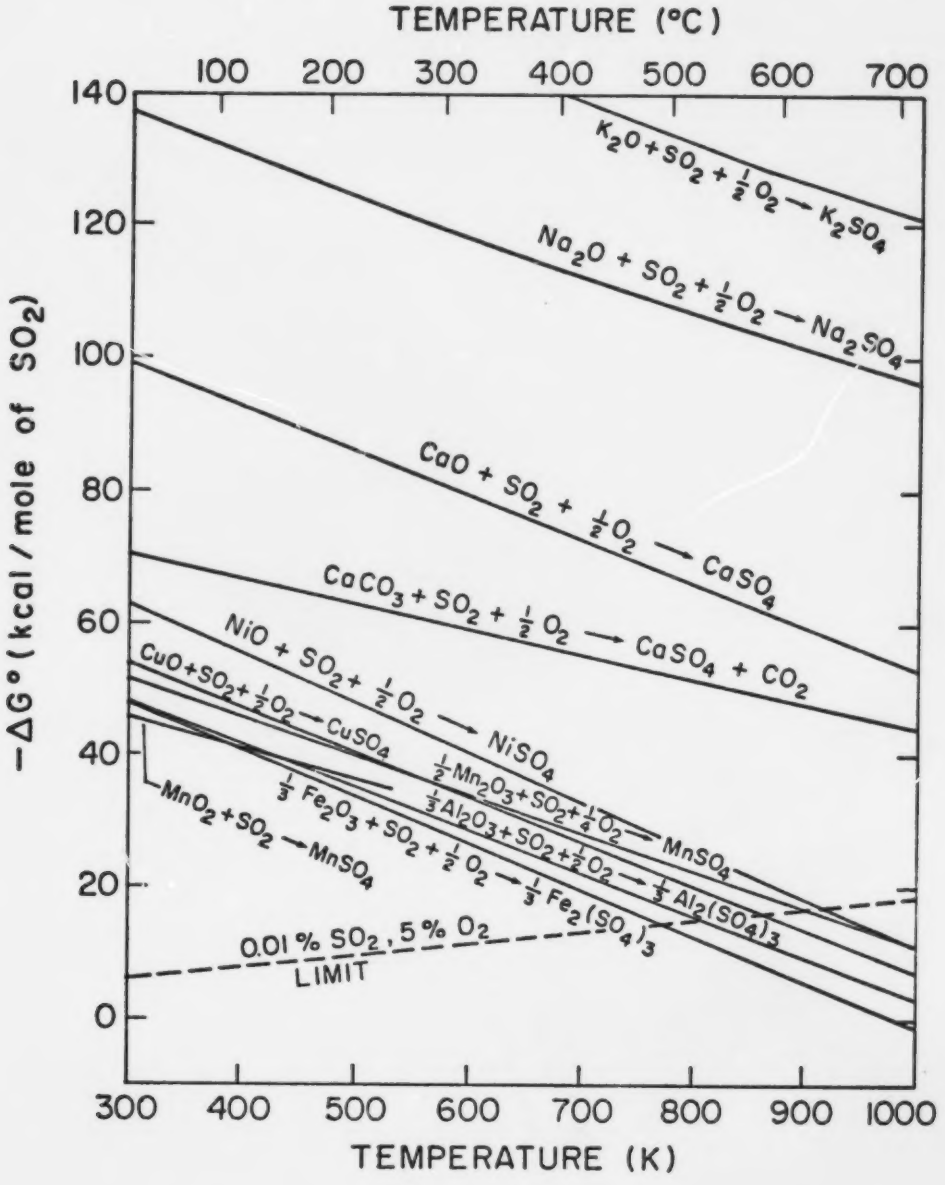


Figure 2. Gibbs free energy of formation of selected sulfates.

## EXPERIMENTAL METHODS

Sulfur dioxide reacting with the absorbents to produce either sulfates or sulfites will cause an increase in weight. Reaction rates can be determined by monitoring the time rate of weight increase at a fixed gas composition and temperature. Two thermogravimetric systems were used. Each involved weighing the specimen in a crucible suspended from the balance in a vertical tube furnace. Some supplementary kinetic data were obtained for red mud in a fixed bed reactor by measuring the $SO_2$ concentration of the effluent gas with an infrared on-stream analyzer.

The thermogravimetric data were supplemented by a variety of other determinations on specimens following partial reaction. The results were compared with similar results before reaction. Electron beam microprobe analyses were used to determine the distribution of sulfur and other elements within sectioned specimens. A three-channel analyzer was used to enable concurrent determinations of associated elements. Crystalline phases were identified by powder x-ray diffraction methods. Wet chemical analyses were used to determine mean concentrations of the elements and wet chemical methods were used to determine sulfur separately as sulfite ion and as sulfate ion.

Fracture surfaces of specimens were examined and photographed using scanning electron microscopy. Internal surface area was measured by the B.E.T. method. Pore size distributions were determined by the B.J.H. method using an Orr Surface Analyzer.

Thermogravimetric experiments were made in both dry and wet gases. A continuously recording electrobalance (Cahn Model RG) was usually used for dry gas experiments while a quartz helix (McBain) balance was used for wet gas experiments. However, the gas trains were interchangeable

and both balances were used with wet and dry gases.

The gas train for the dry gas experiments was a closed loop consisting of a reaction chamber heated by a proportionally controlled electric resistance tube furnace, a gas reservoir and a circulating pump, see Figure 3. The large reservoir, initially 18 liters and later 41 liters, provided a nearly constant concentration of sulfur dioxide through the reaction period even though the gas concentrations used were very low. To prevent dynamic oscillations in the balance many experiments were conducted at a total pressure of 0.1 atm. After loading a pre-weighed specimen, the entire gas train was evacuated and the reaction chamber was heated to the experiment temperature. After temperature stabilization, the reaction chamber was isolated from the gas loop and a specified aliquot of $SO_2$ corresponding to the desired operating concentration was injected into the loop from a gas burette. After the gas was well mixed the chamber was opened to the gas loop, which intiated the sulfation experiment.

The wet gas train was a flow-through system with all of the gases except water vapor introduced through flow meters. Oxygen was bubbled through a water humidifier held at a constant temperature. A metered nitrogen-sulfur dioxide mixture joined the oxygen/water vapor mixture at the reaction chamber. The gas passed over the specimen, left the reaction chamber at one atmosphere and was optionally monitored for residual $SO_2$ by the infra-red analyzer. This apparatus is shown with the McBain balance in Figure 4.

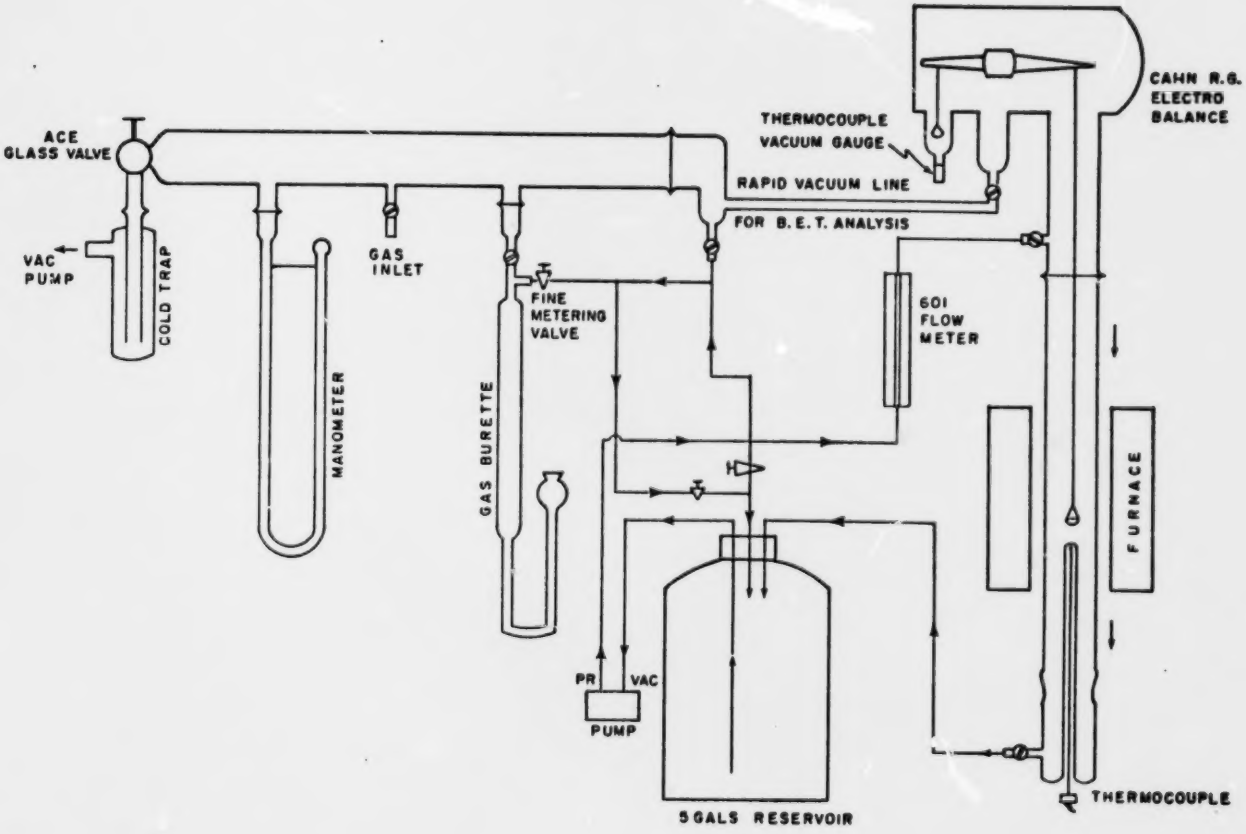


Figure 3. Schematic diagram of closed loop thermogravimetric apparatus with recording electrobalance.

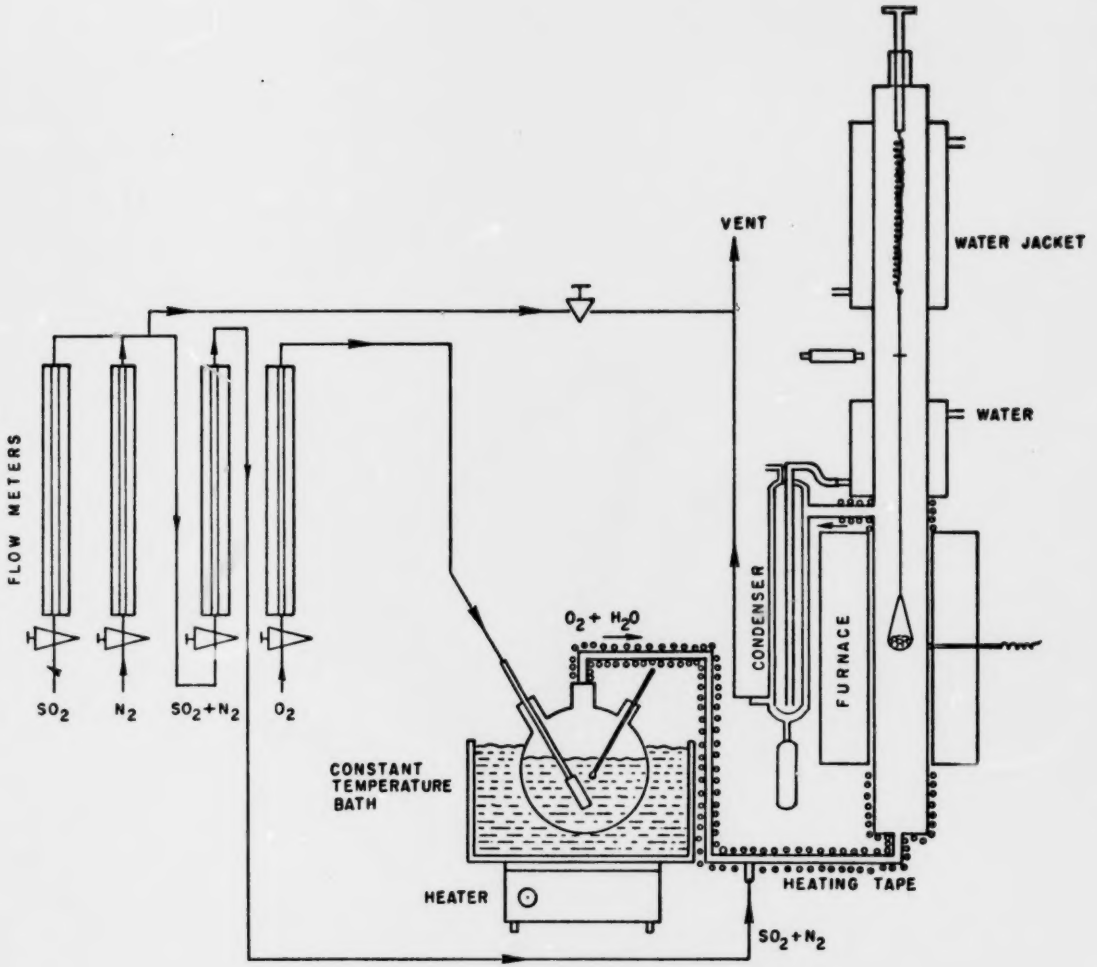


Figure 4. Schematic diagram of flow-through thermogravimetric apparatus with McBain balance.

## REFERENCES

(1) Tracor Co. Applicability of Metal Oxides to the Development of new Processes for Removing $SO_2$ from Flue Gases. Vol. II, Section 8. 31 July, 1969.

(2) Kubaschewski, O., E.Ll. Evans, and C.B. Alcock. Metallurgical Thermochemistry. Pergamon Press. 1967. 495 p.

## KINETICS OF SULFATION OF ALKALIZED ALUMINA ($Na_2O \cdot Al_2O_3$)

### INTRODUCTION

Solid sorption and wet scrubbing processes are being considered for the removal of $SO_2$ from power plant flue gases, which typically contain 0.05 to 0.3%. The solid sorption processes work on hot flue gases and retain their buoyancy for maximum gas dispersion after removal of $SO_2$.

Among the solid processes are chemical reactions with metal oxides to form sulfites ($MO + SO_2 = MSO_3$), or sulfates ($MO + SO_2 + \frac{1}{2} O_2 = MSO_4$). Alkalized alumina, consisting of $NaAlO_2$ and off-stoichiometric variants, is an efficient absorbent of $SO_2$ under the flue gas conditions and the oxide can be periodically regenerated by $H_2$ or natural gas to produce a concentrated stream of $H_2S$, which then may be converted to elemental sulfur.

The Bureau of Mines has investigated the sorption capacity of alkalized alumina and its regeneration. Their studies include the preparation of suitable starting material, sorption of $SO_2$ in static and fluidized beds[1,2] and operation of a pilot plant.[3] They investigated the kinetics of the absorption reactions and concluded that the rate is proportional to the amount unreacted to the power n, with n ranging from 2 to 5. A negligibly small activation energy was observed.[4]

The objective of the present study was to determine the kinetics of sulfation of alkalized alumina over the temperature range from 300 to 600°C, using sulfur dioxide pressures from 0.001 to 0.025 atm. This spans the temperatures and the sulfur dioxide pressures typical of power plant flue gases and the more dilute streams in nonferrous smelters.

Thermodynamic data on sodium aluminate, sodium oxide, aluminum oxide, and the sulfites and sulfates of sodium and aluminum have been reported.[5] The free energy of the sulfiting and sulfating reactions were computed. In the temperature range of interest these reactions are irreversible at the sulfur dioxide and oxygen pressures expected in flue gases or used in these experiments. Sodium sulfate is more stable than aluminum sulfate.

## PREPARATION OF ALKALIZED ALUMINA

The initial process for the preparation of alkalized alumina was originated by Bienstock and Field.[6] Further work by U.S. Bureau of Mines and Grace Chemical Co. independently led to a $NaAlO_2$-$CO_2$ process.[7] In the latter process the commercial sodium aluminate or the alkalized alumina from the Bienstock process is dissolved in water, saturated with $CO_2$ and reprecipitated by disgestion at 90°C. The final step is calcination of the residue at 700°C. All of the alkalized alumina used in this study was prepared by the latter method.

Alkalized alumina prepared in our laboratory and at Grace Chemical Co. in large batches for the U.S. Bureau of Mines were used. Although the results were similar with either material, most of the experiments were conducted with the Grace-USBM material because it exhibited less sample variation in internal surface area than exhibited by the much smaller batches of material prepared in our laboratory.

The Grace-USBM alkalized alumina was extruded and then rolled so that the pellets were 8-10 mesh in size and nearly spherical. This alkalized alumina contained some sulfate and iron resulting from previous use and regeneration. To remove the sulfate and to provide a consistent

starting material, all of the specimen materials were heated at 800°C for 2 hours in a stream of hydrogen to remove the sulfate followed by a stream of oxygen to reoxidize iron. This activation step was performed in small batches as required. The chemical analysis of the activated Grace-USBM alkalized alumina used in the experiments is shown in Table I.

Table 1. CHEMICAL ANALYSIS OF GRACE-USBM ALKALIZED ALUMINA

| Constituent | % |
|---|---|
| Sodium Oxide ($Na_2O$) | 30.45 |
| Sulfate ($SO_4^{--}$) | 0.53 |
| Iron (Fe) | 1.00 |
| Calcium (Ca) | 0.50 |
| Aluminum Oxide ($Al_2O_3$) | Rest |

The B.E.T. surface area of Grace-USBM alkalized alumina varied from 42 to 48 $m^2g^{-1}$. From apparent and true density measurements, the porosity was found to be about 60% by volume. Pore size distribution analysis by the B.E.T. sorption method showed that 60 to 70% of the pores are in the range of 20 to 200 A.

The fractured pellets show a concentric layered morphology. Often this consisted of a core and a distinct shell partially separated by a concentric shrinkage crack. The thickness of the shell varied widely between pellets. Though the pellets have a uniform average sodium and aluminum content, electron beam microprobe transverses showed that there are localized variations of ±20% of the mean values.

## EXPERIMENTAL

Both sulfating and sulfiting kinetics involve a net weight increase, and reaction rates can be determined by monitoring weight gain, at fixed gas conditions and temperature. Pressed and sintered discs and rolled pellets of alkalized alumina were suspended in a quartz basket from a microbalance.

The thermogravimetric data were supplemented by a variety of other determinations on partially reacted specimens. Electron beam microprobe analyses were used to determine the distribution of sodium, sulfur, and aluminum within the reacted specimens while wet chemical analyses were used to determine average concentration of sodium, and the amount of sulfur present as sulfite and sulfate. Fractured surfaces were examined with a scanning electron microscope and surface area measurements were made with the partially and fully reacted specimens. Crystalline phases were determined by X-ray powder diffraction analyses.

A McBain quartz balance was used for the thermogravimetric sorption experiments with the specimen suspended in a vertical tube furnace. Flowmeters were used to regulate the entering gas composition. During wet gas experiments, oxygen was bubbled through water at constant temperature, and the oxygen-water vapor stream joined a sulfur dioxide-nitrogen stream before entering the reaction chamber. The gases left the reactor at a total pressure of one atm and entered an infrared residual sulfur dioxide analyzer.

The kinetics of sulfur dioxide absorption by alkalized alumina were investigated from 300°C to 500°C, using sulfur dioxide partial pressures from 0.001 to 0.025 atm. Both dry gases and gases containing 0.024 atm water vapor were used. The effect of oxygen partial pressures from 0.01

to 1 atm was also studied. Various pellet sizes were employed in order to study the dependance of rate on the particle size.

RESULTS

Sulfation of alkalized alumina is complex and a general summary of the results will precede a more detailed discussion. The primary reaction product is sodium sulfate (I), and thermogravimetric results are usually expressed as the equivalent fraction of sodium oxide, $F_{Na}$, that has been converted to $Na_2SO_4$. Alumina is generally sulfated later in the reaction sequence. Only minor amounts of sulfite were produced, see Figure 1. Similar sulfite concentrations were obtained from 300°C to 600°C with and without water vapor.

All the thermogravimetric experiments have yielded a decrease in sulfation rate with time. The initial rates (rates extrapolated to zero time) increased with sulfur dioxide pressure and temperature, but were independent of the oxygen pressure within the range observed (0.01 to 1 atm).

Although the initial rates were identical in wet and dry gases, as time passed the retardation of the rate became severe unless a small amount of water was present. This effect is illustrated in Figure 2 which shows the weight increase, expressed as $F_{Na}$, versus time of reaction in a gas containing 0.003 atm of sulfur dioxide. For the purposes of this paper, the runs in wet gases are considered to be the standard sulfation kinetic behaviour. Partial sulfation of alumina often causes the calculated values of $F_{Na}$ to exceed 1, as shown in Figure 2.

The primacy of sodium sulfate formation is indicated by weight gain curves, which tend to approach complete sodium fractional uptake, $F_{Na} = 1$

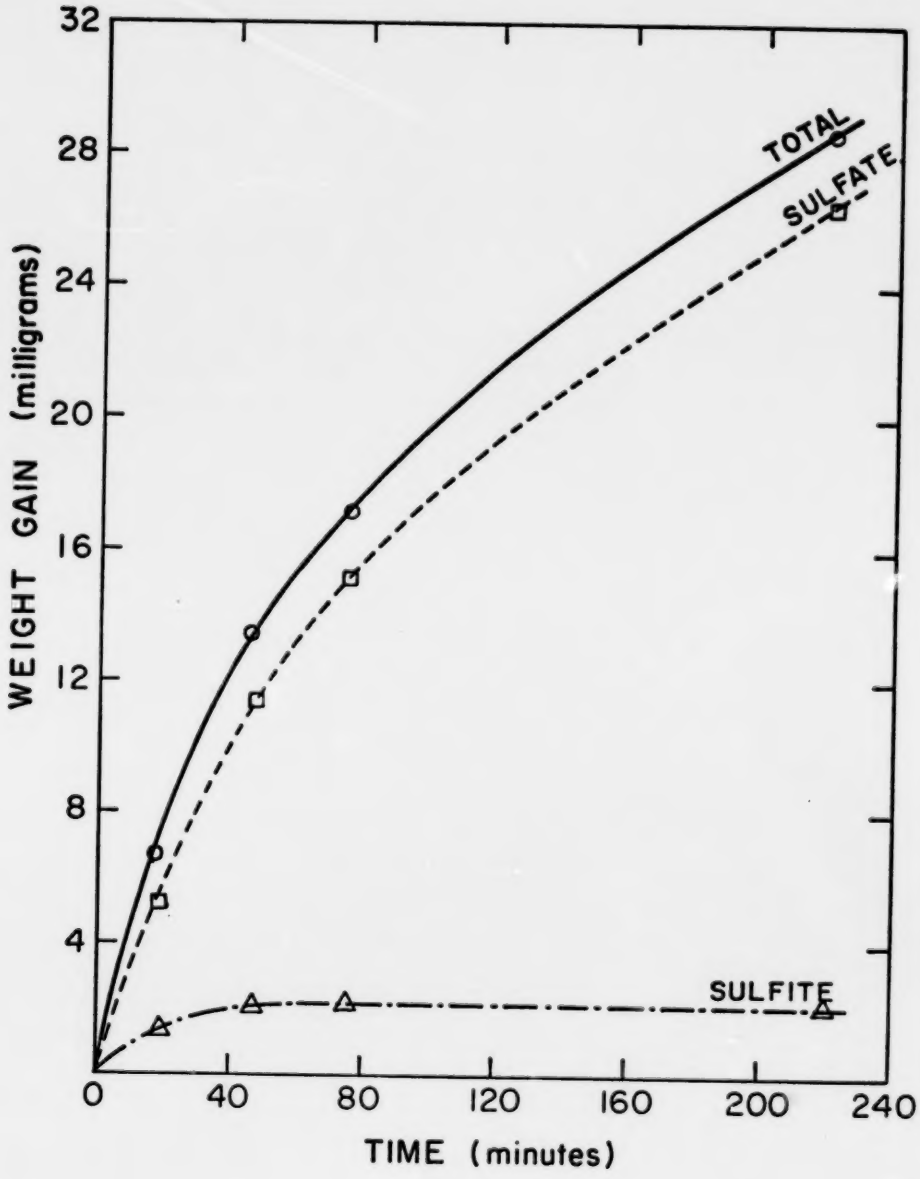


Figure 1. Extent of sulfite and sulfate formation at 300°C in 0.003 atm $SO_2$ (dry).

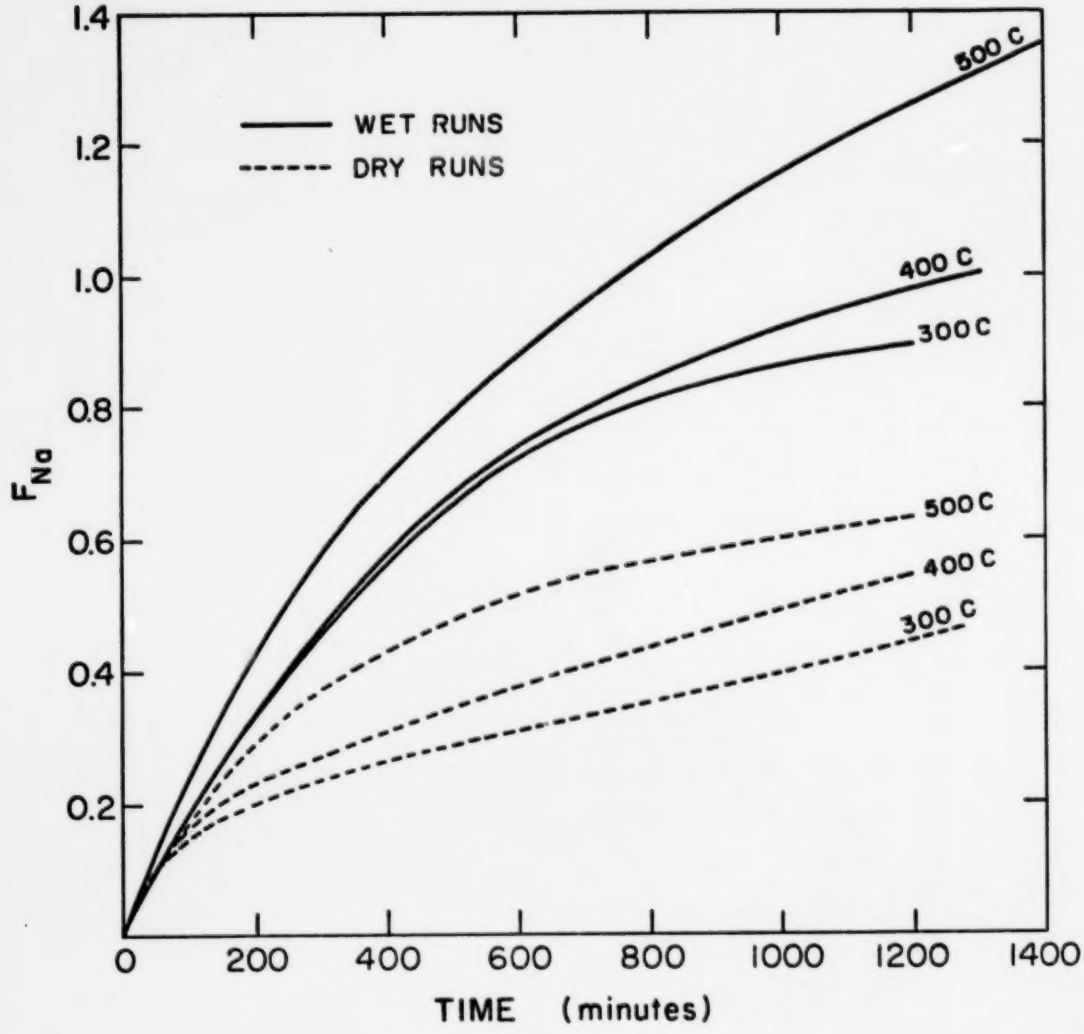


Figure 2. Absorption of $SO_2$ by alkalized alumina at various temperatures; with 0.003 atm $SO_2$ (dry); also with 0.003 atm $SO_2$ and 0.024 atm water vapor.

asymptotically. The intensities of sodium aluminate X-ray diffraction peaks decrease while the sodium sulfate (I) diffraction peaks increase in intensity with increasing sulfation time. At high temperatures and in the late stages of sulfation a mixed sulfate, $Na_3Al(SO_4)_3$, appears in the X-ray diffraction spectrum. The formation of sodium aluminum sulfate undoubtedly involves nucleation and a partial solid state reaction between $SO_2(g)$, $O_2(g)$, $Al_2O_3$ and the $Na_2SO_4$ precursor reaction product. Figure 3 shows the nucleation of $Na_3Al(SO_4)_3$ after 800 minutes at 600°C in a dry atmosphere accompanied by a marked increase in the reaction rate. Nucleation of the mixed sulfate is initiated at high temperatures and by water vapor. Because of the earlier nucleation in wet gas runs there is no inflection in the absorption rate curves. Although there is no X-ray diffraction evidence for aluminum sulfate some must usually be formed before nucleation of the mixed sulfate to account for all of the weight gain. Chao and Sun[8] report that the sulfation of $Al_2O_3$ is normally slow to 600°C but that sodium sulfate enhances the sulfation of alumina at temperatures above 300°C.

Representative thermogravimetric curves showing the effect of $SO_2$ partial pressures on the sulfation rate in wet gases at 300°C, 400°C and 500°C are shown in Figures 4, 5 and 6, respectively. At 300°C and 400°C there is very little if any sulfation of alumina, $F_{Na} \leq 1$, while at 500°C complete sulfation of sodium and aluminum oxides is achieved at 2.5% $SO_2$, $F_{Na} \simeq 2$.

Surface area measurements showed that completely reacted pellets have a specific surface of 15 to 20 $m^2g^{-1}$ after dry runs, and about 30 to 35 $m^2g^{-1}$ after reaction with wet gases. The reduction of the surface area increases as the temperature is lowered. These observations

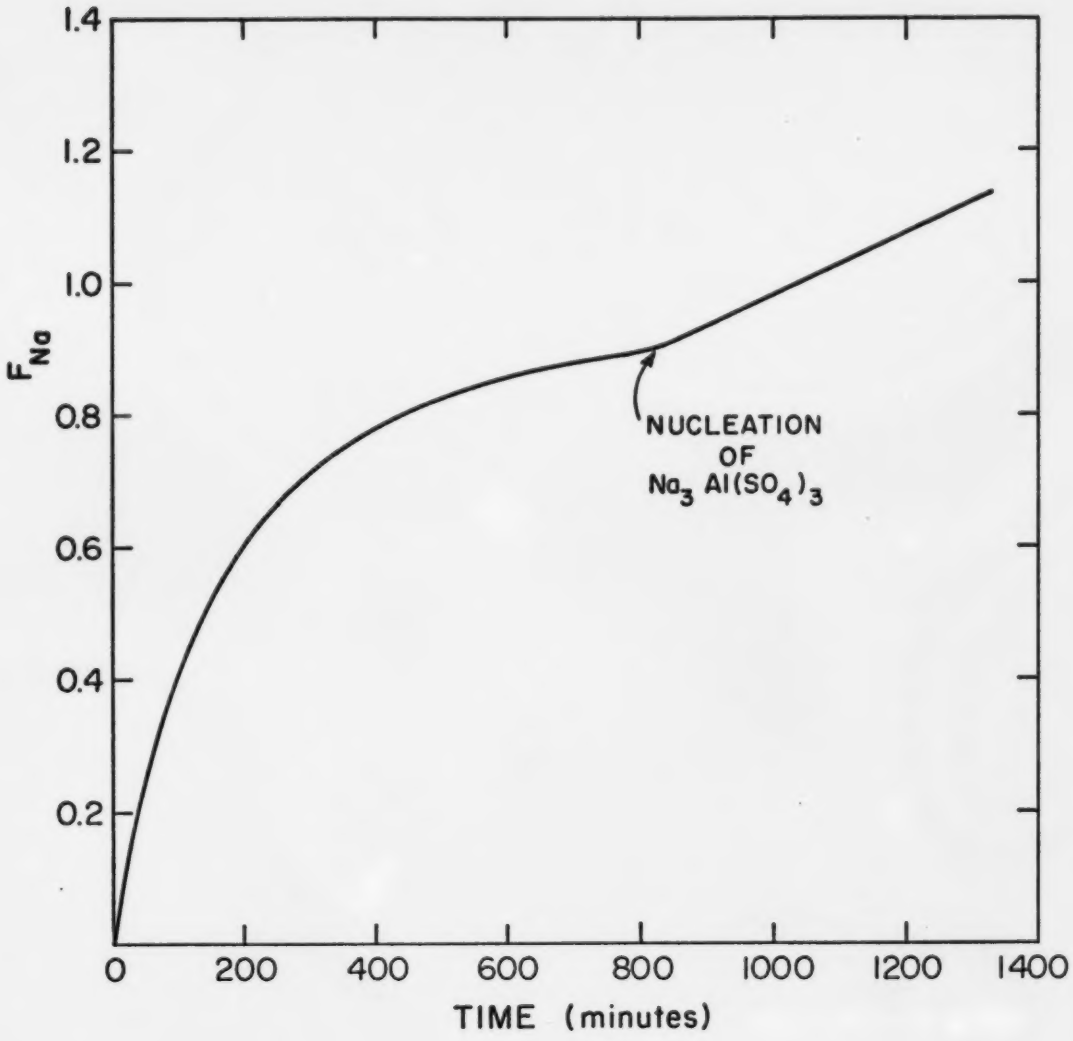


Figure 3. Nucleation of $Na_3Al(SO_4)_3$ at 600°C in 0.003 atm $SO_2$ (dry).

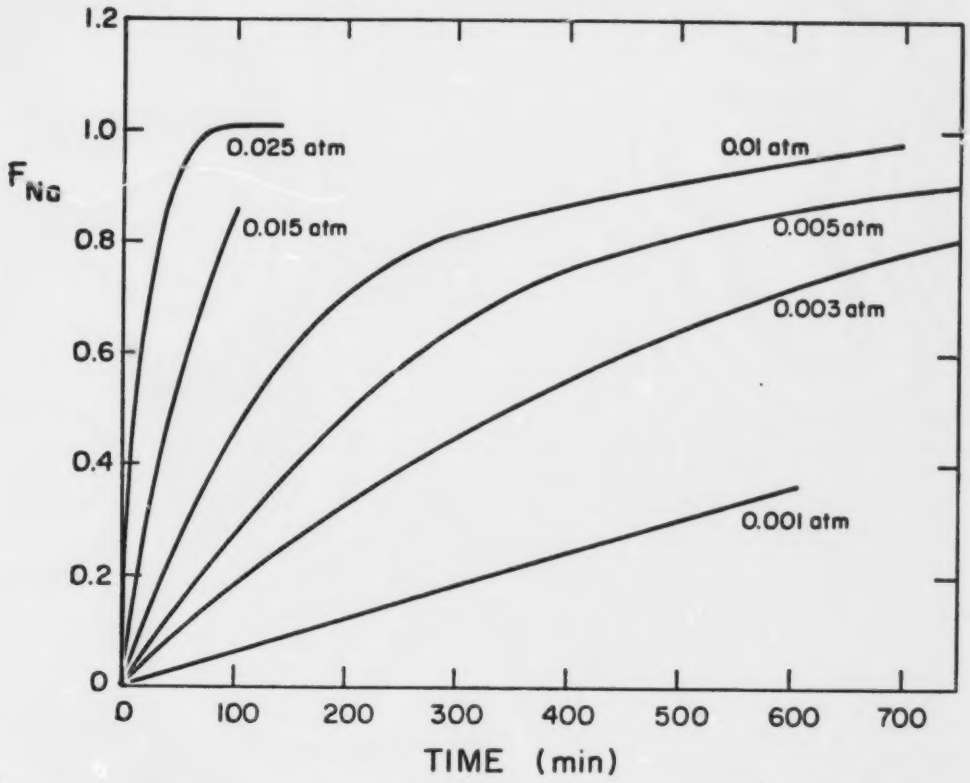


Figure 4. Absorption of $SO_2$ by alkalized alumina at 300°C; with 0.024 atm water vapor and various concentrations of $SO_2$.

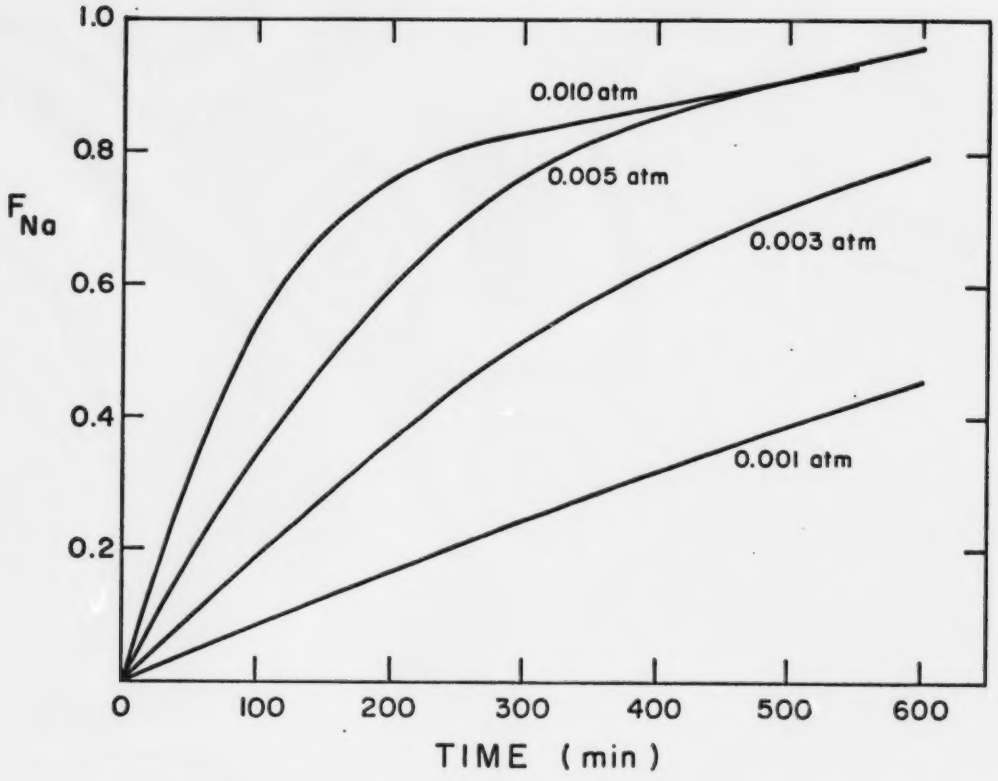


Figure 5. Absorption of $SO_2$ by alkalized alumina at 400°C; with 0.024 atm water vapor and various concentrations of $SO_2$.

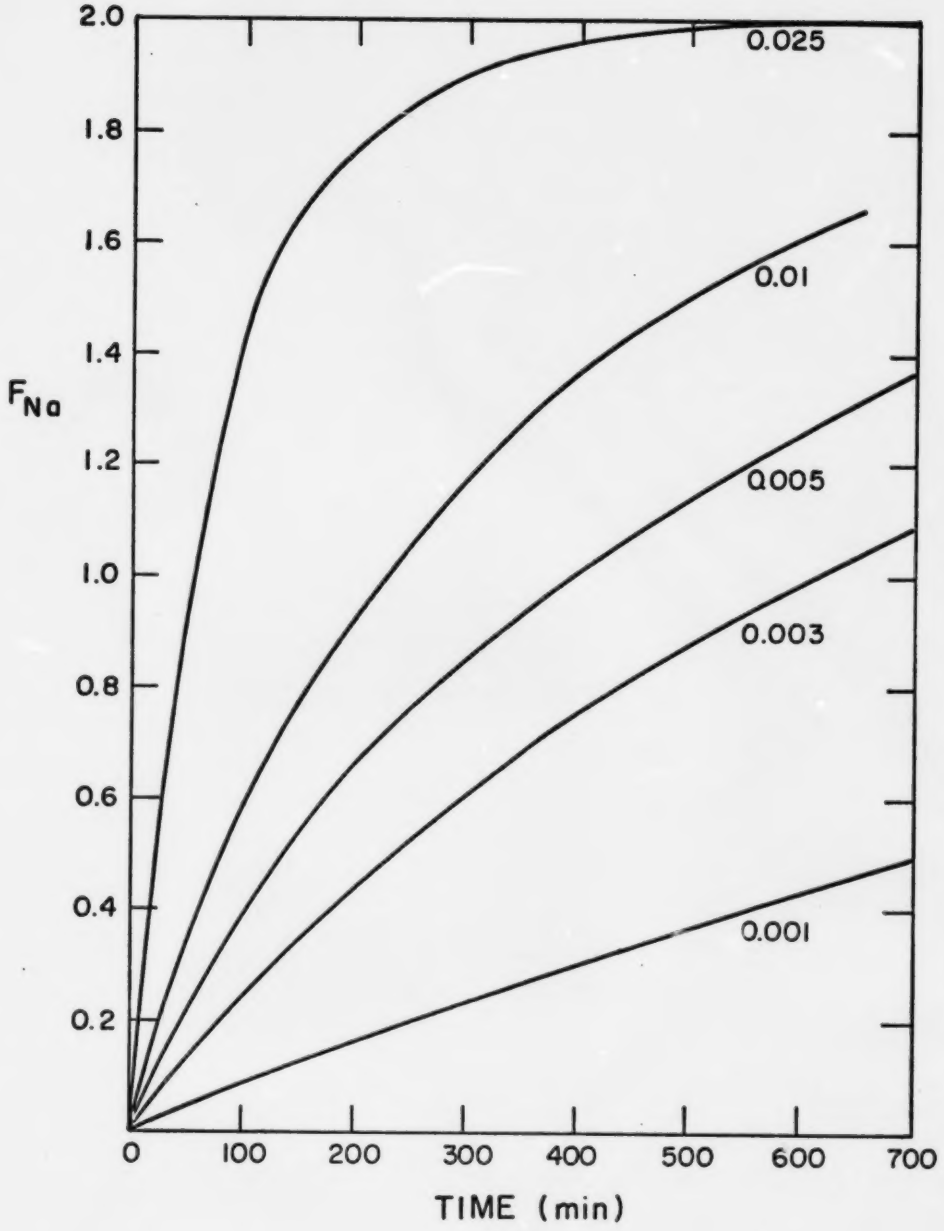


Figure 6. Absorption of $SO_2$ by alkalized alumina at 500°C; with 0.024 atm water vapor and various concentrations of $SO_2$.

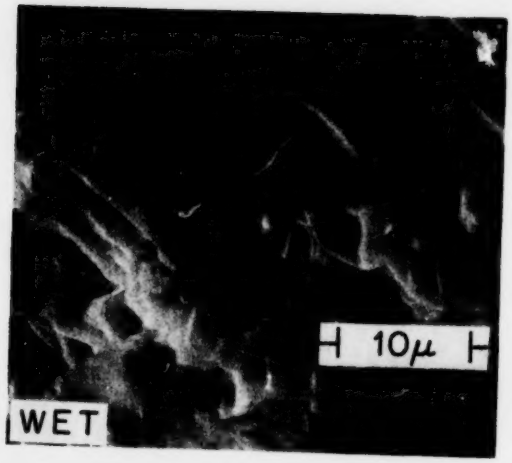


Reproduced from best available copy.

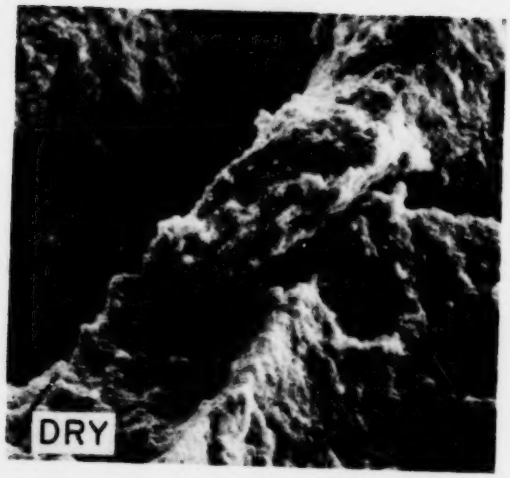


Figure 7. Scanning electron micrographs of the pellet surfaces after reaction at 300°C with (a) 0.003 atm $SO_2$ and 0.024 atm water vapor and (b) 0.003 atm $SO_2$ (dry).

consistent with the rate increase expected from a comparison of the effectiveness factor. A series of thermogravimetric runs for progressively smaller particles at 0.003 atm of $SO_2$ and at 300°C and 500°C is shown in Fig. 8.

Temperature gradients within the pellets caused by the endothermic sulfation reactions were calculated; see the appendix. Temperature reductions from this cause cannot exceed 1°C and will have a negligible effect on the assumed isothermal rate.

The initial rates are first order in $SO_2$, zero order in oxygen, and involve the selective sulfation of sodium oxide. Initially, the rates are the same in both wet and dry gases, and can be expressed as,

$$\left.\frac{dF_{Na}}{dt}\right|_{t=0} = k_{Na}\, p_{SO_2} \qquad (1)$$

where $k_{Na}$ is the extensive rate constant. The rates are also proportional to the unreacted fraction, $1-F_{Na}$:

$$\frac{dF_{Na}}{dt} = k_{Na}(1-F_{Na})\, p_{SO_2} \qquad (2)$$

Integration leads to the following expression for the fractional formation of sodium sulfate,

$$F_{Na} = 1-\exp(-k_{Na} \cdot p_{SO_2} \cdot t) \qquad (3)$$

Equation (3) can be expressed logarithmically and this provides a convenient test of the experimental data in wet gases,

suggest that the blocking of pores, thereby cutting down the available surface area for reaction, is probably the cause of the reduction in the rate with dry gases.

It should be noted that water vapor acts only as a catalyst, and that the rate is not increased by larger water vapor pressures. There is no difference in the X-ray diffraction patterns of sodium sulfate formed after reaction with wet and dry gases. Typical scanning electron micrographs of the pellet surfaces taken after reaction at 300°C, in a gas containing 0.003 atm $SO_2$, and after reaction with a gas containing the same amount of $SO_2$ and 0.024 atm water vapor are shown in Fig. 7. Dry sulfation does not appear to affect the surface morphology of alkalized alumina.

The effectiveness factor determined for a reaction rate at 500°C, 0.015 atm $SO_2$, is about 0.8 for a 200 A pore and an 8-10 mesh particle, see appendix. The pore volume distribution of the starting material computed from B.E.T. sorption isotherms showed that about 40% of the pore volume lies above 200 A. Hence, the transfer of $SO_2$ from the exterior into the interior of the porous pellet by transport in major pore channels can be ruled out as a primary rate determining mechanism. This was confirmed when several reacted pellets were sectioned and examined by electron beam microprobe analysis. Occasionally there was some reduction in the sulfur concentration in traversing a partially reacted pellet from the surface to the center, but not nearly as much as would be required if pore diffusion into the pellet was the rate controlling step.

Thermogravimetric runs made on progressively smaller particles produced a moderate increase in rate. The rate for -100 mesh particles was approximately 20% greater than the 8-10 mesh pellets, which is

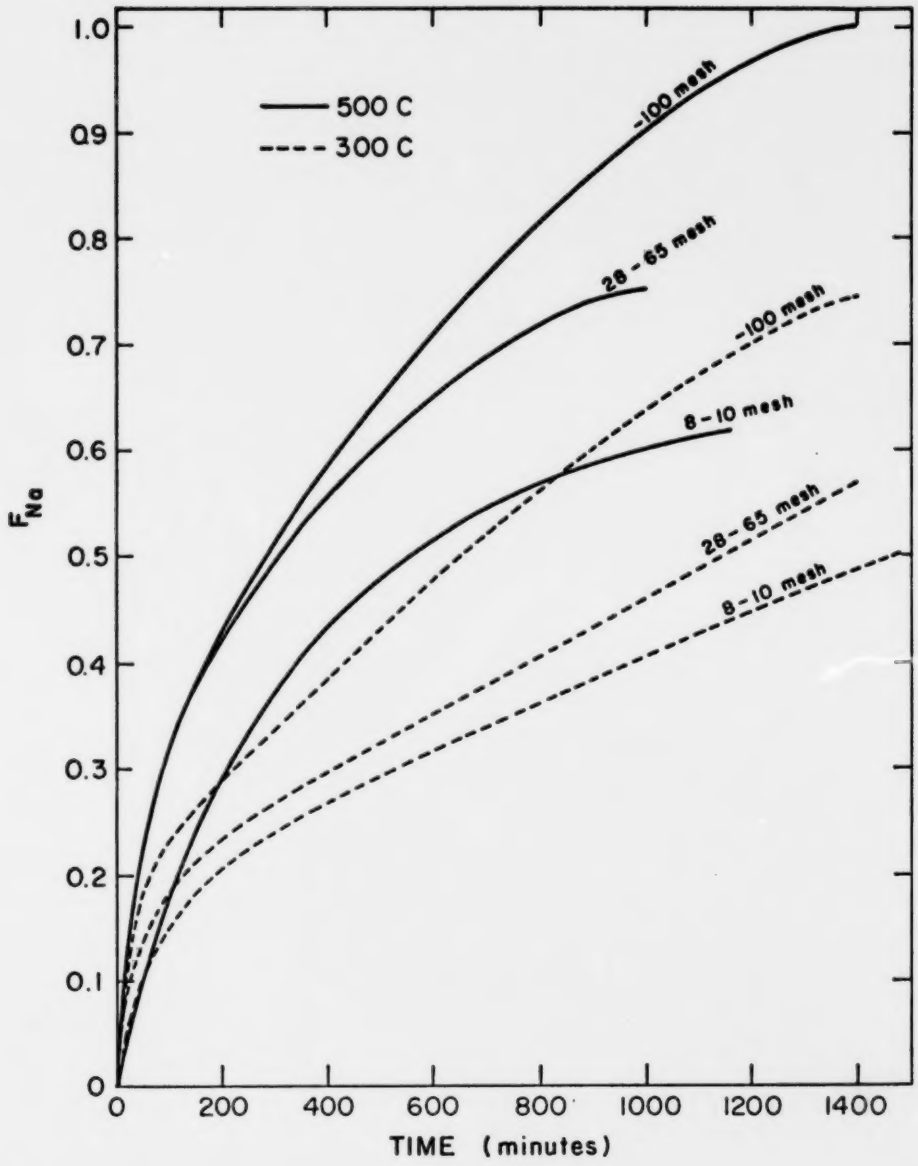


Figure 8. Effect of pellet size on the absorption of $SO_2$ by alkalized alumina in 0.003 atm $SO_2$ (dry) at 300°C and 500°C.

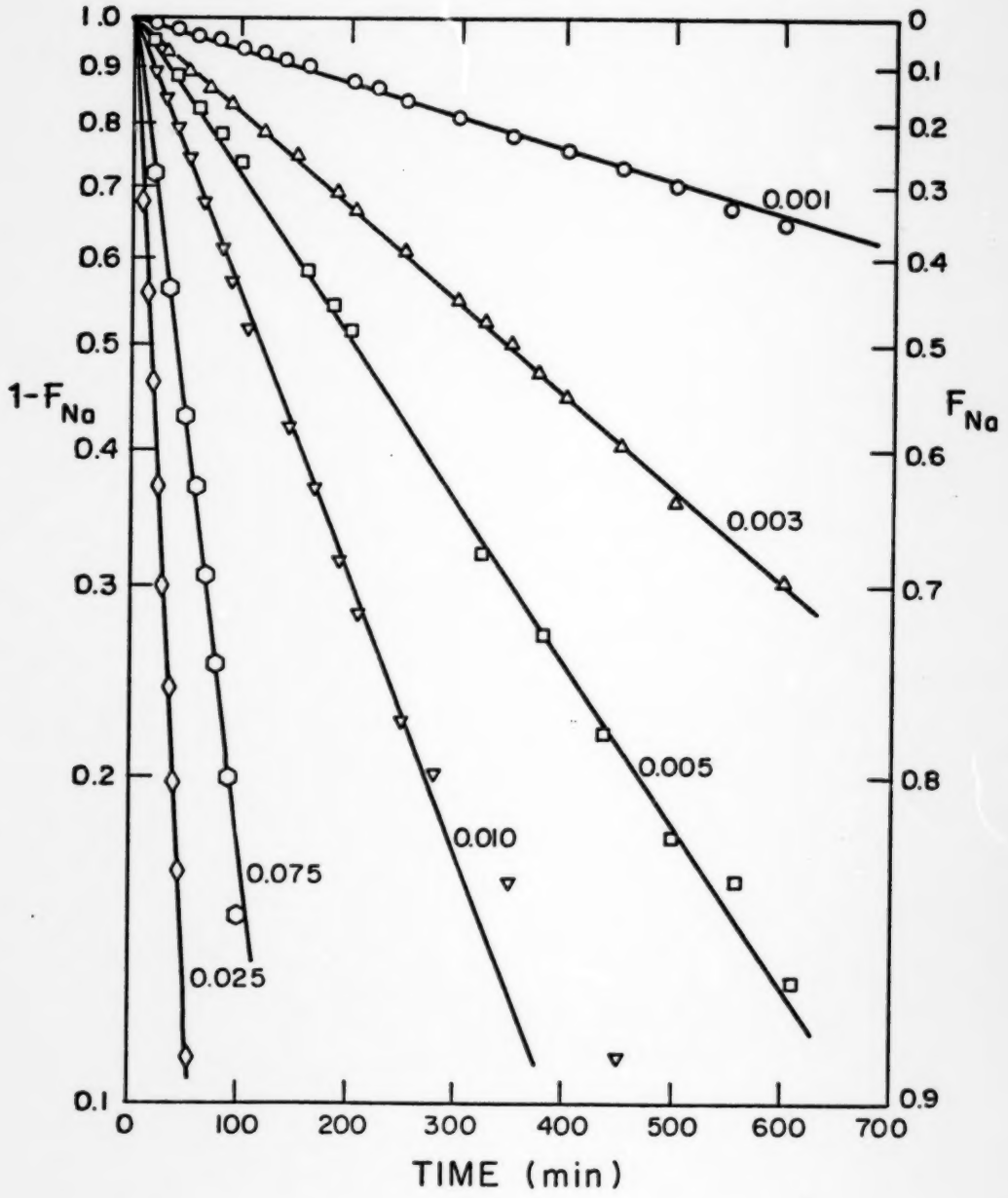


Figure 9. Plot of $\log(1-F_{Na})$ vs. time; with various concentrations of $SO_2$ at 300°C.

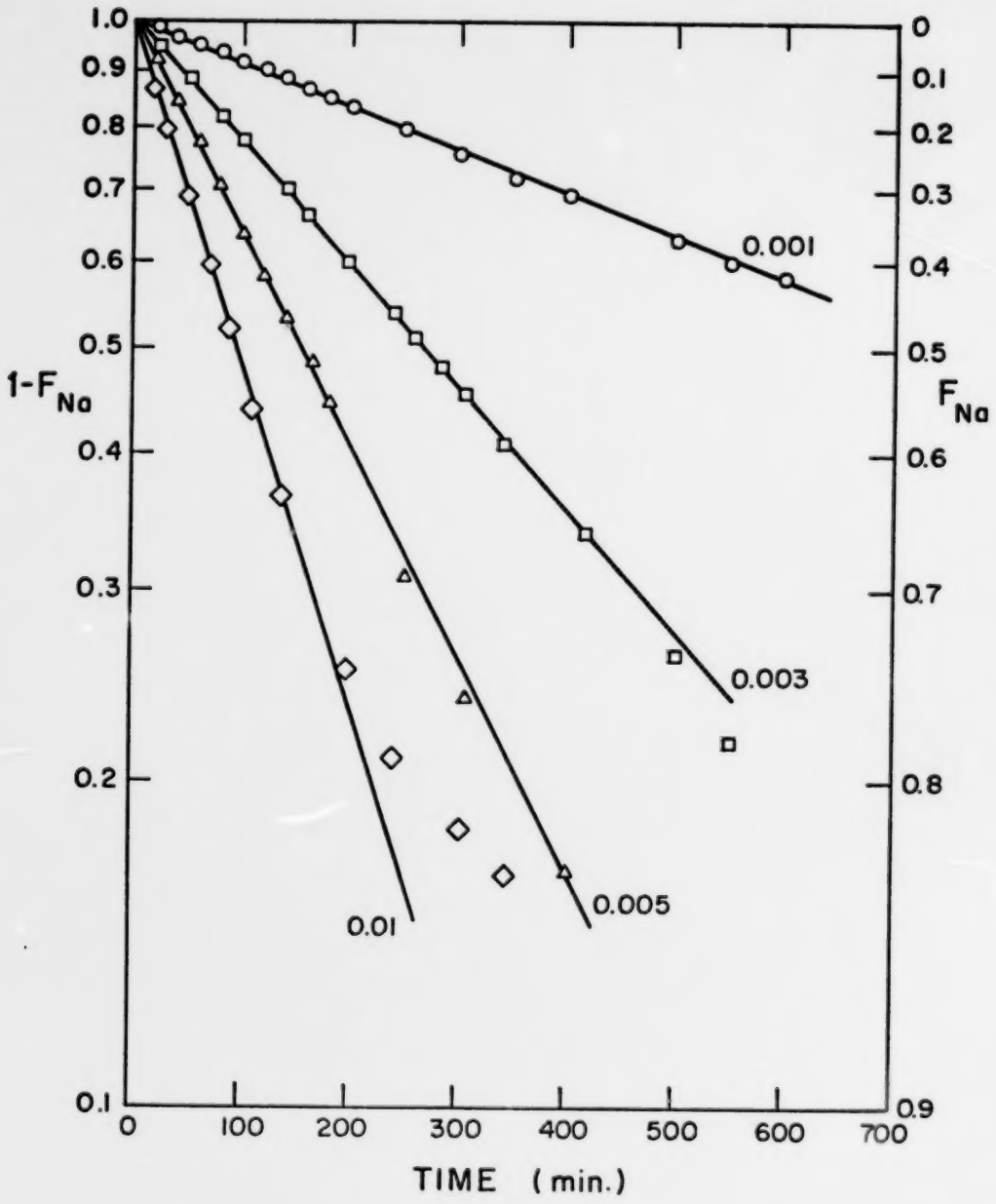


Figure 10. Plot of $\log(1-F_{Na})$ vs. time; with various concentrations of $SO_2$ at 400°C.

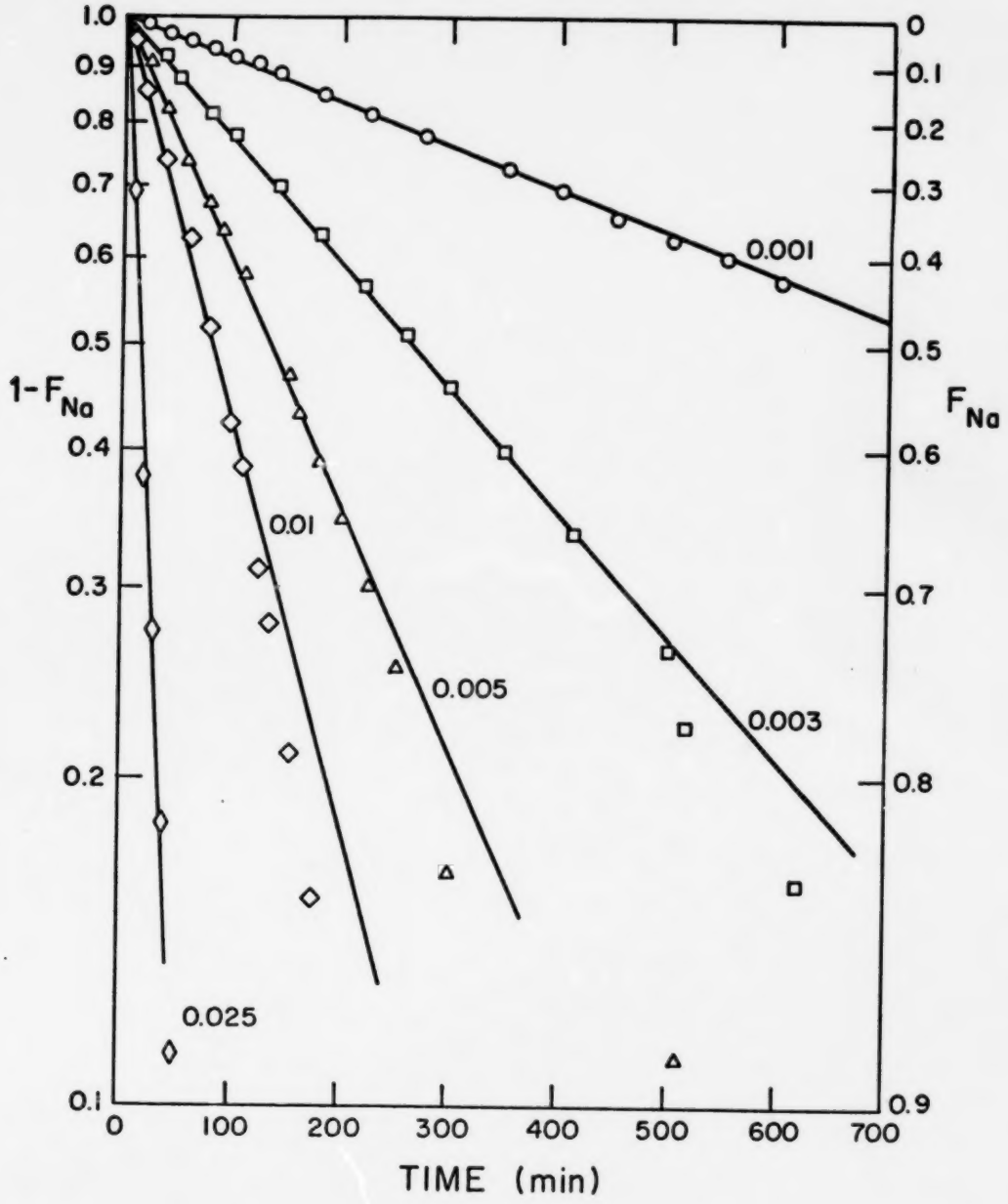


Figure 11. Plot of $\log(1-F_{Na})$ vs. time; with various concentrations of $SO_2$ at 500°C.

$$\log (1-F_{Na}) = \frac{k_{Na} \cdot p_{SO_2}}{2.303} \quad t \qquad (4)$$

Plots of log $(1-F_{Na})$ versus time for wet gas runs at 300°C, 400°C and 500°C are shown in Figures 9, 10 and 11, respectively. In each case a straight line fit is obtained with different slopes for the different $SO_2$ pressures. At 300°C the fit is good out to 90% reaction ($F_{Na} = 0.9$) for those cases where the experiments were conducted over a sufficiently long period. At 500°C the fit is only good to about 70% reaction and the ensuing deviation is caused by the sulfation of alumina, which becomes significant in the later stages at this temperature.

The experimental slopes of the curves in Figures 9, 10 and 11 are plotted versus the sulfur dioxide pressure as open datum points in Figure 12. The closed datum points are the initial rates for dry gas experiments at the same temperatures. These rates were determined from a tangent to the fractional conversion at t = 0. The slopes of three isotherms give the experimental extensive rate constant for the formation of sodium sulfate in alkalized alumina. The initial dry gas experimental rate constants are identical with wet gas rate constants.

An Arrhenius plot of the rate constants for the formation of sodium sulfate is given in Figure 13. The experimental activation energy is $\Delta E = 2.0 \pm 0.5$ kcal.mole$^{-1}$. The experimental rate equation for the formation of sodium sulfate from alkalized alumina in the presence of wet gases is

$$\frac{dF_{Na}}{dt} = 3.85 \exp\left(-\frac{2000}{RT}\right)\left(1-F_{Na}\right)p_{SO_2} \quad (atm^{-1} \cdot min^{-1}) \qquad (5)$$

and the fractional conversion to sodium sulfate is

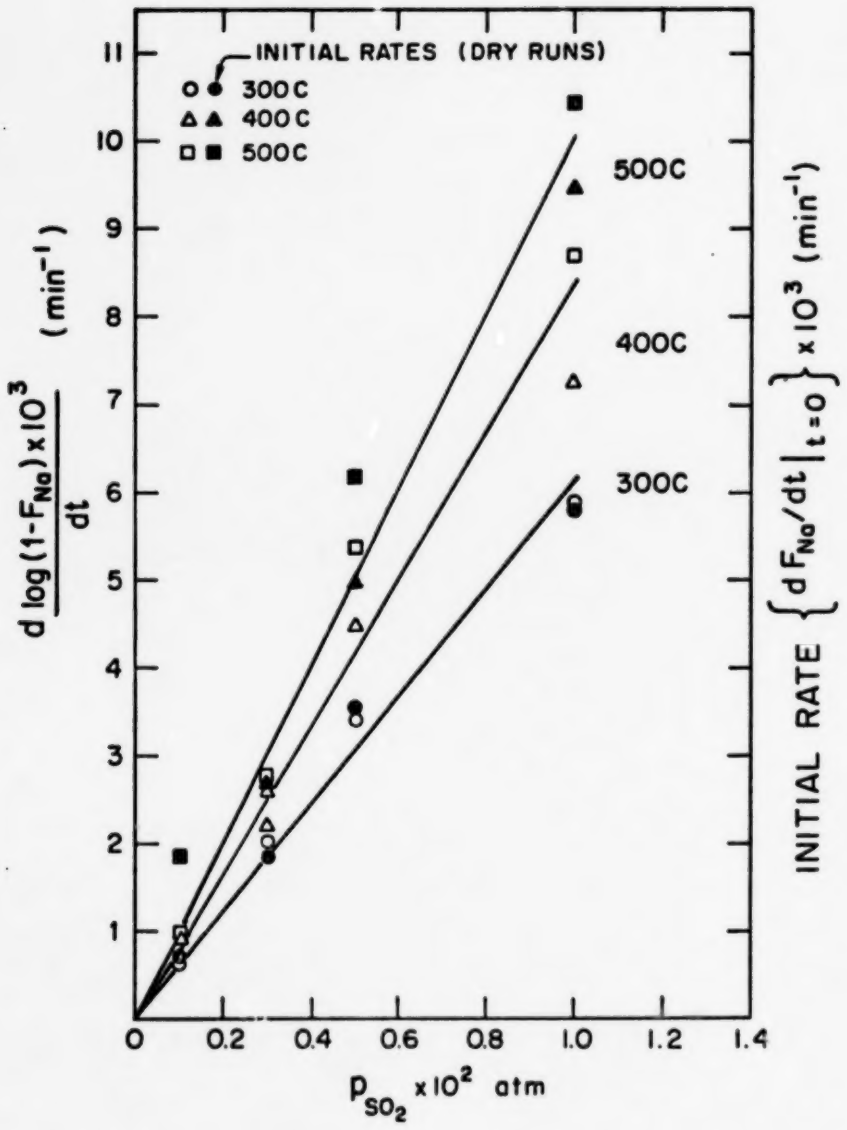


Figure 12. First order dependency of the rate on $p_{SO_2}$.

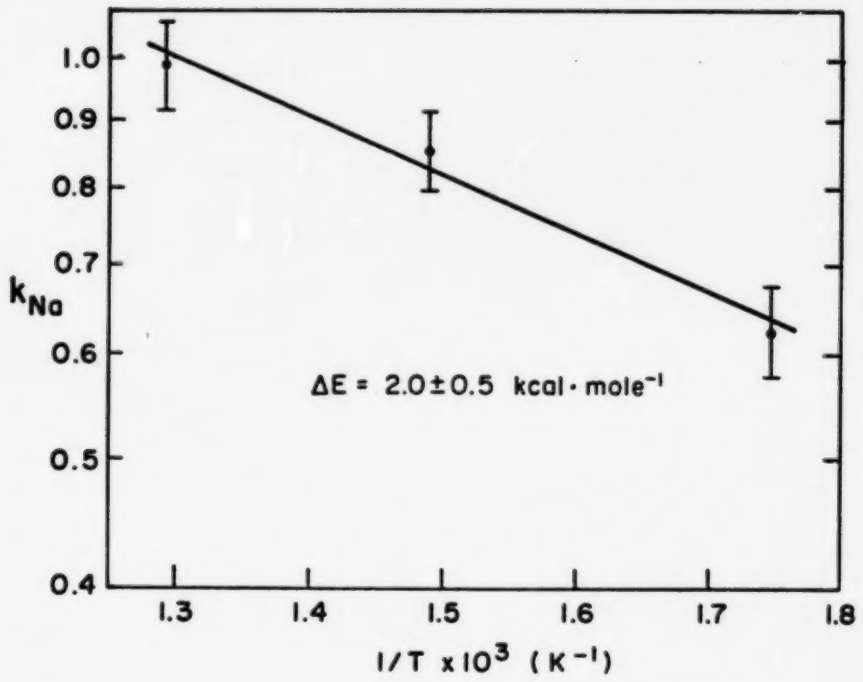


Figure 13. Arrhenius plot of the experimental rate constant for the formation of $Na_2SO_4$ from alkalized alumina.

$$F_{Na} = 1 - \exp\left[-3.85\ p_{SO_2}\ t\ \exp(-2000/RT)\right] \qquad (6)$$

No attempt was made to determine a kinetic expression for the alumina sulfation because of the variable delay for nucleation of the mixed sodium aluminum sulfate. At 500°C the extent of reaction attributible to the sulfation of alumina was computed by subtracting the extrapolated straight line portion of the log $(1 - F_{Na})$ plots from the actual value of log $(1 - F_{Na})$. These values of the weight gain contribution by alumina sulfation were converted to fractional values for the sulfation of alumina, $F_{Al}$, and a new plot of log $(1 - F_{Al})$ versus time was constructed. The results for three experiments in wet gases at 500°C are shown in Figure 14. Note that in each case there is a delay prior to nucleation in which there is no alumina sulfation, $F_{Al} = 0$.

## DISCUSSION OF RESULTS

The initial rates in dry gases are consistent with the rates observed in the presence of small amounts of water vapor, which follow logarithmic kinetics. The subsequent pronounced decrease in the dry gas rates at 300°C does not fit any reasonable mathematical rate expression and is accompanied by a greater decrease in specific surface than occurs in wet gas runs. Therefore, this reduction in rate, which occurs after about 15 to 25% conversion, appears to be a perturbation from normal behaviour caused by a secondary phenomenon, perhaps the blocking of pores by the sodium sulfate produced by the reaction. Small amounts of water vapor may promote recrystallization and short range in situ movements of material that maintain a more open structure.

The overall chemical reaction for the formation of sodium sulfate

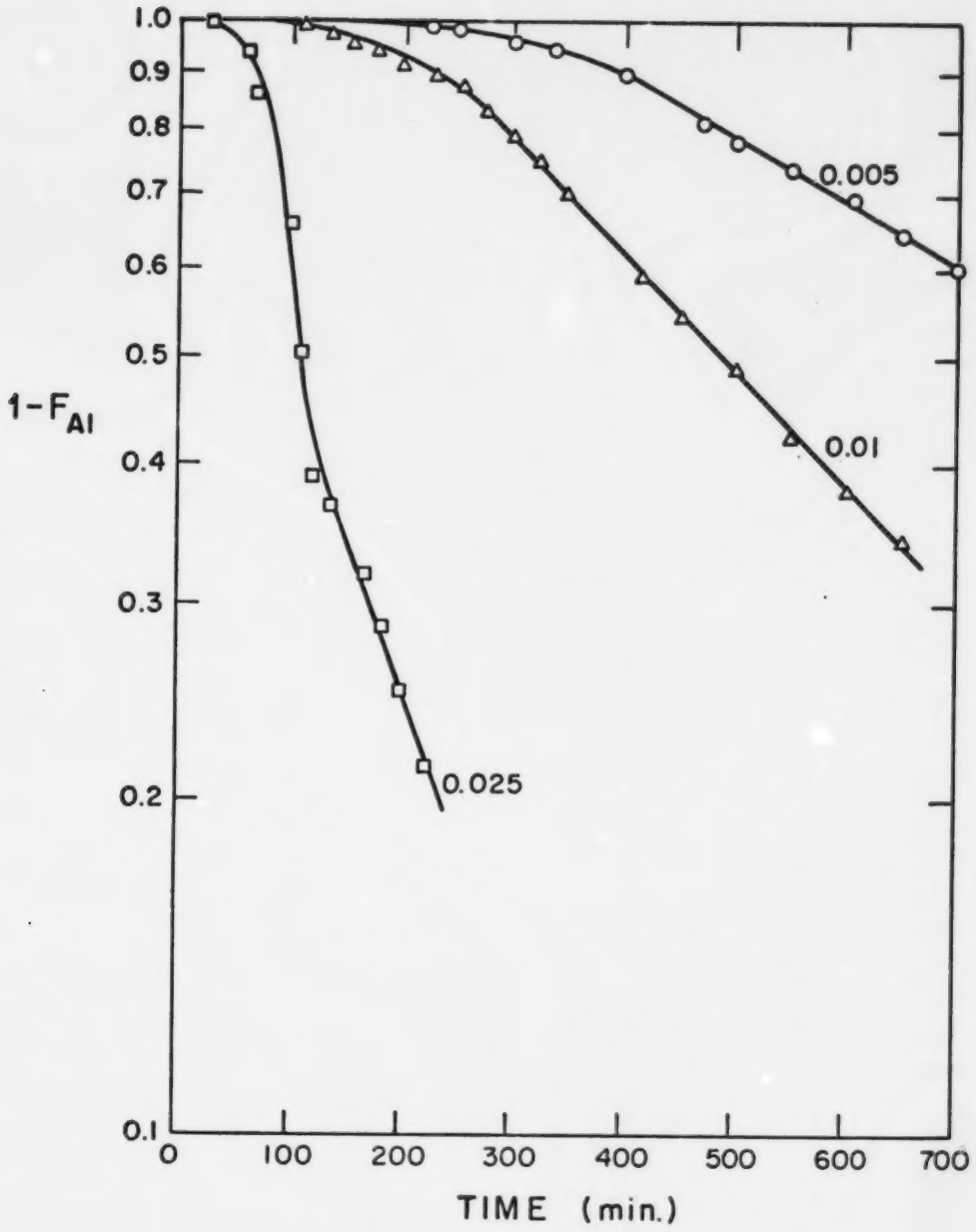


Figure 14. Plot of $\log(1-F_{Al})$ vs. time; at 500°C with various concentrations of $SO_2$.

from alkalized aluminum is

$$Na_2Al_2O_4(c) + SO_2(g) + \frac{1}{2} O_2(g) = Na_2SO_4(c) + Al_2O_3(amorph) \qquad (7)$$

The rate controlling step is probably the formation of sodium sulfite with subsequent oxidation of the sodium sulfite intermediate product to sodium sulfate. This reaction sequence explains the zero order oxygen dependence and the appearance of sodium sulfite at the very beginning of the reaction but without further increase.

A surface chemical reaction model is postulated to control the reaction kinetics. Accordingly, the rate controlling step is preceded by $SO_2$ chemisorption. At the concentrations of $SO_2$ used in this investigation fractional surface coverage is expected to be low, so the concentration of adsorbed $SO_2$ species will be proportional to $p_{SO_2}$. The reaction rate steps may be summarized as follows, with the second step rate controlling:

$$Na_2Al_2O_4\Big|_s + SO_2(g) \overset{k_a}{\rightleftharpoons} Na_2Al_2O_4\Big|_s \cdot SO_2 \quad \text{(equilibrium chemisorption)} \qquad (8)$$

$$Na_2Al_2O_4\Big|_s \cdot SO_2 \overset{k'}{\rightarrow} Na_2SO_3 + Al_2O_3 \quad \text{(slow step)} \qquad (9)$$

$$Na_2SO_3 + \frac{1}{2} O_2 \rightarrow Na_2SO_4 \qquad (10)$$

The last step is moderately fast but it is slow enough to leave measurable amount of $Na_2SO_3$ in the pellets.

The rate of reaction of $SO_2$ is:

$$\frac{dn_{SO_2}}{dt} = -k' \theta A_s \qquad (11)$$

where $A_s$ is the $Na_2Al_2O_4$ reacting surface area, $\theta$ is the fraction of that area covered with adsorbed $SO_2$ and k' is the specific rate constant of the rate controlling step. Since $\theta = k_a p_{SO_2}$ at low adsorption coverage, the rate is:

$$\frac{dn_{SO_2}}{dt} = -k' k_a A_s p_{SO_2} \qquad (12)$$

The experimental rate, $dF_{Na}/dt$ is proportional to $-dn_{SO_2}/dt$ and the experimental rate constant $k_{Na}$ is proportional to $k' k_a A_s$. The small experimental activation energy, E = 1.67 kcal $mole^{-1}$, may have resulted because the necessarily negative adsorption enthalpy associated with $k_a$ offsets the true activation enthalpy (necessarily positive) associated with the surface specific rate constant, k'. It is not possible to separate these constants experimentally.

It is recognized that small activation energies are often associated with a rate process controlled by mass transport in the gas phase, but they need not be. In this case gas phase mass transport in pores had been ruled out on other evidence. Experiments with nitric oxide have yielded additional evidence that the rate of formation of sodium sulfate from alkalized alumina is controlled by a surface chemical reaction rather than mass transport. Experiments in our laboratory show that at 300°C, 0.0005 atm of NO increases the rate by about four times over that observed in wet gases without NO. This effect of NO has been previously reported.[1]

If it is assumed that the reactive surface area $A_s$, averaged over the entire pellet is proportional to the unreacted volume fraction, then

$$A_s = A_o(1 - F_{Na}) \qquad (13)$$

where $A_o$ is the initial reactive area. A more detailed structural-kinetic analysis of micrograins reacting in a porous pellet is presented in Chapter V. As sulfation proceeds, and after reaction is complete, the surface area measured by B.E.T. technique will be greater than the reactive interface area because of the presence of reaction products.

When equation (13) is combined with equation (12) a final rate equation is obtained for the consumption of $SO_2$ to produce sodium sulfate,

$$\frac{dn_{SO_2}}{dt} = -k'k_a A_o(1 - F_{Na})\, p_{SO_2} \qquad (14)$$

that explains the wet gas experiments and is equivalent with the experimental rate expression, equation (2).

## CONCLUSIONS

The kinetics of sulfation of porous alkalized alumina are complex. The primary reaction product is sodium sulfate (I) but at higher temperatures and after a nucleation delay further sulfation results in formation of $Na_3Al(SO_4)_3$. The rate of formation of sodium sulfate is proportional to the $SO_2$ partial pressure and independent of oxygen pressure. This rate is controlled by a surface chemical reaction and is proportional to the fraction of unreacted sample remaining. Hence, the rate decreases logarithmically and approaches complete reaction asymptotically. Appropriate rate equations were derived. If small amounts of water vapor are not present a marked decrease in rate will occur after about 20% reaction that is caused by a secondary phenomenon, probably pore blocking by the sodium sulfate. Small amounts of nitric

oxide increase the rate significantly but this effect was not studied in detail.

NOMENCLATURE

| | |
|---|---|
| $A_o$ | initial surface area of the pellet - $(m^2 \cdot g^{-1})$ |
| $A_s$ | reactive surface area - $(m^2 \cdot g^{-1})$ |
| $F_{Na}$ | fraction of $Na_2O$ reacted - $(g \cdot g^{-1})$ |
| $dF_{Na}/dt$ | rate of sulfation of $Na_2O \cdot Al_2O_3$ - $(min^{-1})$ |
| k' | specific surface rate constant of the rate controlling step |
| $k_a$ | equilibrium constant for chemisorption |
| $k_{Na}$ | experimental rate constant for formation of sodium sulfate - $atm^{-1}\ min^{-1}$) |
| $-dn_{SO_2}/dt$ | rate of disappearance of $SO_2$ (moles $sec^{-1}$) |
| $p_{SO_2}$ | partial pressure of $SO_2$ - (atom) |
| R | gas constant |
| t | time - (min, sec) |
| T | temperature - ($^oK$) |
| $\theta$ | fraction of area covered by adsorbed $SO_2$ |

REFERENCES


(1) Town, J.W., P.E. Sanker, and H.J. Kelly. Alkalized-Alumina Attritioning and $SO_2$ Sorption Rates. Bu. Mines Rept. of Inv.. 7275. 1969. 29 p.

(2) Paige, J.I., J.W. Town, and J.H. Russel. Sorption of $SO_2$ and Regeneration of Alkalized Alumina in Fluidized-Bed Reactors. Bu. Mines Rept. of Inv.. 7414. 1970. 31 p.

(3) Bienstock, D., J.H. Field, and J.H. Myers. Process Development in Removing Sulfur Dioxide from Hot Flue Gases (in Four Parts). 3. Pilot Plant Study of the Alkalized Alumina System for $SO_2$ Removal. Bu. Mines Rept. of Inv.. 7021. 1967. 52 p.

(4) Russel, J.H., J.W. Town, and H.J. Kelly. Mathematical Evaluation of $SO_2$ Sorption - Regeneration Reactions with Alkalized Alumina. Bu. Mines Rept. of Inv.. 7415. 1970. 29 p.

(5) Kubaschewski, O., E.Li. Evans, and C.B. Alcock. Metallurgical Thermo Chemistry. Pergamon Press Ltd., 1967. p. 304-408.

(6) Bienstock, D., and J.H. Field, (assigned to United States of America). Process for the Removal of Sulfur Oxides from Gases. U.S. Pat. 2,992,884 July 18, 1961.

(7) Ciapetta, F.G., P.K. Mather, and T.O. Tongue. Development of Improved Alkalized-Alumina for $SO_2$ Removal. Davison Chemical Division of W.R. Grace and Co.. Clarkeville, Md.. Interim Rept.. Nov. 30, 1967. p. 77.

(8) Chao, T., and S.C. Sun. Study on Sulfation of Alumina with Gaseous Sulfur Trioxide . Trans. Soc. Mining Engrs.. 238:425, Dec. 1967.

## KINETICS OF SULFATION OF REDUCED ALUNITE ($K_2O \cdot 3Al_2O_3$)

### INTRODUCTION

Fuel combustion is the chief source of air pollution by sulfur dioxide, and about 18 million tons of sulfur dioxide are being emitted annually by power generating plants in the United States[1]. Both liquid scrubbing techniques and sorption by dry solids are being considered for the removal of sulfur dioxide that occurs in dilute concentration in power plant gases. Dry, elevated temperature sorption processes retain the buoyancy of the stack gases for maximum dispersion in the atmosphere after treatment.

Among the dry processes are absorption by metal oxides to form sulfites or sulfates, with subsequent regeneration of the oxide and recovery of sulfur in a concentrated form. Alkalized alumina ($Na_2O \cdot Al_2O_3$) developed by U.S. Bureau of Mines was proved to be an excellent regenerable sorbent for sulfur dioxide[2]. The mineral alunite, a hydrated potassium aluminum sulfate ($K_2O \cdot 3Al_2O_3 \cdot 4SO_3 \cdot 6H_2O$) is chemically similar to the final sulfated product of alkalized alumina. Heating alunite at 700°C decomposes the aluminum sulfate to oxide[3]. Hydrogen reduction converts all the sulfate to hydrogen sulfide and oxides. The oxides thus generated react with sulfur dioxide and oxygen to form sulfates. Hence, the generation of the sorbent from alunite is essentially the same as the regeneration of an alkalized alumina sorbent or the regeneration of reduced alunite after $SO_2$ absorption.

Alunite is found in several locations in the western United States and the estimated reserves recoverable by inexpensive surface mining are over 500 million tons.[7] The purpose of the present study was to investigate the sulfation kinetics of hydrogen reduced alunite.

## MATERIALS AND EXPERIMENTAL METHOD

Pelletized alunite from Marysvale, Utah was used in this study. The mineral was crushed to -100 mesh, mixed with 5% bentonite and 10% water, and pressed at 1000 psi. The 1/2 inch disc pellets were then dried at 525°C and stored. Pellets were thermally decomposed or reduced with hydrogen in small batches in a horizontal tube furnace as required for the sulfation kinetic studies.

The absorption of sulfur dioxide by hydrogen reduced alunite pellets was investigated under various isothermal and constant atmospheric conditions using a quartz helix balance, from which the specimens were suspended. The thermogravimetric analysis was supplemented by X-ray diffraction, chemical analyses and electron beam microporbe analyses. Surface area measurements were made on the pellets before and after reaction and scanning electron microscopy was used to observe the fractured surfaces.

## OPTIMUM HYDROGEN REDUCTION OF ALUNITE AND SORBENT REGENERATION

Chemical analyses showed that the sulfur content of alunite reduced in hydrogen at 800°C for 60 minutes was about 2% while that of calcined alunite was about 9%. The heating decomposes only the aluminum sulfate, while the presence of hydrogen is necessary for the reduction of potassium sulfate.

$$K_2O \cdot 3Al_2O_3 \cdot 4SO_3 \cdot 6H_2O \xrightarrow{511^oC} K_2O \cdot 3Al_2O_3 \cdot 4SO_3 + 6H_2O$$

$$K_2O \cdot 3Al_2O_3 \cdot 4SO_3 \xrightarrow{700^oC} K_2SO_4 + 3Al_2O_3 + 3SO_2 + \frac{3}{2} O_2$$

$$K_2SO_4 + 4H_2 \xrightarrow{600^oC} K_2O + H_2S + 3H_2O$$

This was also confirmed by X-ray diffraction of the pellets, which exhibited strong peaks of $K_2SO_4$ for calcined pellets while the reduced alunite was amorphous.

Fig. 1 compares the absorption of $SO_2$ by calcined alunite and alunite previously reduced in hydrogen. The thermogravimetric sorption curves were obtained at 500°C in a gas mixture of 0.003 atm $SO_2$, 0.024 atm $H_2O$ and oxygen at a total pressure of one atmosphere. Since the $SO_2$ absorption capacity of reduced alunite was about 2.5 times that of the calcined alunite, the remaining study emphasized reduced alunite.

Fig. 2 shows the $SO_2$ absorption at 500°C in 0.003 atm $SO_2$ by alunite previously reduced at various temperatures for 120 minutes. Although the $SO_2$ absorption rate increases with increasing reduction temperature to 800°C, there is no apparent increase between 800°C and 900°C, and the reduction treatment at 1000°C actually reduces the absorption capacity somewhat. Although the rate of reduction increases with the temperature, the rate of volatilization of $K_2SO_4$ and permanent loss of potassium also increases. Consequently, 800°C seems to be the optimum reduction temperature, balancing reduction losses with vapor losses.

Fig. 3 gives the absorption of $SO_2$ by alunite previously reduced in hydrogen at 800°C for various periods, which are indicated on the figure. These data show that there is no apparent increase in the reduction and absorbent effectiveness if the reduction period at 800°C is extended beyond 60 minutes. Consequently, hydrogen reduction of alunite

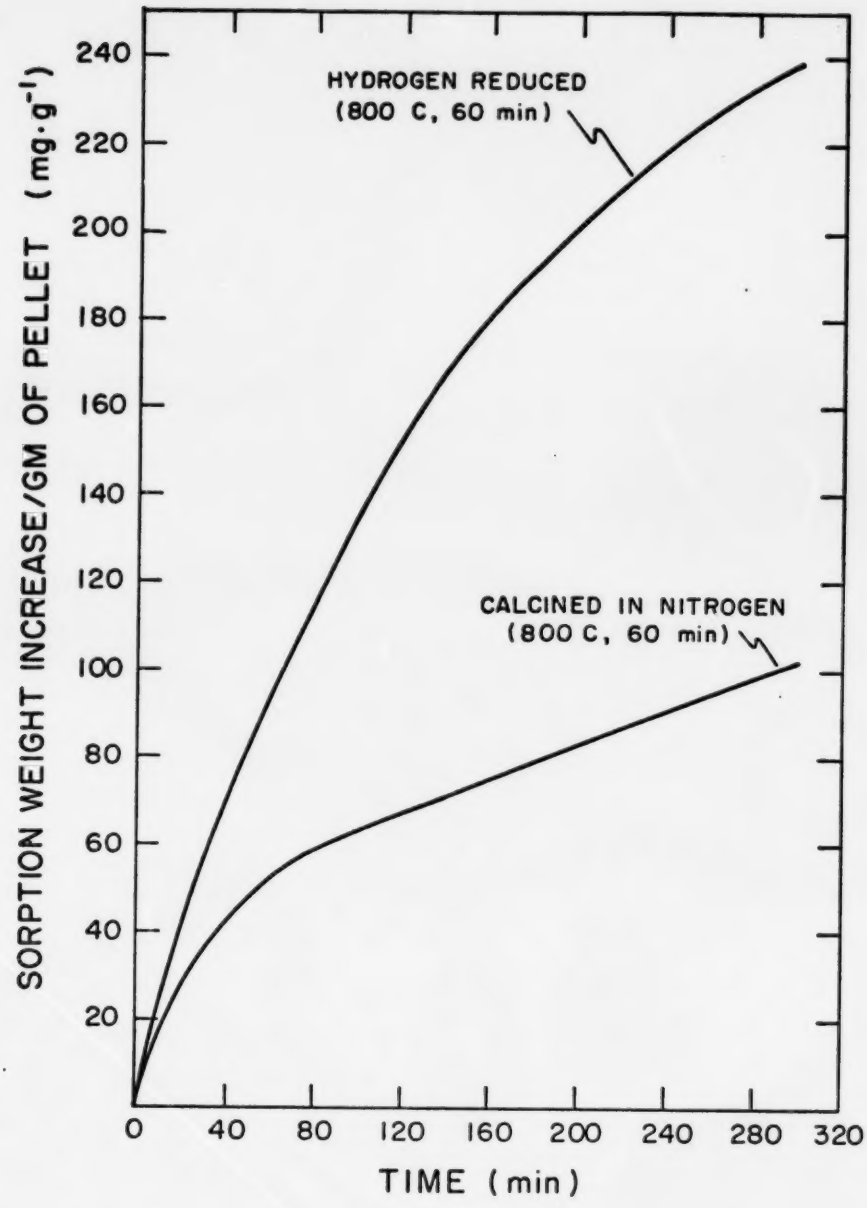


Figure 1 Absorption of $SO_2$ by alunite (reduced or calcined at 800°C for 60 min); with 0.003 atm $SO_2$ and 0.024 atm water vapor at 500°C.

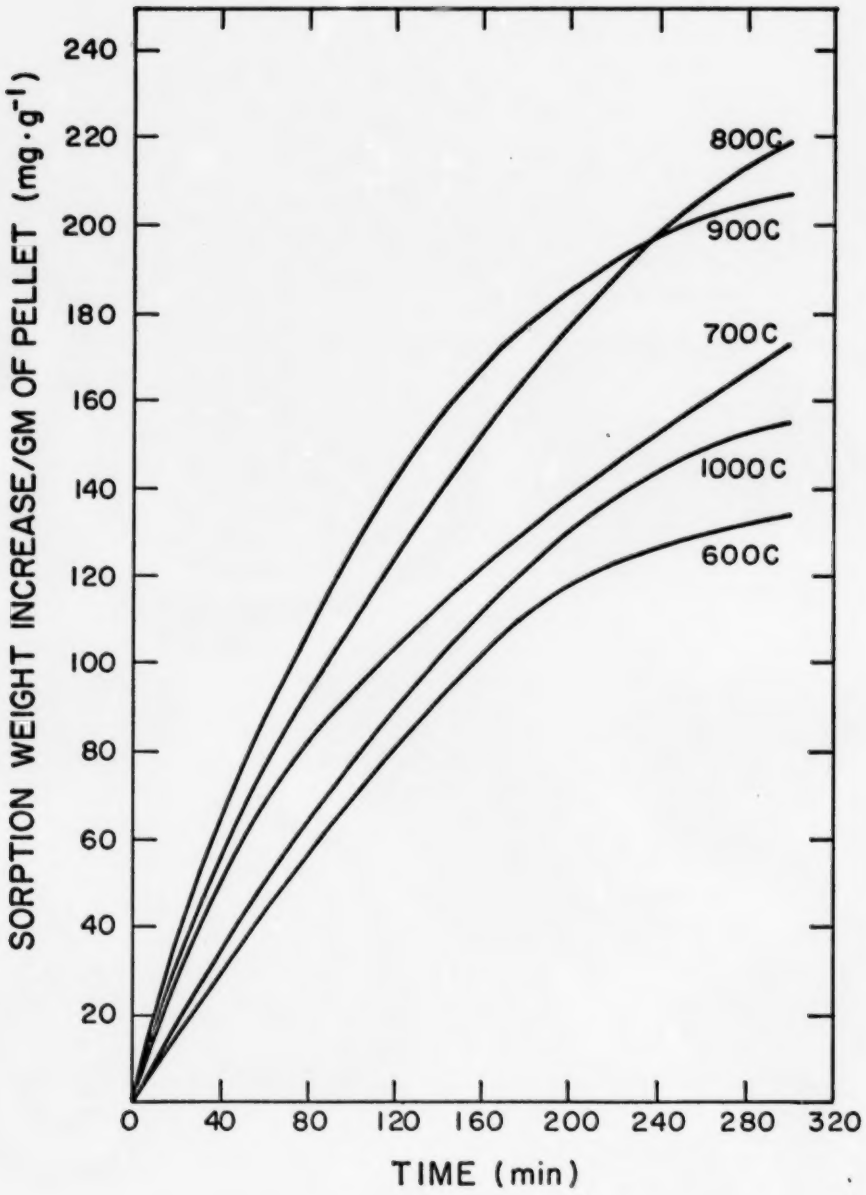


Figure 2 Absorption of $SO_2$ by alunite (reduced at various temperatures for 120 min); with 0.003 atm $SO_2$ and 0.024 atm water vapor at 500°C.

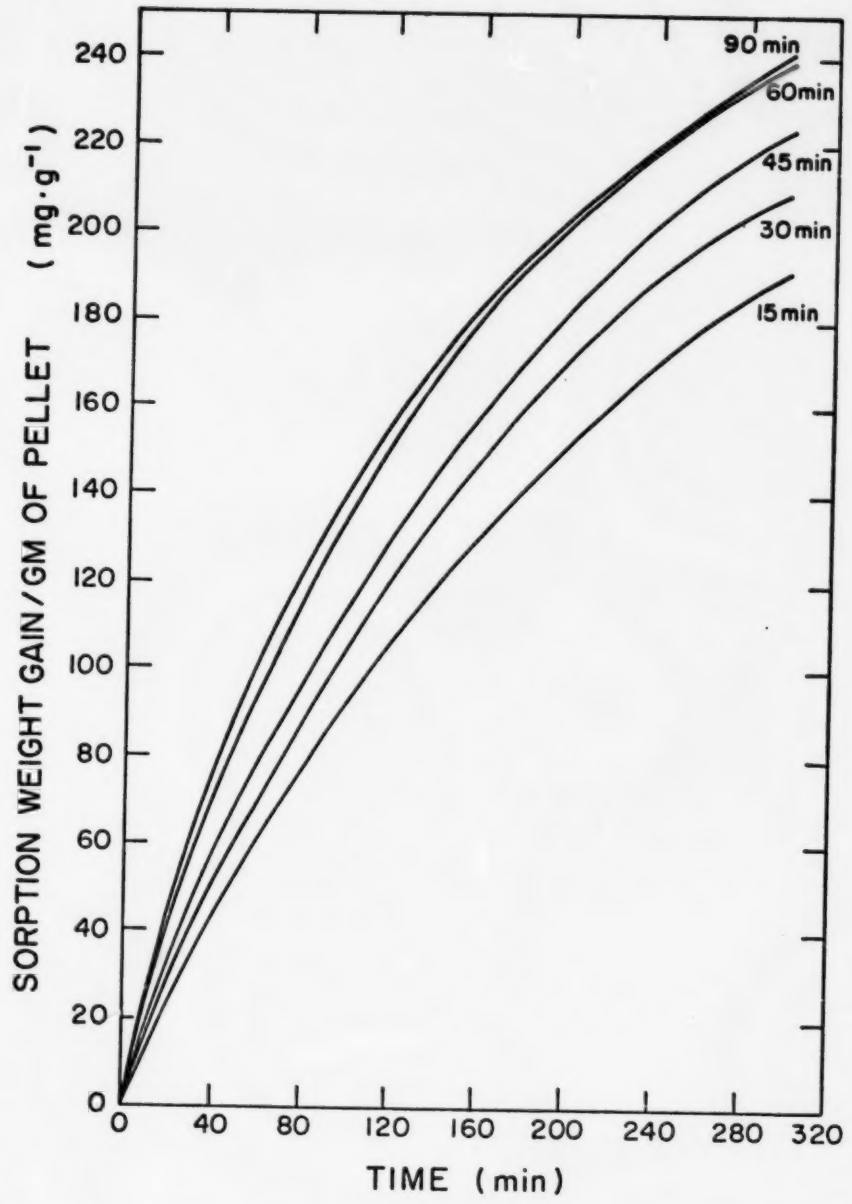


Figure 3. Absorption of $SO_2$ by alunite (reduced at 800°C for various periods); with 0.03 atm $SO_2$ and 0.024 atm water vapor at 500°C.

at 800°C for 60 minutes was adopted as a standard procedure for further pellet preparation. The chemical and physical properties of this hydrogen reduced alunite are summarized in Table I.

Table I. PROPERTIES OF ALUNITE REDUCED IN HYDROGEN

(800°C, 60 min.)

| | |
|---|---|
| Chemical Analysis: | |
| Potassium oxide ($K_2O$) | 21.0 wt. % |
| Aluminum oxide ($Al_2O_3$) | 62.0 |
| Silica ($SiO_2$) | 8.4 |
| Sulfite ($SO_3^{--}$) | 4.8 |
| Physical Properties: | |
| Surface area, $A_o$ | 24±1 $m^2 \cdot g^{-1}$ |
| Porosity | 64% |
| Crushing strength | 14.1 Kg $cm^{-2}$ |

SULFATION EXPERIMENTAL RESULTS

The kinetics of $SO_2$ absorption by hydrogen reduced alunite were investigated from 100 to 500°C using sulfur dioxide partial pressures from 0.001 to 0.025 atm. The effect of oxygen partial pressures from 0.001 to 1 atm was also studied. Both dry gases and gas mixtures containing up to 0.084 atm of water vapor were used. The dependence of the rate of sorption with various pellet sizes was also investigated.

Temperature

The rate of absorption increases with temperature. Fig. 4 illustrates the absorption of $SO_2$ by reduced alunite at various temperatures.

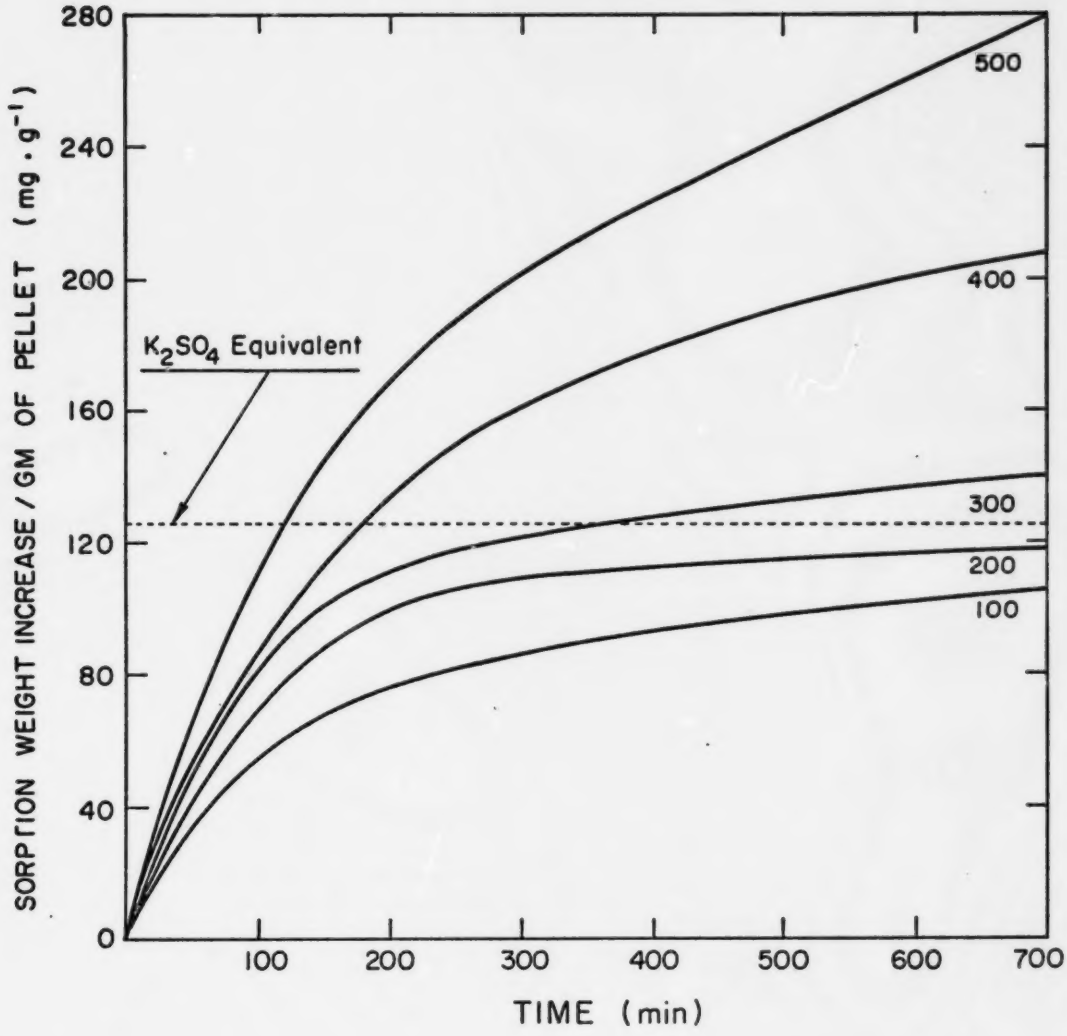


Figure 4. Absorption of $SO_2$ by reduced alunite at various temperatures; with 0.003 atm $SO_2$ and 0.024 atm water vapor.

Below 300°C the rate becomes negligibly small when the weight increase corresponding to the sulfation of all $K_2O$ in the pellets has been reached. This limit is indicated by the horizontal dashed line in Fig. 4. X-ray diffraction shows $K_2SO_4$ to be the only phase present. Hence, below 300°C sulfation of $K_2O$ accounts for essentially all of the absorption.

Above 300°C a new phase, $K_3Al(SO_4)_3$, appears. There is no X-ray diffraction evidence of the presence of aluminum sulfate or aluminum sulfite. This evidence suggests that above 300°C alumina also begins to sulfate, but the aluminum sulfate combines immediately with potassium sulfate to form the mixed compound. As the sorption of $SO_2$ nears completion another mixed compound, $KAl(SO_4)_2$, appears as the final product in the X-ray diffraction patterns. This compound is identical with dehydrated alunite. The rate of sulfation becomes negliglibly small when the weight increase corresponding to the stoichiometric formation of $KAl(SO_4)_2$ in the pellets has been reached. The excess alumina present at this stage, as in alunite, is not sulfated.

Sulfur Dioxide Concentration

Fig. 5 shows the amount of $SO_2$ absorbed at 200 and 500°C, for various partial pressures of $SO_2$. Oxygen and 0.024 atm of water vapor were also present. The initial absorption rates determined from the slopes of the weight gain curves at zero time increase linearly with the $SO_2$ concentration. The rate decreases with increased sulfation of the solid and becomes zero asymptotically as the absorption capacity of reduced alunite is reached.

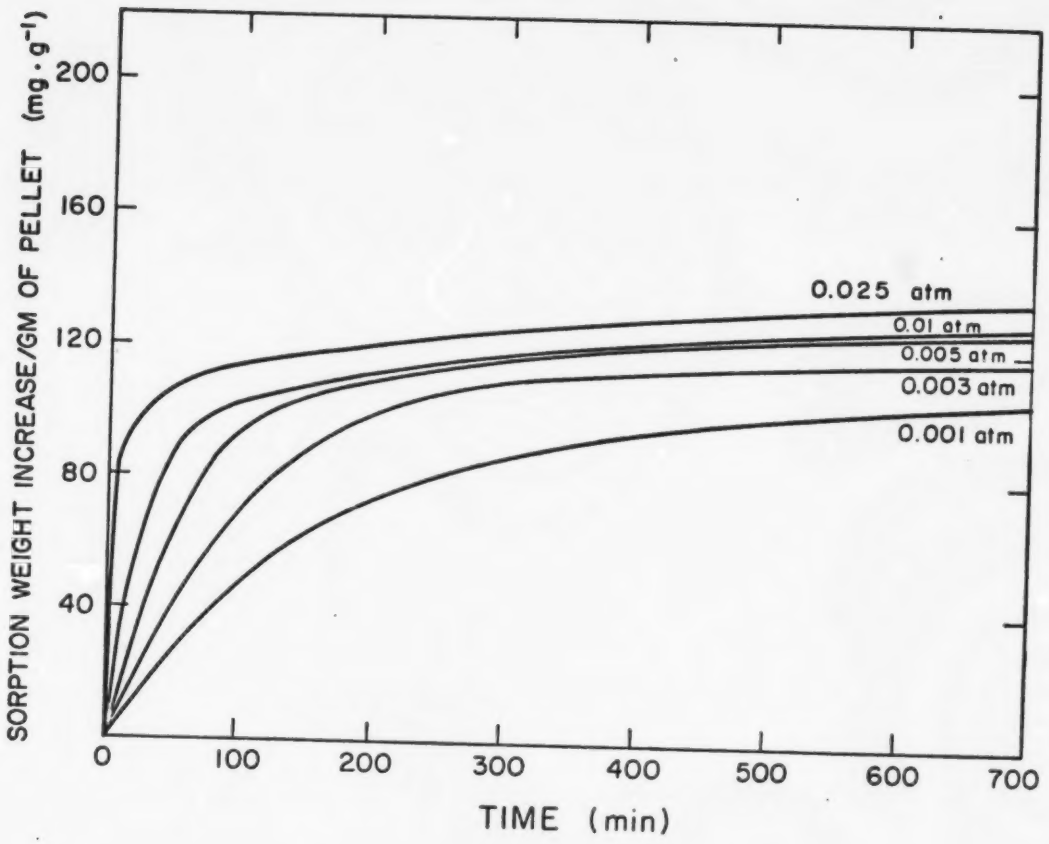


Figure 5a. Absorption of $SO_2$ by reduced alunite at 200°C; with 0.024 atm water vapor and various concentrations of $SO_2$.

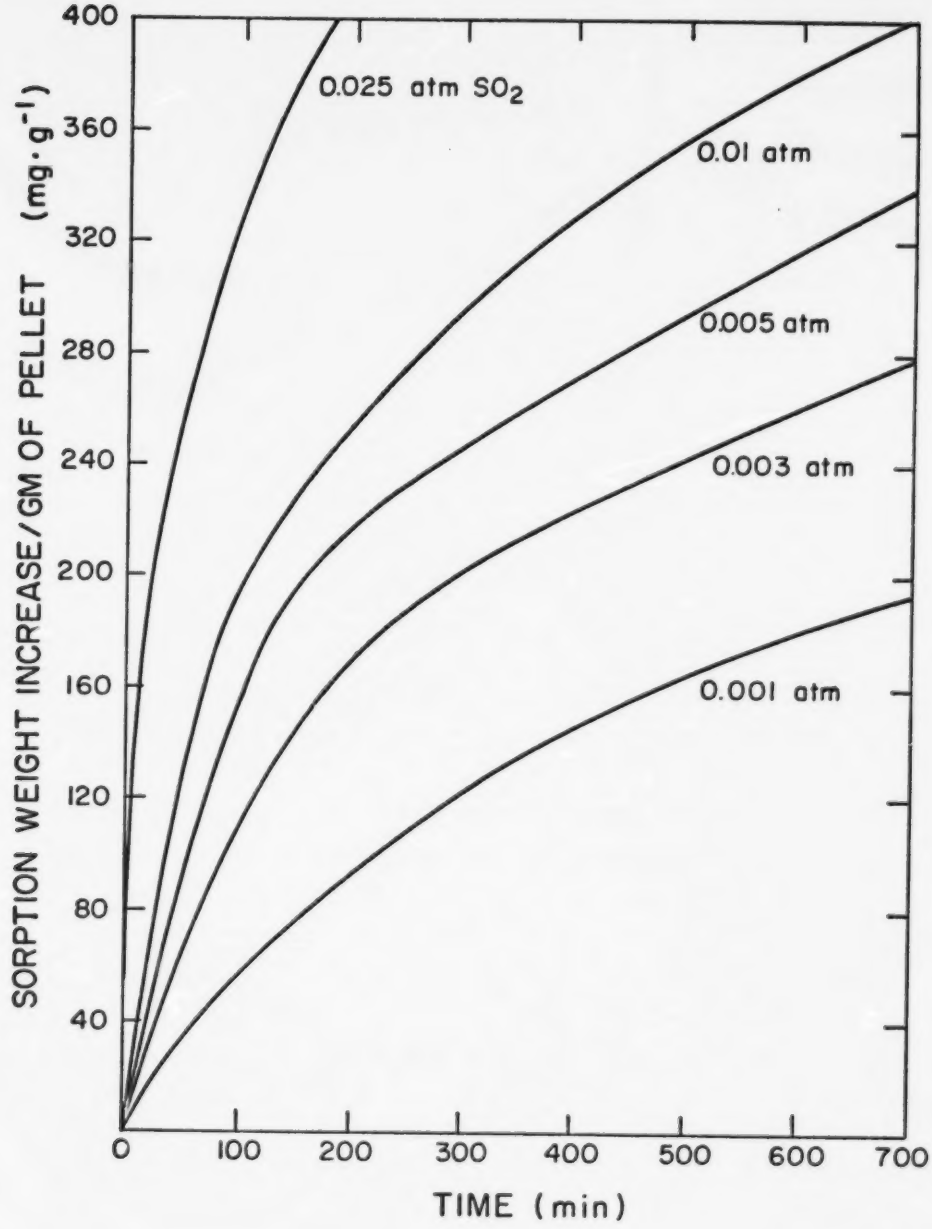


Figure 5b. Absorption of $SO_2$ by reduced alunite at 500°C; with 0.024 atm water vapor and various concentrations of $SO_2$.

Oxygen Concentration

The effect of oxygen partial pressure was investigated in the absence of water vapor. At 200°C the oxygen concentration has little effect on the rate of absorption. At 500°C, the initial rate is independent of $p_{O_2}$, but in the later stages of absorption, the rate becomes a function of the oxygen concentration. Fig. 6 shows the effect of oxygen concentration on the absorption at 500°C. Since the early sulfation primarily involves $K_2O$, these results indicate that the formation of $K_2SO_4$ is independent of oxygen partial pressure, while the formation of potassium aluminum sulfate (or aluminum sulfate) is proportional to the square root of oxygen partial pressure. The sulfation of potassium oxide may proceed through an intermediate sulfite formation step which is rate controlling and independent of oxygen. Aluminum sulfite is thermodynamically unstable at the experimental conditions used.

Water Vapor

The effect of water vapor from 0 to 0.084 atm $p_{H_2O}$ on the reaction kinetics was investigated. The rates were independent of water vapor at 500°C, as shown in Fig. 7. At low temperatures, 200°C, the initial rates were also independent of water vapor, but as the reaction proceeds the rate decreases markedly for reaction in dry gases. Above $p_{H_2O} = 0.01$ atm , water vapor has little effect on the reaction kinetics at any temperature.

It should be noted that water vapor is not a reactant in the sulfation chemical process but acts as a promoter. The presence of NO in the gas mixture had a similar effect. A similar catalytic behavior is observed for the sulfation of alkalized alumina.[4] Surface area measurements on the pellets reacted with dry and wet gases showed that there

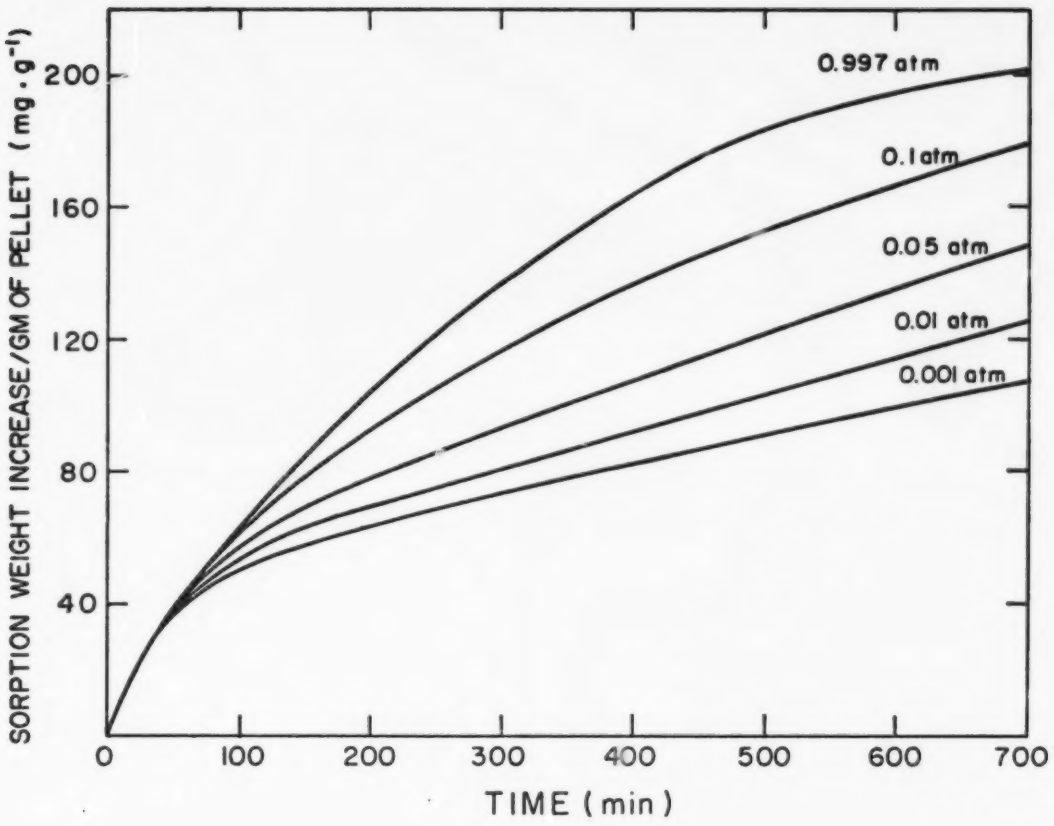


Figure 6. Effect of oxygen partial pressure on the absorption of $SO_2$; with 0.003 atm $SO_2$ (dry) at 500°C.

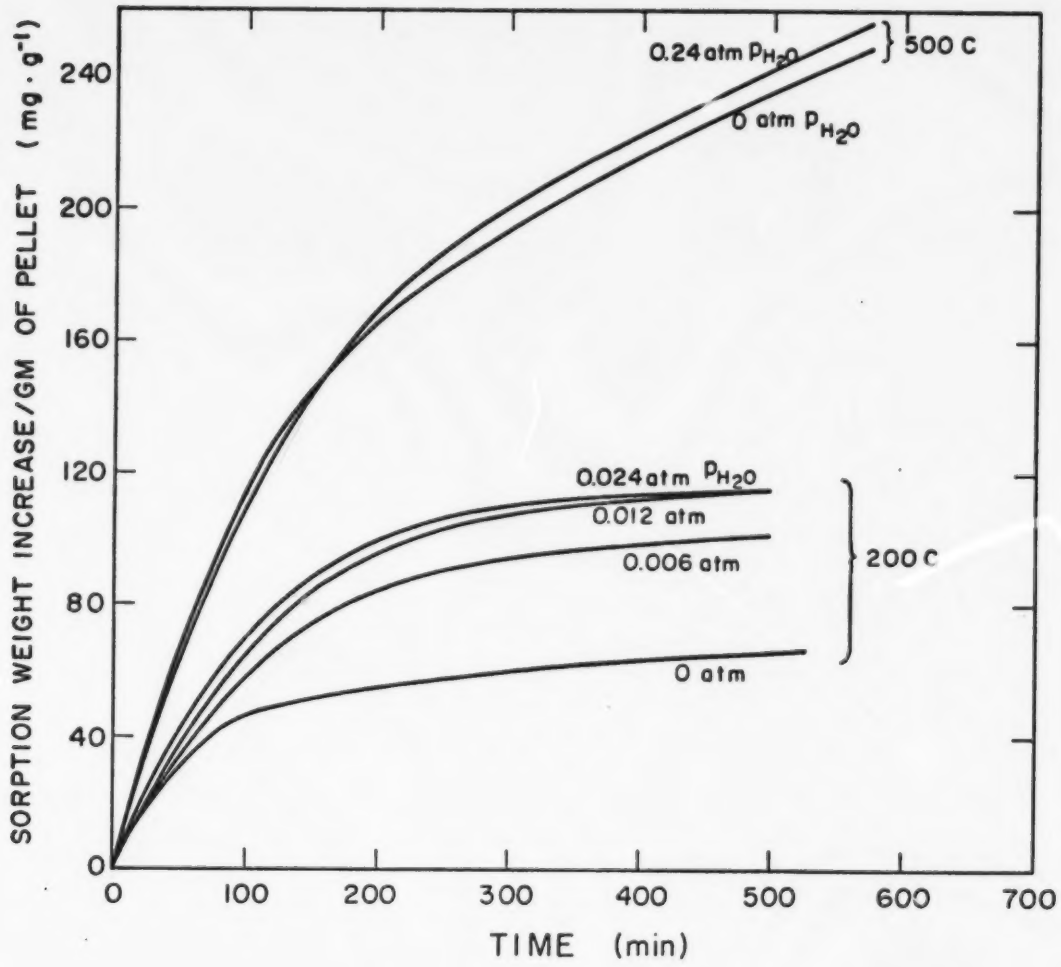


Figure 7. Effect of water vapor on the absorption of $SO_2$; with 0.003 atm $SO_2$ and various partial pressures of water vapor at 200°C and 500°C.

was a drastic reduction in the surface area after reaction with dry $SO_2$ and $O_2$ at low temperatures. Reaction with wet gases caused only moderate surface area reduction. Blocking of pores by the sulfation products probably accounts for the reduction in surface area. This reduction in available surface area for further reaction also accounts for the marked decrease in the extensive sulfation rate as reaction proceeds in dry $SO_2$ at low temperatures.

Pellet Size

The effect of particle size was also investigated using crushed pellets. The standard pellets were 12.7 mm in diameter and about 1.9 mm in thickness. After reduction they were crushed and sieve size fractions of 0.5, 0.25 and 0.125 mm diameter grains were subjected to sulfation kinetic experiments at 500°C, where the fastest rates were obtained. The particle size had little effect on the sulfation rate. Since the rates remain constant with decreasing particle size, it can be concluded that large scale pore diffusion within the pellet is not an important factor in the reaction kinetics. This was also confirmed by microprobe sulfur analyses of cross sectioned pellets. Although there were random point-to-point fluctuations, the average sulfur content traversing the specimen was uniform.

DISCUSSION OF RATE MECHANISM BELOW 300°C - SULFATION OF $K_2O$

It was noted earlier that the sulfation of $K_2O$ is the main reaction below 300°C, while there is sulfation of both $K_2O$ and $Al_2O_3$ above 300°C. It is convenient to divide the discussion of rate mechanisms accordingly.

A term $F_{K_2O}$ is defined as the fraction of $K_2O$ that has already

reacted to form $K_2SO_4$.

$$F_{K_2O} = w/W_K$$

where w is the weight change at any time and $W_K$ is the maximum weight gain corresponding to the stoichiometric sulfation of $K_2O$ in the pellets.

When $\log_e\left(1-F_{K_2O}\right)$ was plotted against reaction time we obtained a straight line with a y intercept of zero for all wet sulfation kinetic experiments at 300°C and lower temperatures. Three typical experiments in 0.003 atm $p_{SO_2}$ at different temperatures are shown in Fig. 8. Differentiating the integral expression,

$$\log_e\left(1-F_{K_2O}\right) = k'_{K_2O}t \quad , \tag{1}$$

yields the following rate expression with the rate proportional to the unreacted volume fraction

$$\frac{dF_{K_2O}}{dt} = k'_{K_2O}\left(1-F_{K_2O}\right) \tag{2}$$

where $k'_{K_2O}$ is the slope of the experimental plot of $\log_e\left(1-F_{K_2O}\right)$ vs. time.

The rate increases with the partial pressure of $SO_2$ as shown for five runs at 200°C in Fig. 9. When the experimental rate constant $k'_{K_2O}$ is plotted against $p_{SO_2}$ a straight line was obtained indicating a first order dependence on $p_{SO_2}$. This is shown in Fig. 10.

A first order irreversible heterogeneous rate equation for sulfation of $K_2O$ would be expressed as

$$\frac{dF_{K_2O}}{dt} = k_{K_2O}\cdot A_r \cdot p_{SO_2} \tag{3}$$

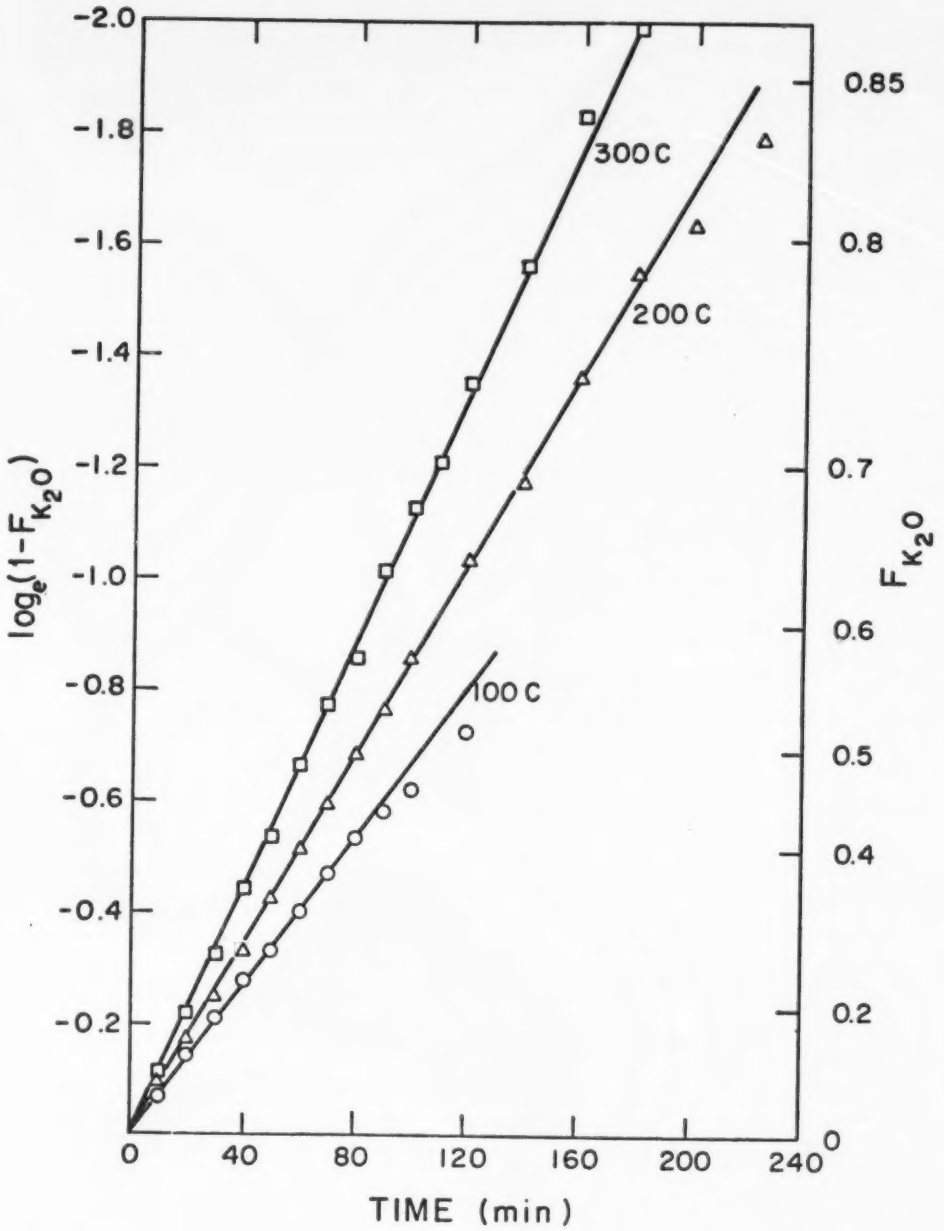


Figure 8. Plot of $\log_e(1-F_{K_2O})$ vs. time; with 0.003 atm $SO_2$ and 0.024 atm water vapor at various temperatures.

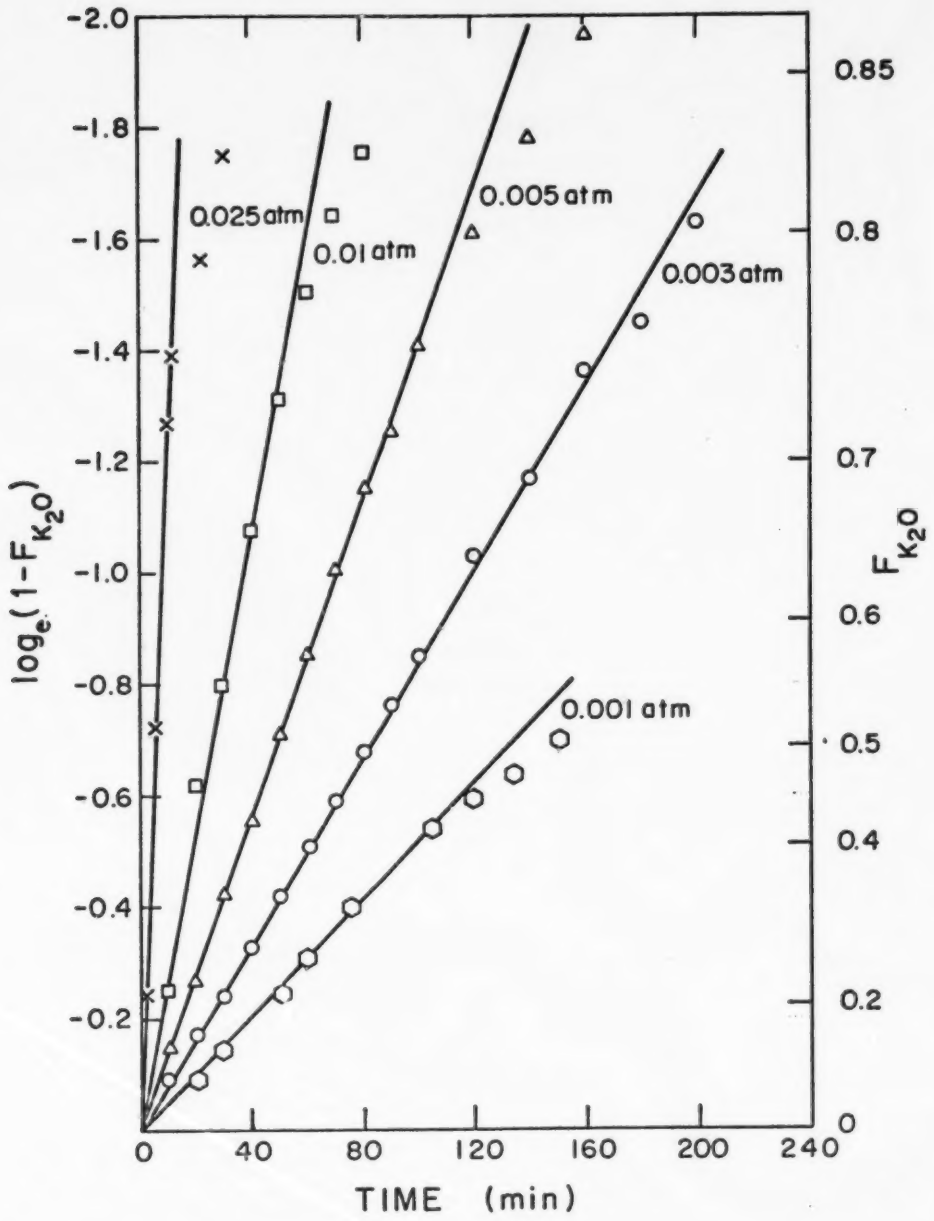


Figure 9. Plot of $\log_e(1-F_{K_2O})$ vs. time; with various concentrations of $SO_2$ and 0.024 atm water vapor at 200°C.

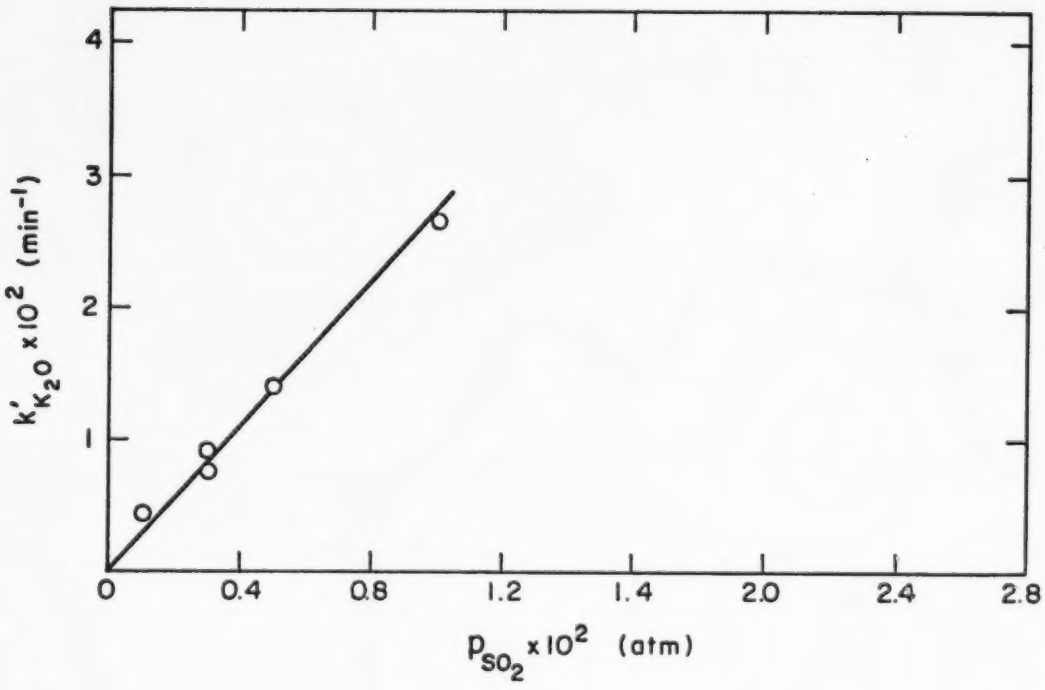


Figure 10. Plot of experimental rate constant for the sulfation of $K_2O$ vs. $p_{SO_2}$.

where the rate is given extensively, $A_r$ is the remaining reactive surface area and $k_{K_2O}$ is the specific rate constant for the sulfation of $K_2O$. If $A_r$ is proportional to the unreacted volume fraction

$$A_r = A_o\left(1-F_{K_2O}\right) \tag{4}$$

then

$$\frac{dF_{K_2O}}{dt} = k_{K_2O}\cdot A_o\cdot p_{SO_2}\cdot\left(1-F_{K_2O}\right) \tag{5}$$

and ,

$$k'_{K_2O} = k_{K_2O}\cdot A_o\cdot p_{SO_2} \tag{6}$$

This variation in reactive area is often encountered with porous internally reacting solids and it can be explained by a suitable population distribution of micrograins of various size in the porous solid. Each micrograin reacts at its surface and consists of a shrinking unreacted core. Smaller grains are consumed early in the reaction and cease to contribute to the total reactive area. Bartlett[4] has computed rate curves for an aggregate of spherical micrograins having Schuhmann size distribution with a core-shell morphology. When the computed fraction conversion for rate control by surface chemical reaction is plotted as $\log_e(1-F)$ vs. dimensionless time, a nearly straight line results.

Values of $k_{K_2O}\cdot A_o$ were computed for different temperatures and plotted against 1/T in Fig. 11. The apparent activation energy from this Arrhenius plot is only 800 cal.mole$^{-1}$, and

$$k_{K_2O} = 3.06 \times 10^{-3}\cdot\exp -\left(\frac{800}{RT}\right)\left(\text{g of solid min}^{-1}\ \text{m}^2\text{atm}^{-1}\right) \tag{7}$$

The following heterogeneous chemical reaction mechanism is suggested

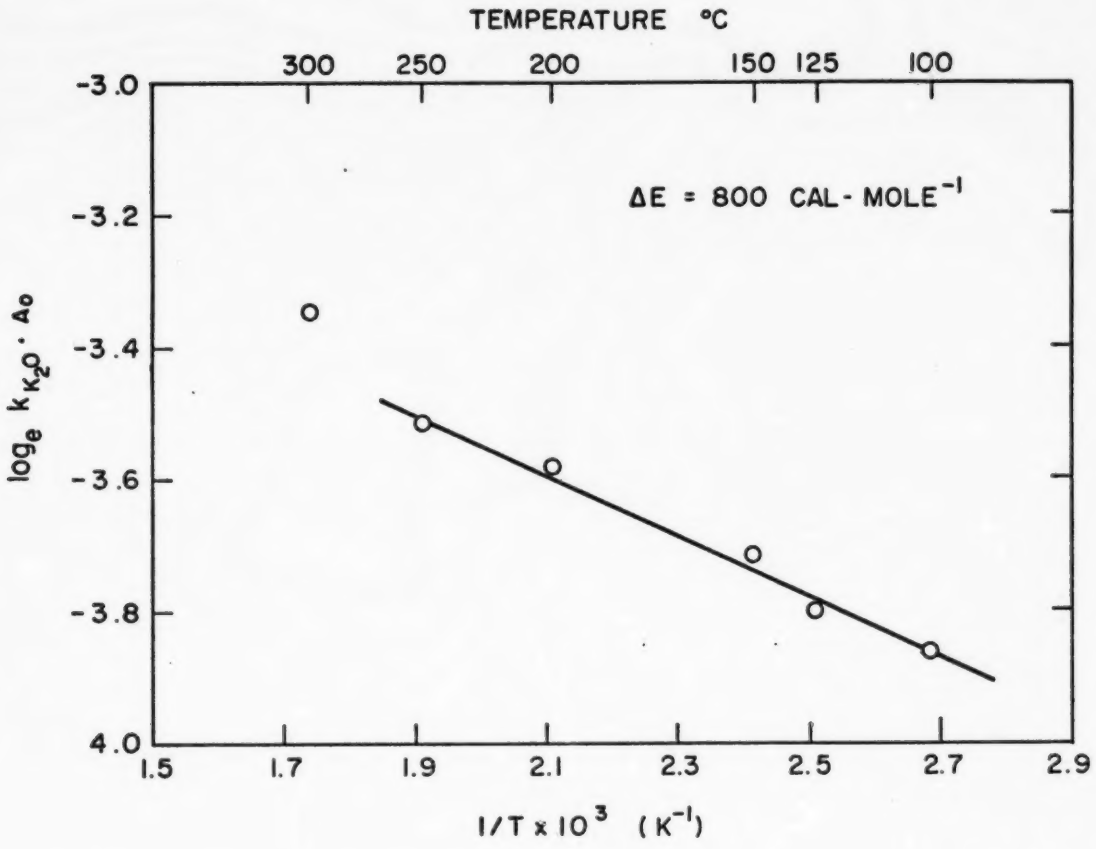


Figure 11. Plot of $\log_e(k_{K_2O}A_o)$ vs. 1/T.

for the sulfation of $K_2O$. The sulfite formation step is assumed to be the rate controlling step, because of the zero order dependency on oxygen.

$$K_2O|_s + SO_2(g) \rightleftharpoons K_2O|_s \cdot SO_2 \qquad \text{equilibrium chemisorption}$$

$$K_2O|_s \cdot SO_2 \longrightarrow K_2SO_3(c) \qquad \text{slow step}$$

$$K_2SO_3(c) + \tfrac{1}{2} O_2(g) \longrightarrow K_2SO_4(c)$$

DISCUSSION OF RATE MECHANISM ABOVE 300°C - SULFATION OF $K_2O$ AND $Al_2O_3$

Above 300°C, potassium sulfate and potassium aluminum sulfates are produced. From our investigations it is not possible to determine whether potassium aluminum sulfate forms in a single step reaction ($K_2SO_4 + \frac{1}{3} Al_2O_3 + SO_2 + \frac{1}{2} O_2 \rightarrow \frac{2}{3} K_3Al(SO_4)_3$) or proceeds through the formation of an amorphous aluminum sulfate intermediate ($\frac{1}{3} Al_2O_3 + SO_2 + \frac{1}{2} O_2 \rightarrow \frac{1}{3} Al_2(SO_4)_3$ ; $\frac{1}{3} Al_2(SO_4)_3 + K_2SO_4 \rightarrow \frac{2}{3} K_3Al(SO_4)_3$.) Chao and Sun[6] report that the sulfation of aluminum oxide is extremely slow even at 600°C, but the presence of alkali metal sulfates catalyzes the sulfation of alumina above 300°C.

It is seen from Fig. 6 that oxygen concentration has an effect on the rate of sulfation in the latter stages at 500°C. The rate controlling step is expected to be relatively simple and irreversible, and probably involves the sulfation of aluminum oxide by reaction with $SO_2$ and $O_2$.

The postulated reactions can be written as follows:

$$K_2O + SO_2 \rightarrow K_2SO_3$$

$$K_2SO_3 + \tfrac{1}{2} O_2 \rightarrow K_2SO_4$$

$$\frac{1}{3}\ Al_2O_3 + SO_2 + \frac{1}{2}\ O_2 \rightarrow \frac{1}{3}\ Al_2(SO_4)_3$$

$$K_2SO_4 + \frac{1}{3}\ Al_2(SO_4)_3 \rightarrow \frac{2}{3}\ K_3Al(SO_4)_3$$

$$\frac{2}{3}\ K_3Al(SO_4)_3 + \frac{2}{3}\ Al(SO_4)_3 \rightarrow 2\ KAl(SO_4)_2$$

$$(K_2O \cdot Al_2O_3 \cdot 4SO_3)$$

Extrapolation of the rate expression for the formation of $K_2SO_4$ to 500°C yields the experimental rate constant $k'_{K_2O}$ at 500°C. The weight increase corresponding to the formation of $K_2SO_4$ can be computed from the rate expression. Subtracting this weight increase from the observed weight increase yields the weight increase contributed by alumina sulfation. This is illustrated in Fig. 12. Again, we can define a term $F_{Al_2O_3}$ as the fraction of alumina that has been sulfated to form $KAl(SO_4)_2$. When $\log_e \left(1-F_{Al_2O_3}\right)$ was plotted against reaction time, straight lines were obtained for the runs above 300°C suggesting a rate mechanism for sulfation of alumina similar to that of potash with the rate being proportional to the unreacted fraction. Figs. 13 and 14 are $\log_e \left(1-F_{Al_2O_3}\right)$ vs. time plots that show the effect of temperature and $SO_2$ pressure, respectively, on the rate of alumina sulfation. The dependence of the rate on $p_{SO_2}$ is first order as shown in Fig. 15. The Arrhenius plot for the sulfation of alumina in hydrogen reduced alunite is shown in Fig. 16. The apparent activation energy is 9600 cal.mole$^{-1}$. The alumina sulfation extensive rate may be expressed as

$$\frac{dF_{Al_2O_3}}{dt} = k'_{Al_2O_3}\left(1-F_{Al_2O_3}\right) \qquad (8)$$

where

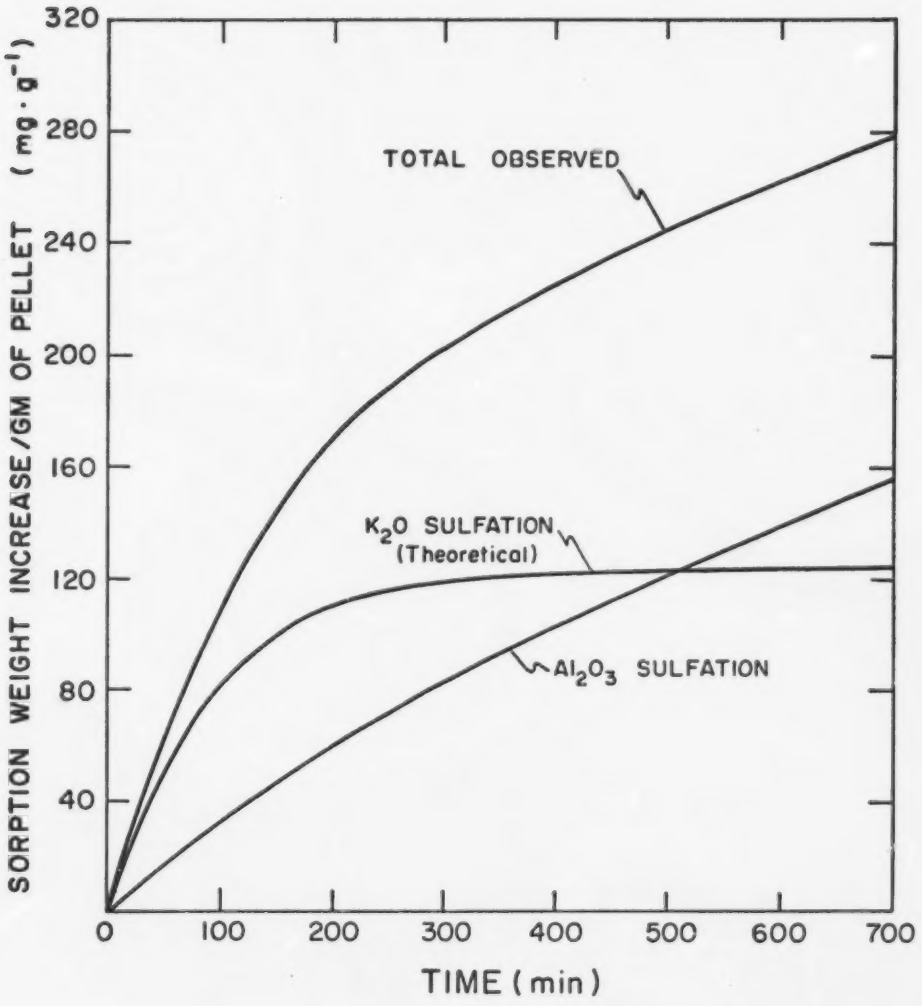


Figure 12. Contribution by sulfation of alumina towards the observed weight gain; with 0.003 atm $SO_2$ and 0.024 atm water vapor at 500°C.

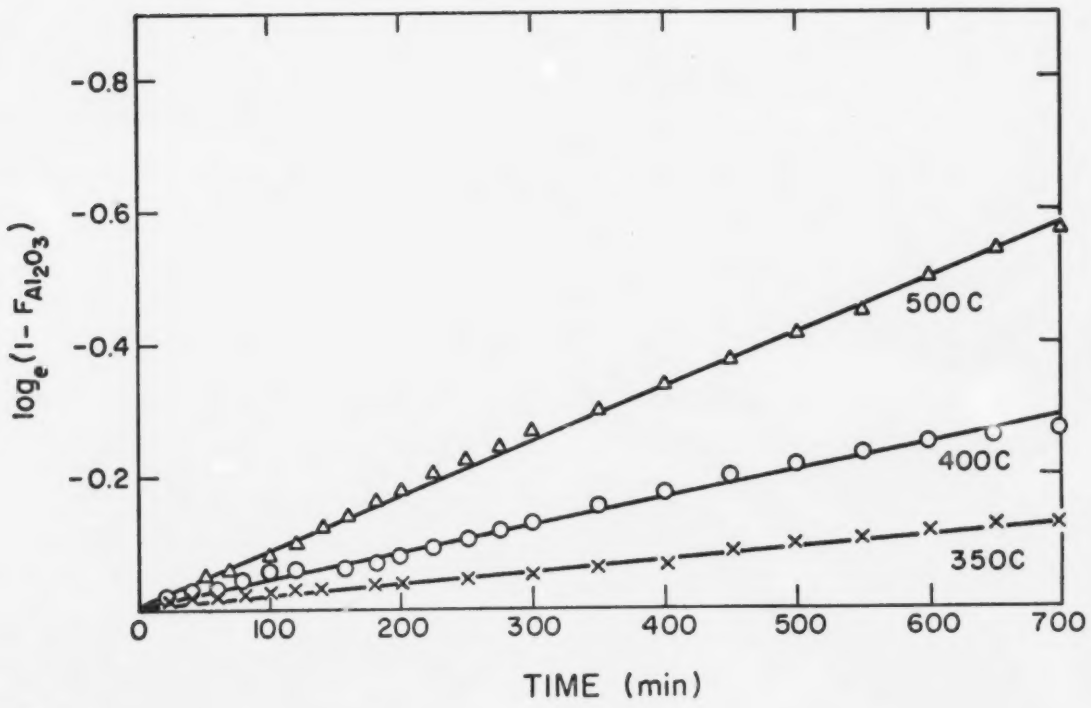


Figure 13. Plot of $\log_e(1-F_{Al_2O_3})$ vs. time; with 0.003 atm $SO_2$ and 0.024 atm water vapor at 300°C, 400°C, and 500°C.

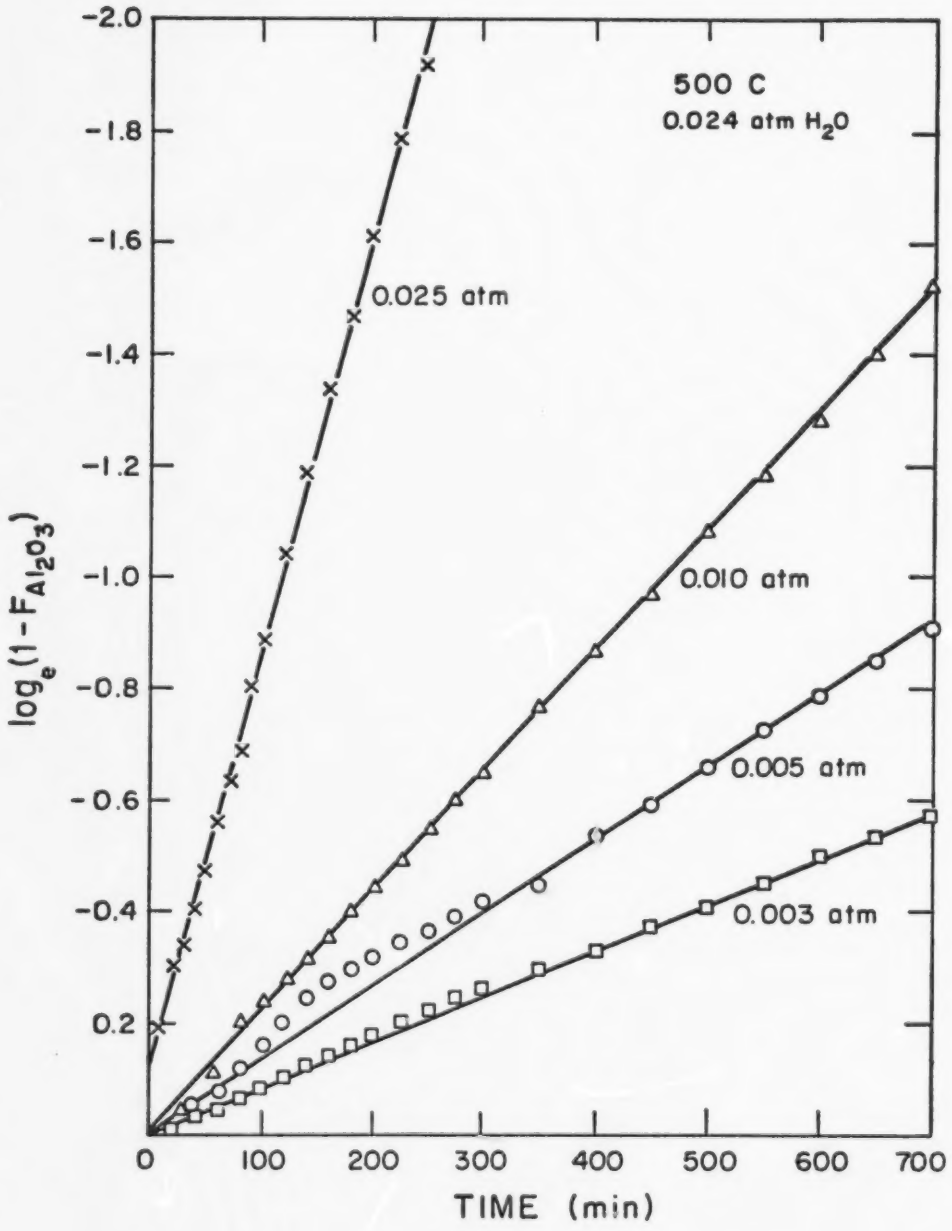


Figure 14. Plot of $\log_e(1-F_{Al_2O_3})$ vs. time; with various concentrations of $SO_2$ and 0.024 atm water vapor at 500°C.

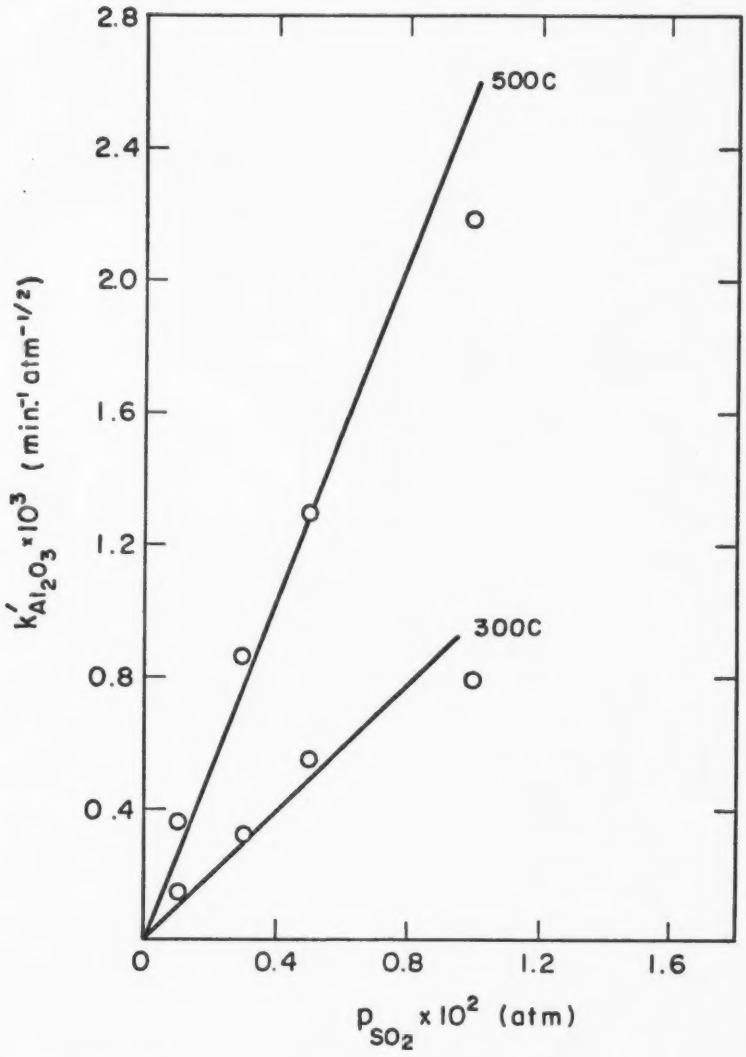


Figure 15. First order dependency of the rate of sulfation of alumina on $p_{SO_2}$.

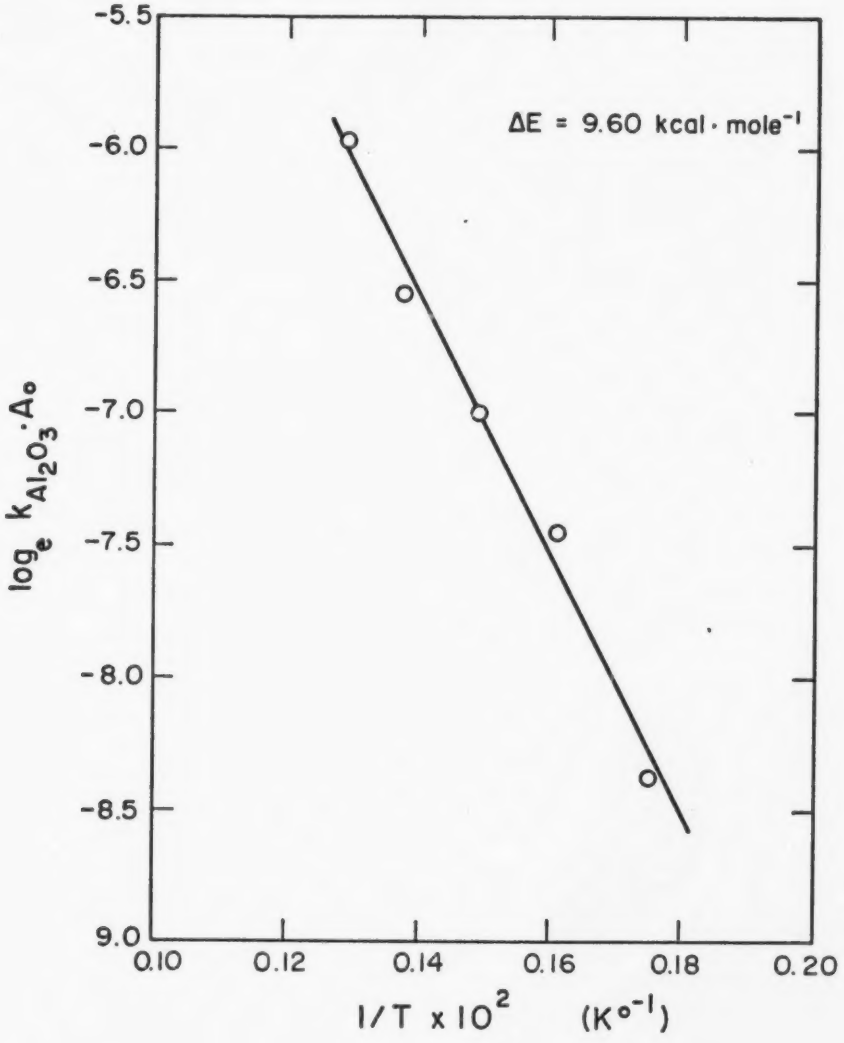


Figure 16. Plot of $\log_e(k_{Al_2O_3}A_o)$ vs. 1/T.

$$k'_{Al_2O_3} = k_{Al_2O_3} \cdot A_o \cdot p_{SO_2} \cdot p_{O_2}^{\frac{1}{2}} \tag{9}$$

and

$$k_{Al_2O_3} = 4.79 \times 10^{-2} \exp\left[-\frac{9600}{RT}\right] \quad (\text{g of solid min}^{-1}\ \text{m}^2\ \text{atm}^{-3/2}) \tag{10}$$

The experimental proportionality constant $k'_{Al_2O_3}$ can be determined by another method. Above 300°C there are essentially two parallel reactions taking place from the beginning, $K_2O$ sulfation being faster than $Al_2O_3$ sulfation. The observed weight gain can be written as

$$w = W_K \cdot F_{K_2O} + W_{Al} \cdot F_{Al_2O_3} \tag{11}$$

where $W_K$ and $W_{Al}$ are the weight gains for stoichiometric sulfation of $K_2O$ and $Al_2O_3$ respectively. At longer reaction times, $F_{K_2O} \rightarrow 1$, and the weight gain becomes

$$w = W_K + W_{Al} \cdot F_{Al_2O_3} \tag{12}$$

Substitution for $F_{Al_2O_3}$, i.e., $F_{Al_2O_3} = 1\text{-}\exp\left(-k'_{Al_2O_3} \cdot t\right)$ yields,

$$w = W_K + W_{Al} \cdot \left(1\text{-}\exp\left(-k'_{Al_2O_3} \cdot t\right)\right) \tag{13}$$

Rearranging this we get

$$\log_e\left(\frac{W_K + W_{Al} - w}{W_{Al}}\right) = -k'_{Al_2O_3} \cdot t \tag{14}$$

So a plot of $\log_e\left[\frac{W_K + W_{Al} - w}{W_{Al}}\right]$ vs. t should be a straight line with a slope of $k'_{Al_2O_3}$ at long reaction times if the assumed expression for $F_{Al_2O_3}$ is correct. A plot of $\log_e\left[\frac{W_K + W_{Al} - w}{W_{Al}}\right]$ vs. t is shown in Fig. 17, and a straight line is obtained at longer reaction times. $k'_{Al_2O_3}$ values obtained by this method are in close agreement with the values determined by the previous method.

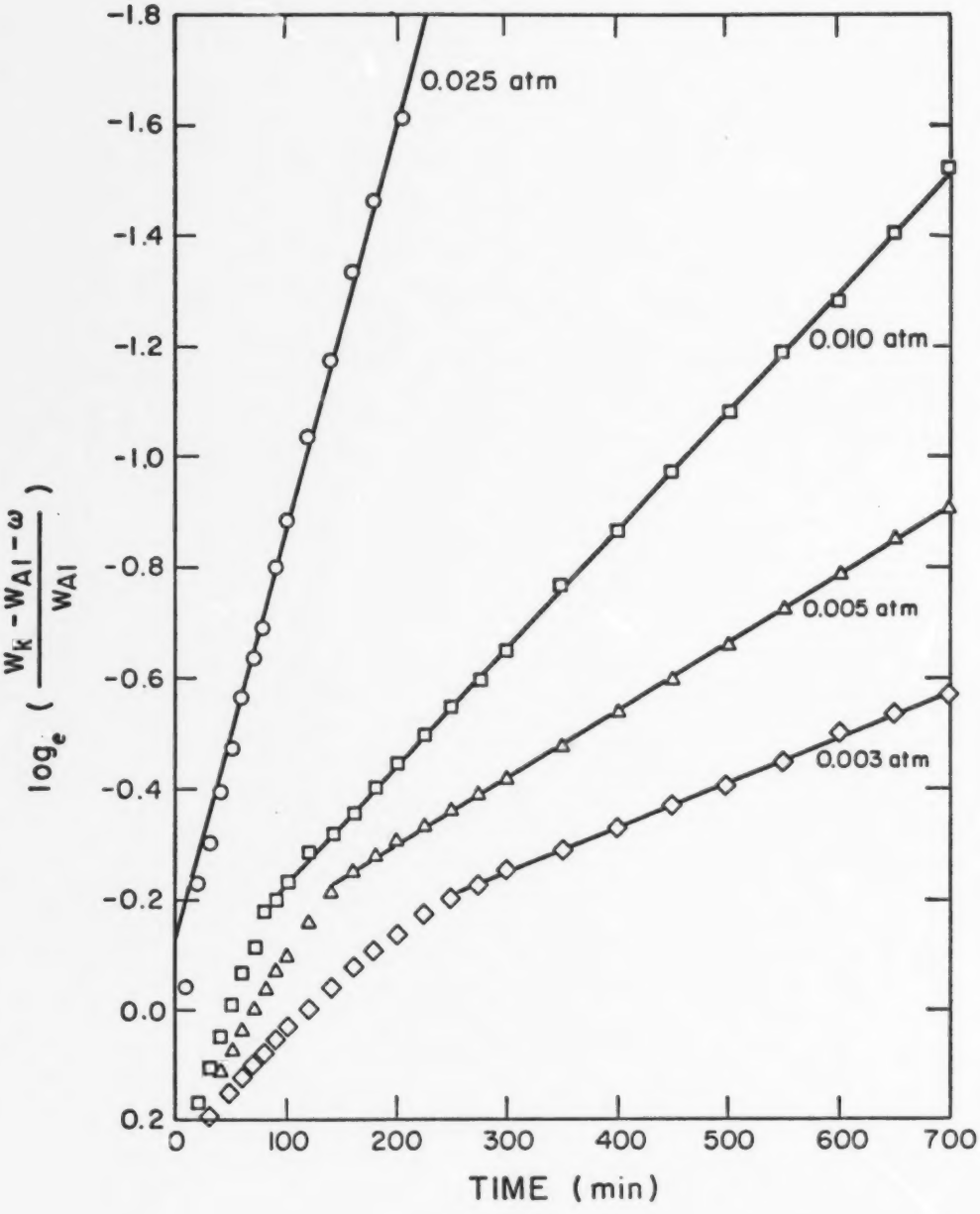


Figure 17. Calculation of $k'_{Al_2O_3}$ by the second method at 500°C.

## COMBINED RATE EQUATION

Extrapolation of $k'_{Al_2O_3}$ from Arrhenius plot (Fig. 16) to lower temperatures shows that for reaction periods used in our study, the weight gain due to alumina sulfation becomes insignificant below 300°C. We have already seen that at high temperatures the rate can be written as the combination of rate expressions for $K_2O$ and $Al_2O_3$ sulfations. The combined rate expression can be written as

$$W = W_K \left[1-\exp(-k_{K_2O} \cdot A_o \cdot p_{SO_2} \cdot t)\right] + W_{Al} \left[1-\exp(-k_{Al_2O_3} \cdot A_o \cdot p_{SO_2} \cdot p_{O_2}^{1/2} \cdot t)\right] \quad (15)$$

At lower temperatures, because of the temperature dependency, $k_{Al_2O_3}$ becomes small, and the second term in equation 15 becomes negligibly small.

## CONCLUSIONS

The rate of sorption at 0.003 atm $SO_2$ and 300°C is $5.6 \times 10^{-4}$ gS per g of solid per min and the rate is only slightly sensitive to temperature. The maximum loading is 0.05 gS per g of solid below 300°C, and above 300°C it is increased to 0.19 gS per g of solid. These values are comparable to those for alkalized alumina developed by U.S. Bureau of Mines.[2]

The kinetic investigations showed that the rate is proportional to the unreacted fraction, to the partial pressure of sulfur dioxide, and only slightly sensitive to temperature. Initial rates ($K_2O$) are independent of oxygen partial pressures and only slightly sensitive to temperature. At low temperatures absence of water vapor causes extensive

pore blocking that decreases the rate. At high temperatures and larger sulfation periods, the sulfation of $Al_2O_3$ becomes important and the rate becomes a function of oxygen partial pressure.

NOMENCLATURE

| | |
|---|---|
| $A_o$ | Original reactive area based on B.E.T. measurement-$m^2 g^{-1}$ of solid. |
| $A_r$ | Remaining reactive area - $m^2 g^{-1}$ of solid. |
| $F_{Al_2O_3}$ | Fraction of alumina that has reacted to form $KAl(SO_4)_2$. |
| $F_{K_2O}$ | Fraction of potassium oxide that has reacted to form $K_2SO_4$. |
| $k_{Al_2O_3}$ | Rate constant for alumina sulfation - g of solid $min^{-1}$ $m^2$ $atm^{-3/2}$. |
| $k_{K_2O}$ | Rate constant for sulfation of potassium oxide - g of solid $min^{-1}$ $m^2$ $atm^{-1}$. |
| $k'_{Al_2O_3}$ | Experimental rate constant for alumina sulfation - $min^{-1}$. |
| $k'_{K_2O}$ | Experimental rate constant for potassium oxide sulfation - $min^{-1}$. |
| $p_{SO_2}$ | Partial pressure of $SO_2$ - atm. |
| $p_{O_2}$ | Partial pressure of $O_2$ - atm. |
| R | Gas constant - 1.98 cal. $^oK^{-1}$ $mole^{-1}$. |
| t | Reaction time - min. |
| T | Reaction temperature $^oK$. |
| w | Observed weight gain - g·g of $solid^{-1}$. |
| $W_{Al}$ | Maximum weight gain corresponding to the stoichiometric sulfation of alumina - g·g of $solid^{-1}$. |
| $W_K$ | Maximum weight gain corresponding to the stoichiometric sulfation of potassium oxide - g·g of $solid^{-1}$. |

REFERENCES


(1) Bienstock , D. and J.H. Field. Bench Scale Investigation on Removing Sulfur Dioxide from Flue Gases . J. Air. Poll. Cont. Ass.. 10:121, (1960).

(2) Bienenstock, D., J.J. Field and J.H. Myers. Process Development in Removing Sulfur Dioxide from Hot Flue Gases (in Four Parts). 3. Pilot Plant Study of the Alkalized Alumina System for $SO_2$ Removal . Bu. Mines Rept. of Inv.. 7021, 1967, 57 p.

(3) Fink, W.L., K.R. Van Horn and H.A. Pazour. Thermal Decomposition of Alunite . Ind. Eng. Chem. 23:1248, (1931).

(4) Town, J.W., P.E. Sanker and H.J. Kelly. Alkalized Alumina Attritioning Rates and $SO_2$ Sorption Rates . Bu. Mines Rept. of Inv., 7275 (1969), p. 22-28.

(5) Bartlett, R.W. Conversion and Extraction Efficiencies for Ground Particles in Heterogeneous Process Reactors . Met. Trans. 2:2999 (1971).

(6) Chao, T. and S.C. Sun. Study on Sulfation of Alumina With Gaseous Sulfur Trioxide . Trans. Soc. Mining Engrs.. 238:425, Dec. 1967.

(7) U.S. May Get Aluminum from Alunite. Eng. Min. Jour., 173:9, June 1972.

# KINETICS OF SULFATION OF ATLANTIC OCEAN MANGANESE NODULES

## INTRODUCTION

Both dry and wet (slurry) manganese oxides have been shown to be effective sorbents for $SO_2$.[1-3] Manganese oxides can be regenerated from $MnSO_4$ by thermal decomposition,[2] by reduction and by wet chemical methods. The Bureau of Mines process involves NaOH which produces $Na_2SO_4$ that is subsequently electrolyzed.[1] The DAP-Mn process has been developed by Mitsubishi Heavy Industries[4] in Japan and installed on a semi-commercial basis at the Yokkaichi power station. This process involves dry sorption followed by ammonia scrubbing in an air blown tower to regenerate the manganese oxide and produce salable ammonium sulfate.

The use of manganese sea nodules for sorption of $SO_2$ from stack gases was first proposed by Zimmerley.[5] The ocean floors carry huge reserves of these nodules[6] and both, a throw-away process and cyclic regeneration sorption can be considered. A final economic evaluation depends on development of mining methods and costs.

Manganese sea nodules are a complex mixture of several metal oxides, including the oxides of manganese and iron and sometimes calcium carbonate. Minor, but occasionally economically interesting, amounts of copper, nickel and cobalt oxides are usually present. At least three manganese oxide minerals have been recognized in the nodules, but they are usually found as intimately intergrown sub-micron sized crystallites exhibiting weak x-ray diffraction patterns with considerable line broadening.

The present investigation is concerned with the kinetics of sorption of $SO_2$ by relatively dry marine manganese nodules. Hence, a gas-solid process, rather than a gas-slurry process, for the absorption of $SO_2$ is involved.

The results reported were obtained exclusively with manganese nodules from the Blake Plateau in the Atlantic Ocean, off the coast of South Carolina, at a depth of about 3000 ft. A few experiments were made using Pacific Ocean manganese nodules obtained at greater depths. Although the results were generally similar, the sorption capacity was lower.

## PROPERTIES OF BLAKE PLATEAU ATLANTIC MANGANESE NODULES

In order to obtain a uniform representative sample, several nodules were crushed and sieved. The apparent density found by volume displacement of heavy mineral oil for 14-20 mesh samples ranges from 1.9 to 2.9 g $cm^{-3}$. The true density was 5.43 g $cm^{-3}$ as determined by helium displacement in a press transducer. A chemical analysis of the elements of interest is shown in Table 1.

Table 1. WEIGHT PERCENTAGE OF THE MAJOR COMPONENTS IN BLAKE PLATEAU NODULES AS EQUIVALENT OXIDES AND AS METALS

| | | | |
|---|---|---|---|
| $Mn_2O_3$ | 31.20 | Mn | 21.76 |
| $CaCO_3$ | 20.10 | Ca | 8.04 |
| $Fe_2O_3$ | 19.41 | Fe | 13.59 |
| $Co_3O_4$ | 0.78 | Co | 0.57 |
| CuO | 0.23 | Cu | 0.18 |
| NiO | 0.82 | Ni | 0.64 |

Loss on Heating 15 minutes at 600°C was 22.0 %.

Weak powder X-ray diffraction patterns were obtained using a lithium drifted germanium radiation detector. Calcite ($CaCO_3$) and goethite (FeOOH) were detected in unheated nodules and goethite has previously been identified in manganese nodules.[7] No manganese phase could be detected without previously heating the specimen, but the initial manganese composition is believed to be close to $MnO_2$. When heated above 300°C Goethite is converted to hematite, $Fe_2O_3$. Magnetite, $Fe_3O_4$, was not observed in any X-ray diffraction patterns. Calcite appeared at all temperatures to 600°C, inclusive. X-ray diffraction patterns for manganese oxides appeared after heating the nodules in air or oxygen. After heating between 400°C and 600°C, the primary manganese oxides were $\gamma$-$Mn_2O_3$ or $Mn_3O_4$ (haussmanite), which have very similar diffraction patterns, and birnessite, $\delta$-$MnO_2$. Heating in air or oxygen to only 300°C yielded a higher proportion of $\delta$-$MnO_2$.

These results are in agreement with the reported[8] equilibrium transformation of $MnO_2$ to $Mn_2O_3$ between 307°C and 600°C and the transformation of $Mn_3O_4$ to $Mn_2O_3$ below 600°C.

Water is lost on heating manganese nodules. To ensure a uniformly dehydrated starting material, all samples were preheated for 15 minutes at 600°C before starting the reaction at the desired temperature. Thermal decomposition of calcite becomes significant above 600°C and interferes with a gravimetric determination of the sulfation rate. The X-ray diffraction patterns exhibited by the unreacted manganese oxides in partially sulfated specimens show little variation between 300°C and 600°C.

The specific surface area, measured by the B.E.T. method, did not change with temperatures to 600°C. Between 200°C and 600°C the specific surface area was about 170 $m^2/g$. A pore distribution analysis was

performed using an Orr surface analyzer. Assuming cylindrical pores, 50% of the pore volume is occupied by pores below 65 Å, with a maximum distribution of pores between 25 and 40 Å.

## EXPERIMENTAL PROCEDURE

The kinetics of sulfation of Atlantic manganese nodules were studied using sulfur dioxide pressures from 0.0025 to 0.03 atm., which are typical of power plant flue gases and the more dilute streams in non-ferrous smelters, in the temperature range 300°C to 600°C. Thermodynamic data indicate that for these temperatures, the sulfation reactions of all metallic oxides were irreversible.

The sulfation rates were determined by thermogravimetric analysis of crushed and sized nodules, usually -14+20 mesh, suspended in an open crucible within a vertical tube furnace. Weight changes occurring during isothermal experiments were monitored using either a recording electrobalance or a McBain (quartz helix) balance.

A closed loop system was used for experiments in dry gases. Because a very large gas reservoir and circulating pump were used, the change in partial pressure of sulfur dioxide during a sulfation experiment was less than 0.0005 atm. Before each experiment the gas loop was evacuated and filled with a specified gas composition using a gas burette. The sample was brought to temperature while isolated from the gas loop using a reaction chamber bypass. Each experiment began when the reactive gas was switched from the bypass to the reaction chamber.

A flow-through gas system was used for experiments that included water vapor. The gas composition was controlled by flowmeters and water vapor was introduced by a temperature controlled gas bubbler.

Sulfur dioxide was injected downstream from the gas bubbler at the entrance to the reaction chamber.

The kinetic experiments were augmented by electron beam microprobe analyses, scanning electron microscopy, X-ray diffraction, surface area measurements and pore distribution analysis.

## RESULTS AND DISCUSSION

The rate of sulfation of Atlantic manganese nodules decreases as the reaction proceeds. The rates are first order in $SO_2$ pressure. The effect of oxygen pressure is complex but less pronounced than that of sulfur dioxide.

### Absorption Time Curves and Sorption Capacity

From 400°C to 600°C the weight gain absorption curves are similar and approximately the same sorption capacity, or maximum weight gain, is reached regardless of the gas composition or temperature. Typical thermogravimetric sorption curves at 500°C are shown in Figure 1. The final weight increases vary from 525 to 565 mg/gram of nodule. The nodule weight is the initial sample weight before dehydration at 600°C.

Attainment of these high sorption capacities requires complete sulfation of the major constituent metal oxides in the nodules: manganese, iron and calcium. A stoichiometric calculation of complete sulfation based on the chemical analysis of Table 1 requires a weight increase of 543 mg/g. This calculation includes weight losses caused by dehydration and removal of $CO_2$ from calcite. Below 600°C, $SO_2$ reacts directly with $CaCO_3$ without prior calcination in an exchange process.

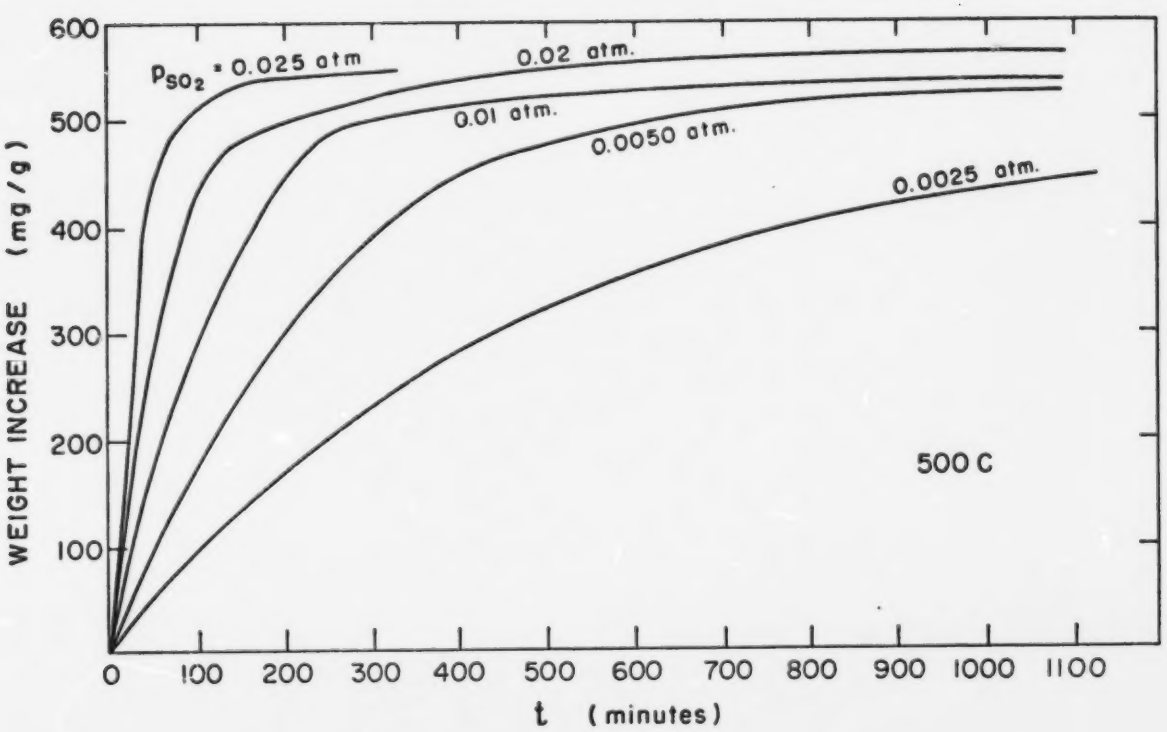


Figure 1. Sulfur absorption curve of manganese nodules at 500°C.

X-ray diffraction patterns from nodules sulfated between 400°C and 600°C show that the sulfates of manganese, iron and calcium are present while calcite is diminished for partial reaction and eliminated when the sorption capacity is reached. This evidence supports occurrence of the following major sulfation reactions, which go to completion as the sorption capacity is reached:

$$MnO_2 + SO_2 \rightarrow MnSO_4$$

$$Mn_2O_3 + 2SO_2 + \frac{1}{2}O_2 \rightarrow 2MnSO_4$$

$$\frac{1}{3}Fe_2O_3 + SO_2 + \frac{1}{2}O_2 \rightarrow 1/3\ Fe_2(SO_4)_3$$

$$CaCO_3 + SO_2 + \frac{1}{2}O_2 \rightarrow CaSO_4 + CO_2(g)$$

The oxidation of sulfur to the sulfate form may occur with the sulfur fixing reaction as shown in the previous expressions or it may occur as a prior step by the catalytic oxidation of $SO_2$ to $SO_3$ on the nodule surfaces. There was no evidence for bulk sulfite formation either by X-ray diffraction or wet chemical analyses for partially or completely reacted specimens. The wet chemical method had a sensitivity of 0.15% sulfur as sulfite.

The following minor sulfation reactions may also occur, but there is no x-ray diffraction or other direct evidence:

$$CuO + SO_2 + \frac{1}{2}O_2 \rightarrow CuSO_4$$

$$NiO + SO_2 + \frac{1}{2}O_2 \rightarrow NiSO_4$$

$$Co_3O_4 + 3SO_2 + O_2 \rightarrow 3CoSO_4$$

These minor metals may be present as substituting cations in the major metal oxide.

Experiments with one batch of Pacific nodules indicate that their sulfur-sorption capacity above 400°C is reduced to approximately 37% of that of the Atlantic nodules. There are major compositional differences between these two nodules. Table 2 gives a chemical analysis of the major constituents. The $SO_2$ sorption capacity of the Pacific nodules examined was only 60% of the stoichiometric sulfation of manganese, which is the dominant constituent.

Table 2. WEIGHT PERCENTAGE OF THE MAJOR COMPONENTS IN PACIFIC NODULES AS EQUIVALENT OXIDES AND METALS

| | | | |
|---|---|---|---|
| $Mn_2O_3$ | 54.50 | Mn | 37.93 |
| $CaCO_3$ | 3.65 | Ca | 1.46 |
| $Fe_2O_3$ | 0.94 | Fe | 0.66 |
| $Co_3O_4$ | 0.15 | Co | 0.11 |
| CuO | 1.69 | Cu | 1.35 |
| NiO | 1.40 | Ni | 1.10 |

Loss on heating 15 minutes at 600°C was 19.5 wt.%.

Atlantic nodules are not completely sulfated at 300°C, as shown by the thermogravimetric sorption curves in Figure 2. X-ray diffraction patterns of nodules sulfated at this temperature show no sulfates other than $MnSO_4$ and no significant loss of calcite. The diffraction patterns and sorption curves show that manganese is readily sulfated and probably reacts completely within a few hours. Continued sulfation of the other major oxides, particularly iron oxide, appears to occur at a very slow rate that is also dependent on the $SO_2$ pressure. A final

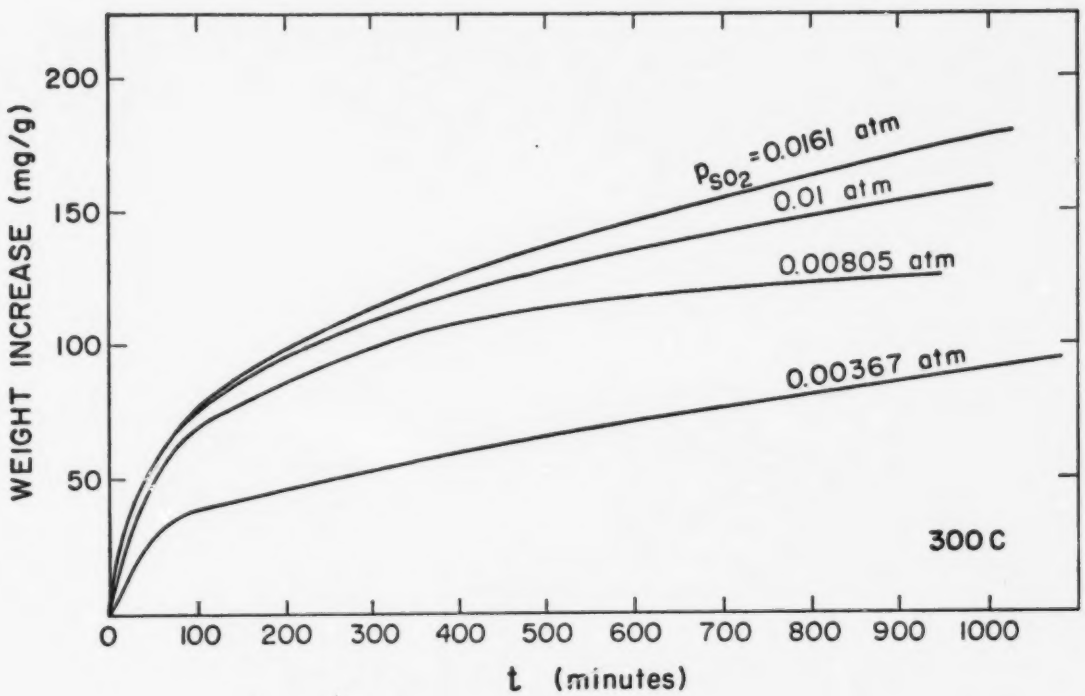


Figure 2. Sulfur absorption curve of manganese nodules at 300°C.

weight increase or sorption capacity is not reached because the other oxides are sulfated very slowly. Surface area measurements were carried out on specimens that had been sulfated at 300°C and 400°C for periods that yielded 18% conversion. The residual internal surface area of the specimen sulfated at 300°C was only 60% of that sulfated at 400°C. This decrease in area suggests that pore blocking also slows the extensive reaction at the lower temperature.

Extraction of Copper, Nickel and Cobalt

Completely sulfated Atlantic nodules were leached in boiling water for 2 1/2 hours. Although acid was not added, partial hydrolysis of soluble iron probably occurred and the acidity increased to pH ~ 2. A large portion of the manganese, but little of the iron, dissolved. Extractions of the economic metals were high: 99% of the copper, 82% of the nickel and 97% of the cobalt. The extractions were calculated from semi-quantitative emission spectrographic analysis of the nodules before and after leaching. These extraction tests indicate that the minor metals in the nodules are substantially sulfated at 400°C and higher temperatures and that these economically important metals could be recovered from manganese nodules sulfated by a stack gas. This may be particularly important for coastal power plants when economic nodule mining methods are developed. Similar extractions on Pacific nodules yielded 45% of the nickel and 90% of the copper after sulfation.

Experimental Rate Equations

At 400°C to 600°C the rate of sulfation of manganese nodules is conveniently expressed in terms of the fractional conversion, F, of all of the major metal oxides to sulfates. In the -14+20 mesh size fraction reaction occurs uniformly throughout the particle. The rate is first order in $SO_2$ pressure and also proportional to the amount of unreacted

material in the nodule, which fractionally expressed is 1-F. Hence,

$$\frac{dF}{dt} = k_o (1-F) p_{SO_2} \qquad (1)$$

where $k_o$ is an experimental rate constant. Integration yields,

$$F = 1 - \exp(-k_o p_{SO_2} t) \qquad (2)$$

When expressed logarithmically, this relation provides a convenient test of the experimental data, which should fit a straight line:

$$d \log (1-F) = \frac{-k_o p_{SO_2}}{2.303} dt \qquad (3)$$

Structural models for porous reacting solids with a distribution of micrograin sizes that obey surface chemical kinetics and follow the logarithmic law for extensive rates of sulfation are discussed in Chapter VI.

Plots of log (1-F) versus time at 400°C, 500°C and 600°C are shown in Figures 3, 4 and 5, respectively. The negative slopes from Figures 3-5, (-d log (1-F)/dt), are plotted against the sulfur dioxide partial pressure in Figure 6 and yield reasonable straight lines. The experimental rate constants at each temperature are determined from the appropriate slope. The first order dependence on $SO_2$ is confirmed by this plot.

Finally, the experimental activation energy can be obtained from an Arrhenius plot of the rate constants determined from Figure 6, which is shown in Figure 7. As the rate constant at 300°C is not known and in order to evaluate accurately the activation energy, the initial rates at time t=0 are plotted versus the sulfur dioxide partial pressures in Figure 8. These slopes are used in the same way as for Figure 6 to

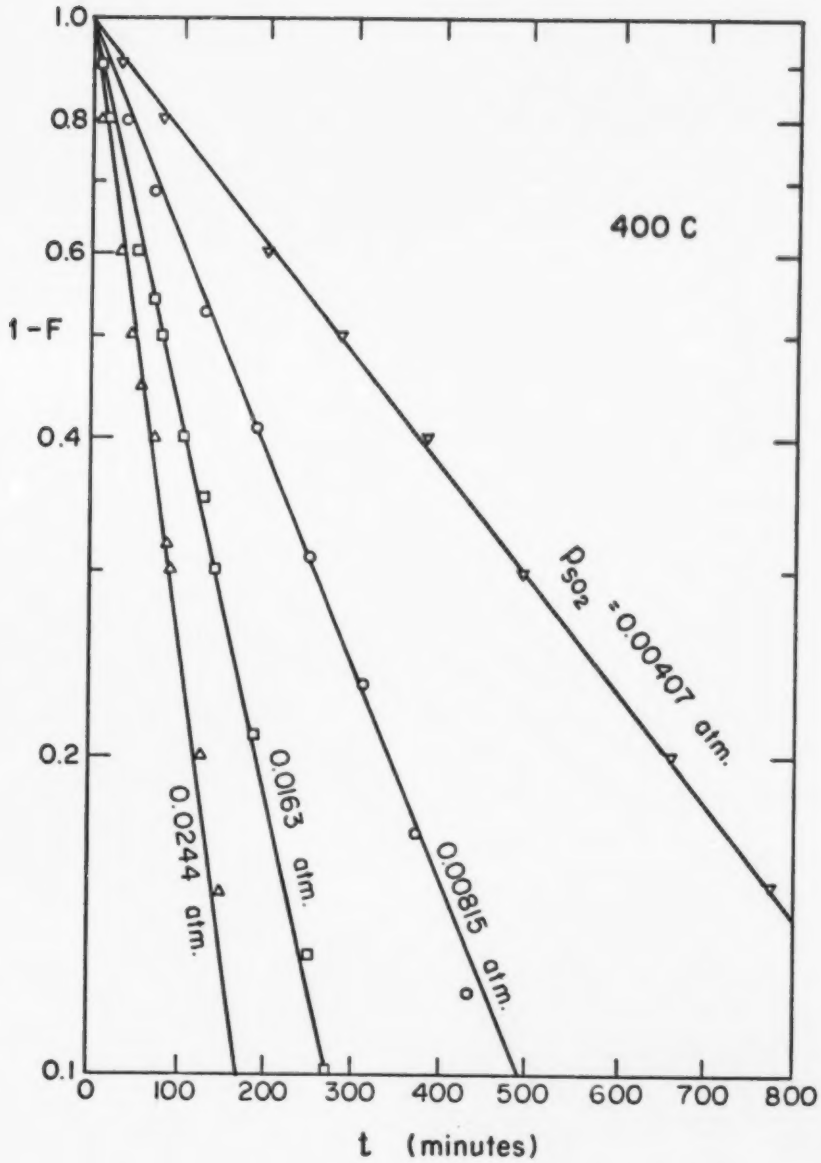


Figure 3. Plot of log(I-F) versus time at 400°C for different $SO_2$ partial pressures.

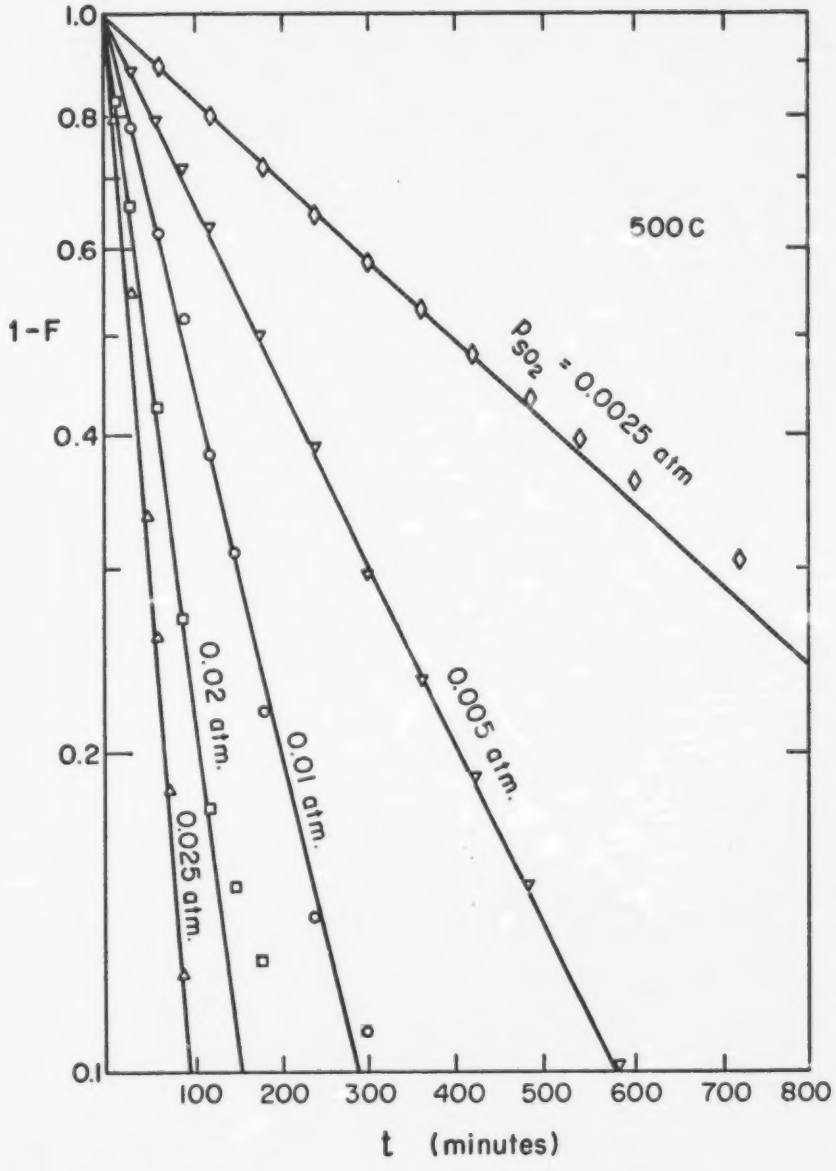


Figure 4. Plot of log(I-F) versus time at 500°C for different $SO_2$ partial pressures.

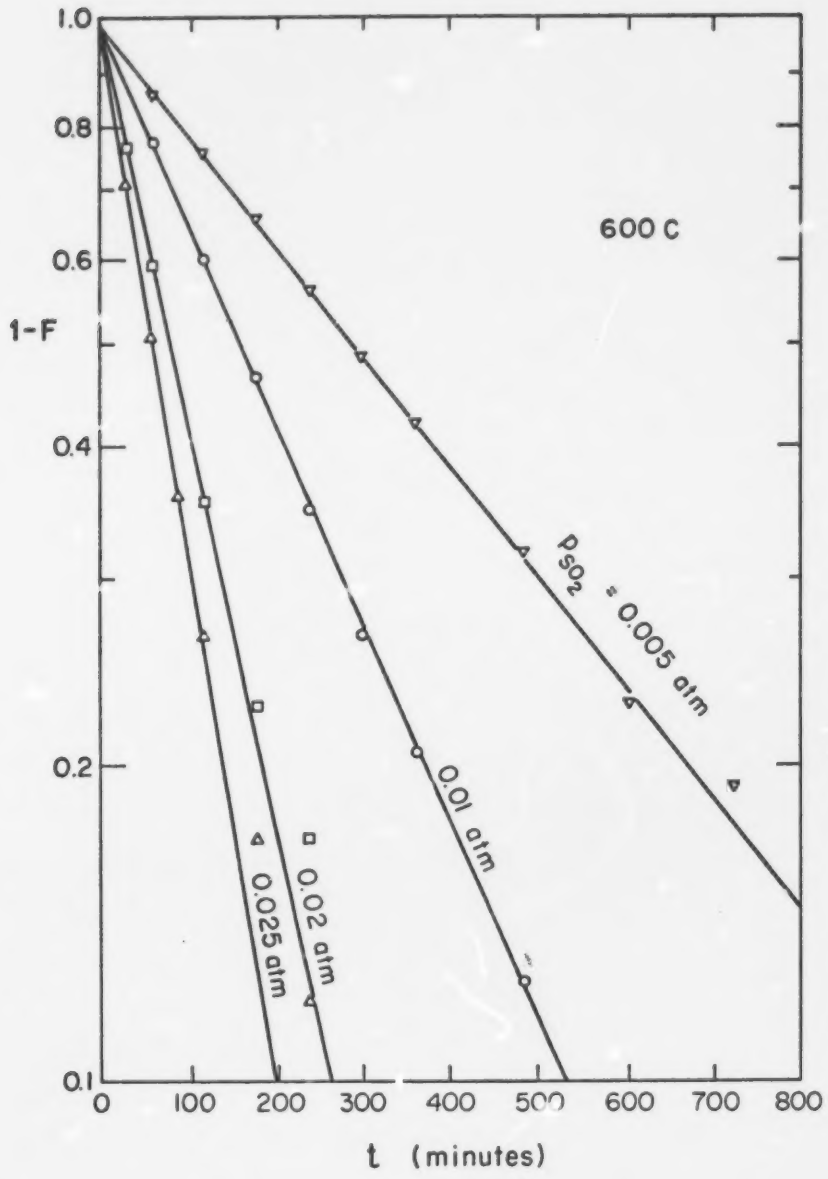


Figure 5. Plot of log(I-F) versus time at 600°C for different $SO_2$ partial pressures.

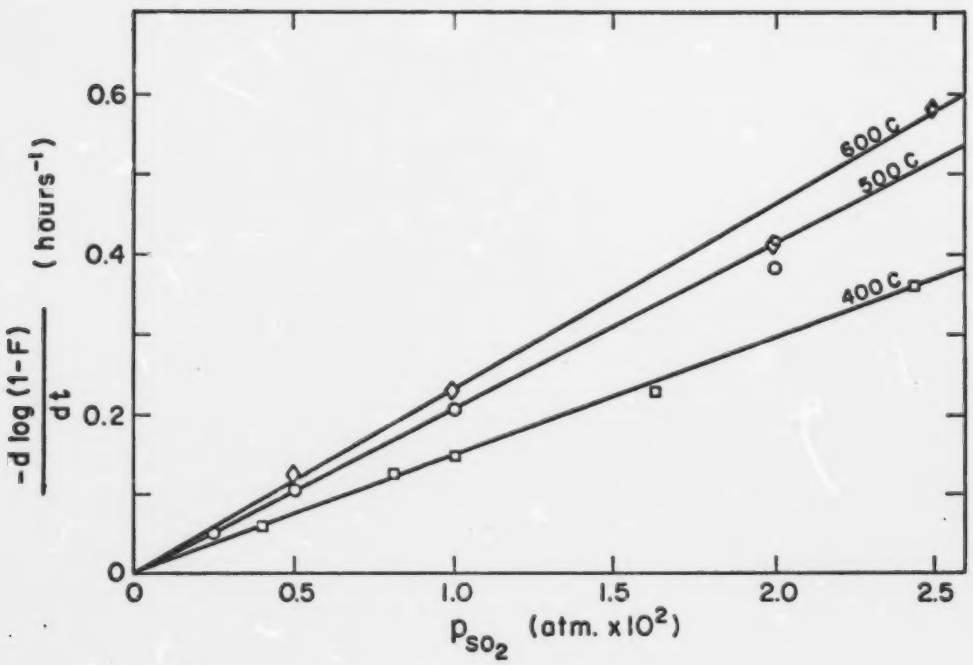


Figure 6. Determination of the experimental rate constant at 400 500 and 600°C.

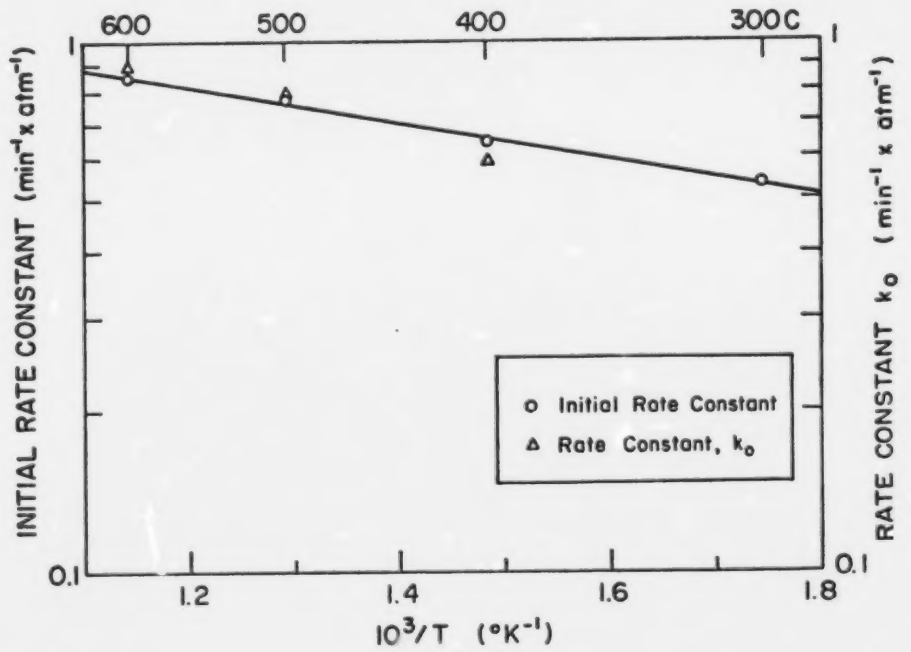


Figure 7. Arrhenius plot of the experimental rate constant and initial rate constant.

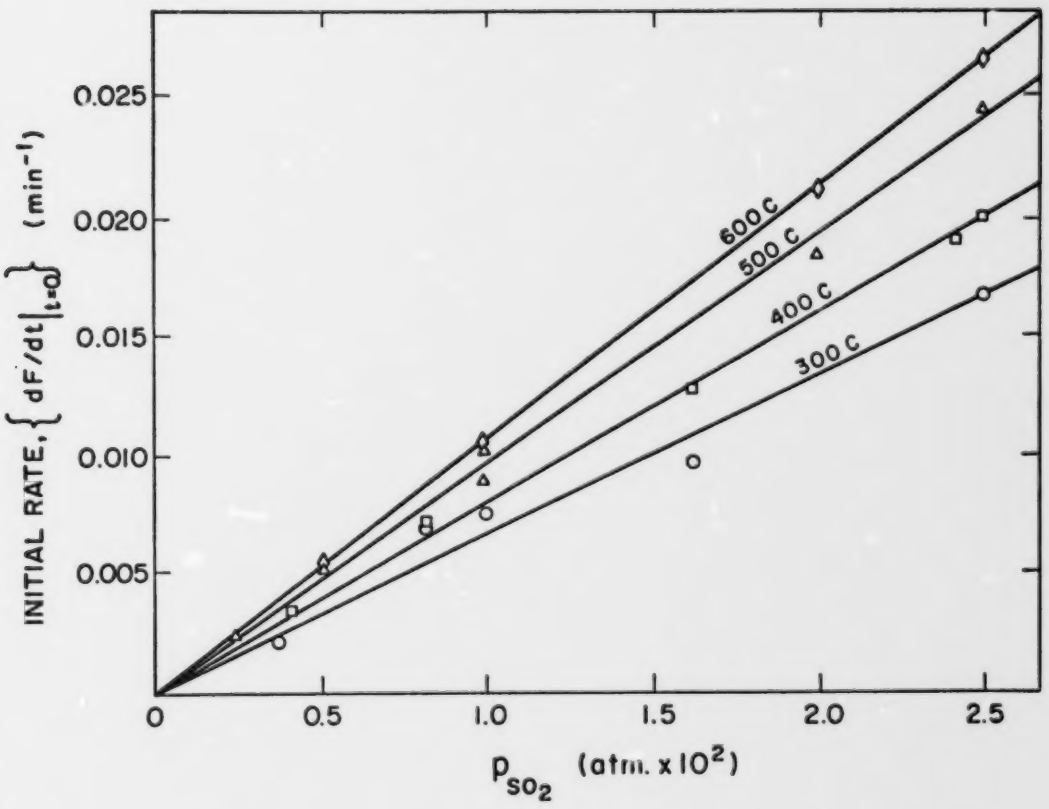


Figure 8. Initial rate as a function of sulfur dioxide partial pressure at 300, 400, 500 and 600°C.

evaluate the activation energy. The small activation energy obtained is 1.6 kcal $mole^{-1}$.

Particle Size and Pore Diffusion

Pore diffusion within the crushed nodule particles is not a significant rate controlling factor over the particle sizes studied. This has been demonstrated by three separate criteria. After various reaction times particles were sectioned and subjected to electron beam microprobe traverses. Although there were microscopic variations in sulfur and other components, the macroscopic concentration distribution of sulfur from the outside to the interior of each particle was uniform. Changing the particle size had little effect on the rate. A plot of fractional reaction versus time at 500°C for three different particle sizes that were sulfated under identical gas compositions at 500°C is shown in Figure 9. The rates were independent of the particle sizes. The effectiveness factor calculated using an average effective diffusion coefficient[9] with an average pore radius of 25 Å tends to unity for the two smaller size particles, but not for -14+20 mesh. Major pore arteries are larger than 25 Å and the true effectiveness factor is probably larger than the one based on the average pore size.

Water Vapor

Experiments were conducted in 0.025 atm of water vapor at 300°C, 400°C and 500°C. The sorption curves at 400°C and 500°C were similar to the sorption curves in dry gas mixtures. The kinetics followed equation (3), except that there was a slight retardation in the rate constant. The results are summarized in Table 3, where the rate constant in the presence of water vapor, $k_w$, is expressed as a fraction of

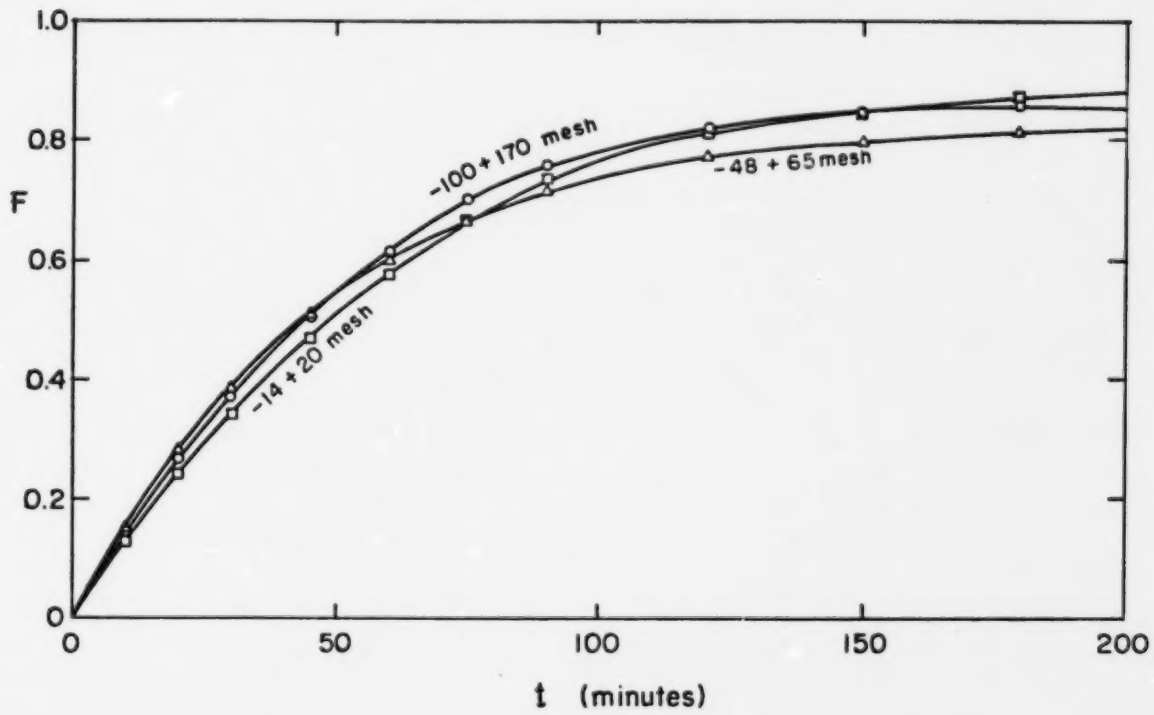


Figure 9. Fractional reaction versus time at 500°C for different particle sizes.

the rate constant, $k_o$, for a dry gas mixture.

Table 3. SUMMARY OF EXPERIMENTS IN THE PRESENCE OF WATER VAPOR USING -14+20 MESH NODULES

| T(°C) | $p_{SO_2}$ (atm x $10^2$) | $p_{H_2O}$ (atm) | $k_w$ ($atm^{-1}$ $hours^{-1}$) | $k_w/k_o$ |
|---|---|---|---|---|
| 400 | 1.0 | 0.025 | 13.8 | 0.92 |
| 400 | 2.5 | 0.025 | 13.1 | 0.875 |
| 500 | 1.0 | 0.025 | 13.8 | 0.67 |
| 500 | 2.5 | 0.025 | 17 | 0.83 |
| 500 | 7.0 | 0.025 | 16.8 | 0.82 |

Scanning electron micrographs of surfaces obtained by fracturing manganese nodules show little structural change as a result of sulfation in dry gases, but the presence of water vapor causes a smoother surface. Scanning electron micrographs of specimens completely sulfated at 400°C in dry and wet gas mixtures, respectively, are shown in Figure 10.

Small amounts of water vapor accelerate the kinetics at 300°C, particularly after sulfation of manganese oxide has been substantially completed. Water vapor may prevent pore blocking or catalyze the oxidation of $SO_2$ to $SO_3$, which would react with the remaining oxides to form sulfates.

Oxygen

The oxygen concentration in the gas did not affect the early stage of sulfation, but there was a rate reduction after about 40% conversion

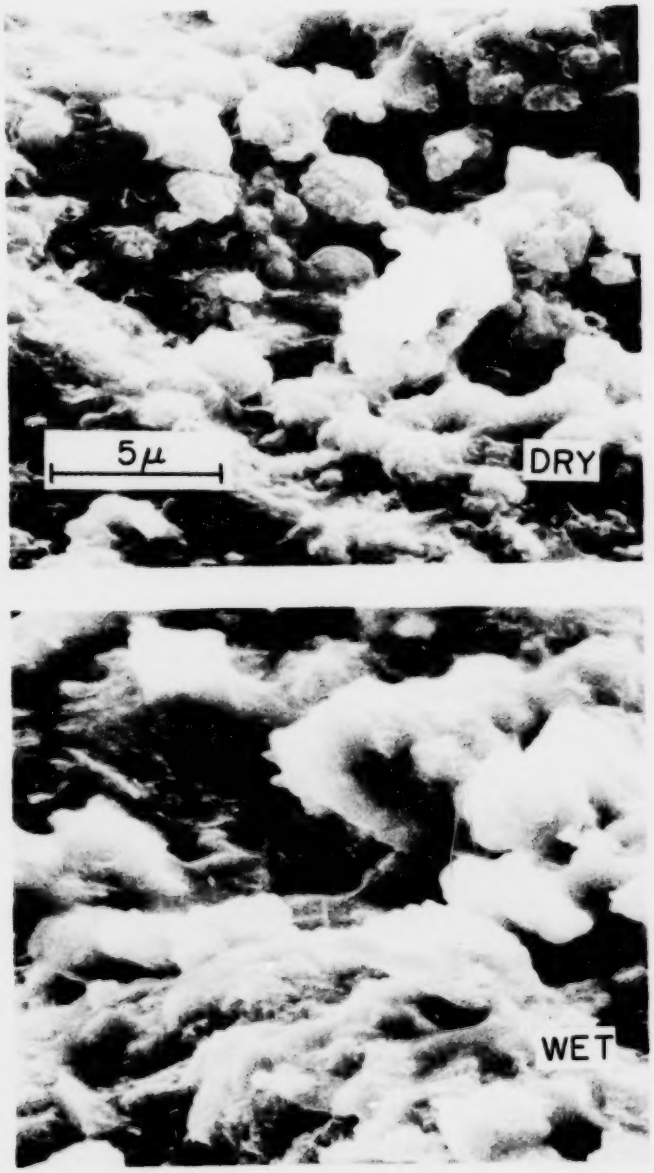


Reproduced from best available copy.

Figure 10. Scanning electron micrographs of specimens completely sulfated in dry and wet gas mixtures.

at 400°C. This effect is hardly noticeable on the weight gain curves since the sorption capacity is unaffected, but there is a pronounced discontinuity at (1-F) ≈ 0.6 when log (1-F) is plotted against time, see Figure 11. In about 1 atm of oxygen the rate is unperturbed and the log (1-F) plot is a straight line to at least 90% conversion. The break at about 40% conversion may correspond with the complete sulfation of $Mn_2O_3$ which does contribute about 42% of the total stoichiometric weight increase for previously dehydrated nodules. Furthermore, it can be seen from the experiments at 300°C that manganese is selectively sulfated early at that temperature. With the exception of $MnO_2$, all of the metal oxides require additional oxygen to form their respective sulfates, and an oxygen rate dependency is not unexpected. Because of the release of $CO_2$ the exchange sulfation of calcite does not yield much net weight gain. Most of the stoichiometric weight increase not assigned to sulfation of manganese oxides is contributed by the sulfation of $Fe_2O_3$ which accounts for 43% of the total weight gain for previously dehydrated nodules. Hence, to a first approximation the sulfation can be divided into that of manganese oxides and iron oxide with the remaining oxides making a small contribution. The sulfation of the two major oxides may occur as parallel processes with both proportional to their unreacted fractions, $1-F_{Mn}$ and $1-F_{Fe}$, respectively, but not necessarily at the same rate, particularly at low oxygen pressures. Early sulfation of the alkali metal oxide has been observed for sulfation of activated sodium aluminate and the reduced mineral, alunite. In both cases alumina is sulfated in the later stages at sufficiently high temperatures.

However, for Blake Plateau manganese nodules the X-ray diffraction results show that all of the sulfates are present for 400°C conversions

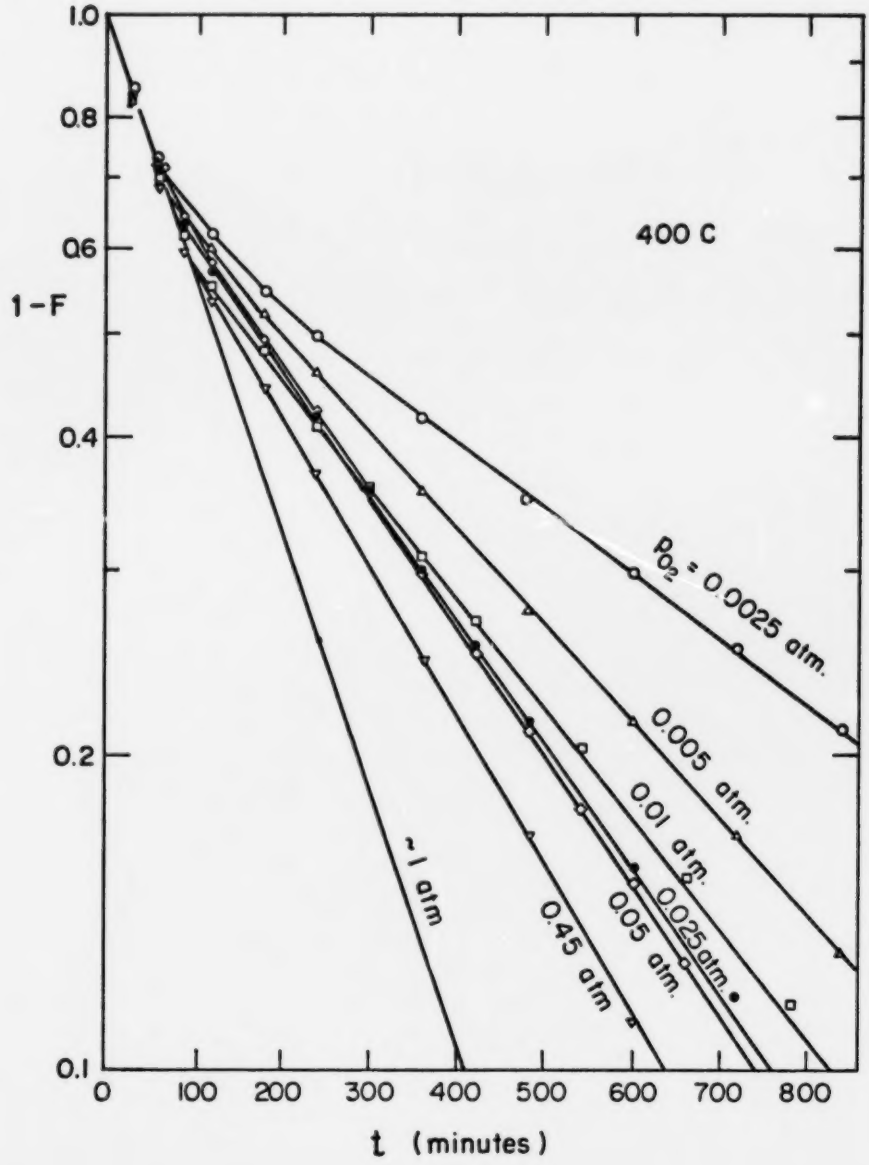


Figure 11. Oxygen effect on the reaction rate at 400°C.

of both 30% and 50% with about the same relative increase in diffraction peaks for each sulfate between 30% and 50% conversions. Furthermore, there is X-ray diffraction evidence for $Mn_2O_3$ at conversions beyond the approximately 40% break point in the absorption curves, which is strong evidence that sulfation of manganese oxides is not complete at the break point. Hence, a satisfactory explanation of the rate perturbation after about 40% reaction has not been resolved. In a 5% oxygen atmosphere, which is fairly typical of stack gases, the rate is reduced to about 1/3 of its former value after 40% conversion. However, because of the logarithmic decay in extensive rate the effect on the absorption curve is not pronounced.

## CONCLUSION

Manganese nodules from the Blake Plateau are a very effective absorbent for $SO_2$ in stack gases. The absorption capacity was in excess of 0.5 g per g of nodule regardless of the $SO_2$ pressure when sulfated between 400 and 600°C. All of the major metal components, manganese, iron and calcium are completely sulfated. Extractions of copper, nickel and cobalt obtained by leaching the fully sulfated nodules in boiling water were nearly complete.

The kinetic study shows that the sulfation rate is proportional to the partial pressure of sulfur dioxide and to the unreacted solid. The rate increases slightly with temperature. The rate is not significantly affected by pore diffusion at nodule crushed particle sizes to 14 mesh. Water vapor had little effect in the range from 400 to 600°C, but at 400°C the rate depended on oxygen pressure in a curious way after about 40% of the material had reacted.

The sulfation kinetics of manganese at 300°C is similar to the kinetics observed at higher temperatures, but $Fe_2O_3$ and $CaCO_3$ are sulfated much more slowly and complete reaction was not reached in our experiments. Small amounts of water vapor accelerate the sulfation of hematite and calcite at 300°C.

NOMENCLATURE

$F$ = Fractional Conversion of the Major Metal Oxides (Manganese, Iron, Calcium).

$k_o$ = Experimental Rate Constant For Dry Gases ($min^{-1}$ $atm^{-1}$).

$k_w$ = Experimental Rate Constant in the Presence of Water Vapor ($hours^{-1}$ $atm^{-1}$)

$p_{H_2O}$ = Partial Pressure of Water (atm).

$p_{SO_2}$ = Partial Pressure of Sulfur Dioxide (atm).

$t$ = Time (minutes).

$T$ = Temperature ($^oK$).

REFERENCES

(1) Bienstock, D., J.H. Field, and J.G. Myers. Process Development in Removing $SO_2$ from Hot Flue Gases, pt. I. U.S. Bur. Mines Report of Invest. 5735. 1961.

(2) Ingraham, T.R., and P. Marier. Kinetics of the Formation of $MnSO_4$ from $MnO_2$, $Mn_2O_3$ and $Mn_3O_4$ and its decomposition to $Mn_2O_3$ or $Mn_3O_4$. Trans. Met. Soc. 242:2039-43. 1968.

(3) Kun Li, R.R. Rothfus, and A.H. Adey. Effect of Macroscopic Properties of Mn Oxides on Absorption of $SO_2$. Environ. Sci. Tech. 2:619, 1968.

(4) T. Uno, et al. Scale-Up of a $SO_2$ Control Process. In: Sulfur and $SO_2$ Development. Amer. Inst. Chem. Engrs.. New York, 1971. P. 73-77.

(5) Zimmerley, S.R. Manganese Minerals for Desulfurizing Gases. US Pat. 3,330,096. Kennecott Corp. July 11, 1967.

(6) Mero, J.L. The Mineral Resources of the Sea. New York, American Elsevier Pub. Co., 1965. 321 p.

(7) Buser, W. The Nature of the Iron and Manganese Compounds in Manganese Nodules. (Internat. Oceanog. Cong. Preprints, Am. Assoc. Advan. Sci., Washington, D.C. 1959.) p. 962-3.

(8) Bienstock, D., L.W. Brunn, E.M. Murphy, and H.E. Benson. Sulfur Dioxide - Its Chemistry and Removal From Industrial Waste Gases. Bur. of Mines Information Circular No. 7836. 1957. 96 p.

(9) Satterfield, C.N., and T.K. Sherwood. The Role of Diffusion in Catalysis. Addison-Wesley Publ. Co. 1963. 118 p.

# KINETICS OF SULFATION OF RED MUD SOLID WASTE FROM THE BAYER ALUMINA PROCESS

## INTRODUCTION

Red mud is the solid waste remaining after extraction of alumina from bauxite by the Bayer process. It is produced at the rate of about one pound of red mud per pound of alumina,[1] or approximately 6,000,000 tons per year in the U.S. and adjacent Carribean countries and constitutes a major disposal problem.

Dry red mud is a porous intimate mixture of several amorphous metal oxides, and at least some of these react with $SO_2$ at elevated temperatures to form sulfites and sulfates:

$$MO + SO_2 \longrightarrow MSO_3$$

$$MO + SO_2 + \frac{1}{2} O_2 \rightarrow MSO_4$$

Hence, red mud is a potential dry absorbent for $SO_2$ in gaseous effluents. The sorbent can be regenerated by contacting the loaded red mud with $H_2$ or natural gas to produce a concentrated stream of $H_2S$, which then may be converted to elemental sulfur or sulfuric acid by conventional processes.

In the present study, the kinetics of sulfation of dry mud have been investigated over the temperature range from 300 to 600°C using $SO_2$ pressures from 0.002 to 0.035 atm. These are the temperature and sulfur dioxide pressure ranges for power plant stack gases and the more dilute streams in non-ferrous smelters.

## PROPERTIES AND PREPARATION OF THE RED MUD SORBENT

The composition and properties of alumina-plant red mud are dependent on the ore from which the mud is derived and also on the process used for extraction of alumina. Jamaican red mud solids contain twice as much iron oxides as Surinam red mud, and about three times less sodium oxide.[2] The dry red mud studied was of the Jamaican type and its chemical composition is given in Table 1.*

Table 1. CHEMICAL COMPOSITION OF THE DRY RED MUD USED IN THIS STUDY

| Material | Wt.% | Material | Wt.% |
|---|---|---|---|
| Loss on heating[a] | 11 | CaO | 8 |
| $SiO_2$ | 5 | $Na_2O$ | 3 |
| $Al_2O_3$ | 12 | MnO | 1 |
| $Fe_2O_3$ | 50 | $SO_4$ | 0.5 |
| $TiO_2$ | 6 | $CO_2$ | 4 |
| $P_2O_5$ | 1 | | |

[a]primarily chemically combined water removed on heating to 700°C

The B.E.T. surface area of the red mud was dependent on the temperature at which it was preheated. At 500°C, the surface area was 35 to 45 $m^2g^{-1}$ while at 700°C, the specific surface decreased to 14 to 18 $m^2g^{-1}$. All samples were heated at 700°C to provide a constant surface area before reaction at all temperatures. This is also a convenient temperature for

*Obtained from Reynolds Metals Co., Sherwin Plant, Gregory, Texas.

removal of sulfur as $H_2S$ and regeneration of the sorbent. The true density was estimated, using an Orr analyzer, and found to be 3.96 g $cm^{-3}$. The apparent density measured by volume displacement of heavy mineral oil was 2.55 g $cm^{-3}$, which yields a void fraction of 0.355.

## EXPERIMENTAL

Both sulfating and sulfiting kinetics involve a weight increase and reaction rates can be determined by monitoring weight gain at fixed gas composition and temperature.

Thermogravimetric data were obtained using a continuously recording electro-balance. The gas train consisted of a reaction chamber heated by a proportionally controlled electric resistance tube furnace, an 18 liter gas reservoir and circulating loop, gas pump, burette and manometer. The gas circulated through the reactor at about 30 cc/min. This large circulating reservoir provided a nearly constant concentration of sulfur dioxide in the system throughout each experiment. Runs were conducted at a total pressure of 0.1 atm. to diminish convective oscillation of the balance.

Each experiment began with the loading of a preweighed specimen and evacuation of the system. After heating the specimen, oxygen and eventually nitrogen were admitted to a pressure of about 0.1 atm. After the temperature stabilized, an aliquot of $SO_2$ corresponding to the desired partial pressure was injected from the gas burette and circulated through a reaction chamber bypass. When the gas was well mixed, the reaction chamber was opened and the thermogravimetric experiment began.

Sulfation experiments were also conducted in a fixed bed reactor through which a gas stream containing $SO_2$ was passed. Sulfation rates

were determined from the change in $SO_2$ partial pressure monitored with a continuous recording infrared analyzer. This apparatus included a recirculation gas loop with the reaction chamber. A known flow of $SO_2$, $O_2$ and $N_2$ was injected continuously into the loop and after mixing with the recycled gas passed through the bed consisting of dry red mud particles of uniform size. A minor fraction of the gas leaving the bed was removed, continually analyzed and vented while the major part of the gas was recycled by a pump. The high recycle ratio provides a small change in $SO_2$ concentration across the bed and the gas kinetics for the recycle reactor approach those of an ideal backmix reactor. The recycle fixed bed reactor is illustrated in Figure 1. The molar reaction rate, dQ/dt, is

$$dQ/dt = \frac{\dot{v}}{RT}\left(p_{SO_{2in}} - p_{SO_{2out}}\right)$$

where $\dot{v}$ is the volumetric flow rate of gas into and out of the recycle system, R is the gas constant, T is absolute temperature and $p_{SO_2}$ is the pressure of $SO_2$ in consistent units. Electron beam microprobe analyses of the distribution of sodium, potassium, calcium, iron, aluminum, titanium, silicon, manganese and sulfur were made for reacted and unreacted specimens. Wet chemical analyses were used to determine the average concentrations of these constituents before and after reaction, and the amounts of sulfite and sulfate. X-ray powder diffraction analyses were useless because the solids were completely amorphous, both before and after reaction. Surface area measurements were made on reacted, unreacted and partially reacted samples.

## DISCUSSION OF RESULTS

The experimental results obtained with the thermogravimetric

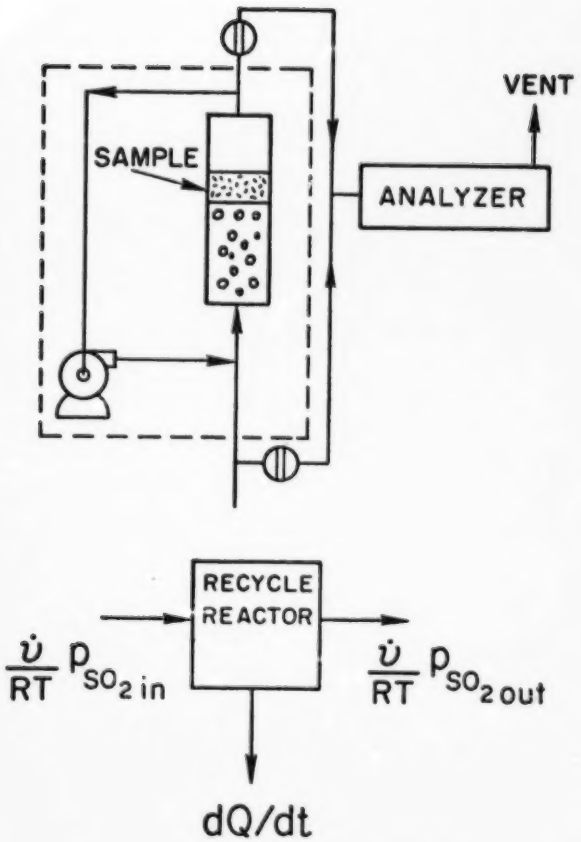


Figure 1. Recycle reactor.

apparatus were very similar to the results obtained with the recycle fixed bed reactor. Although most of the experiments were conducted with 014+20 mesh particles, decreasing the particle sizes did not alter the experimental absorption curves. Wet chemical analyses showed that less than 10% of the absorbent surfaces in the sulfite form with the remainder present as sulfate.

Typical sulfur absorption curves at 300°C are shown in Figure 2. The results are expressed as the weight of sulfur absorbed per gram of dry red mud. However, the term "dry red mud" includes the water that is present prior to heating. The sorption kinetics are fast at this temperature, but the ultimate sorption capacity, 12 mg of sulfur per gram of dry red mud, is low. Changes in the $SO_2$ concentration and oxygen pressure in the reacting gas did not raise or lower the sorption capacity at 300°C. The sorption capacity at this temperature is equivalent to the complete sulfation of the sodium and potassium oxides contained in the particular red mud samples used in the experiments and the sulfation of these oxides is thermodynamically more favored than sulfation of any of the other oxides present in the specimen material.

Sulfation curves at 400 and 500°C are shown in Figures 3 and 4, respectively. The initial absorption kinetics out to a sorption capacity of about 12 mg of sulfur per gram of red mud are quantitatively similar to the kinetics observed at 300°C. However, sulfation continues and the sorption capacity increases. The interesting aspect of these sulfation curves compared with those of many other dry porous solids being sulfated is that the apparent sorption capacity increases with the concentration of sulfur dioxide. It is quite possible that the ultimate sorption capacity is never reached in the finite time experiments. At a given $SO_2$

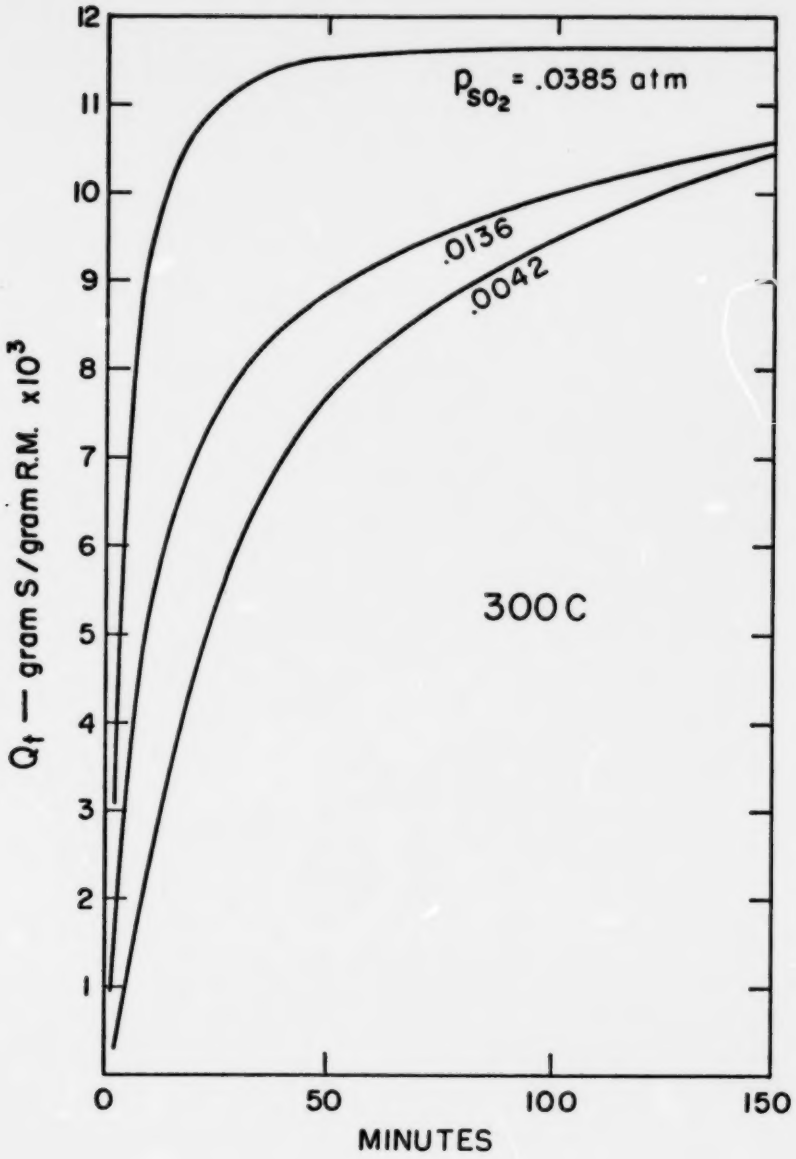


Figure 2. Sulfur absorption curve of dry red mud at 300°C.

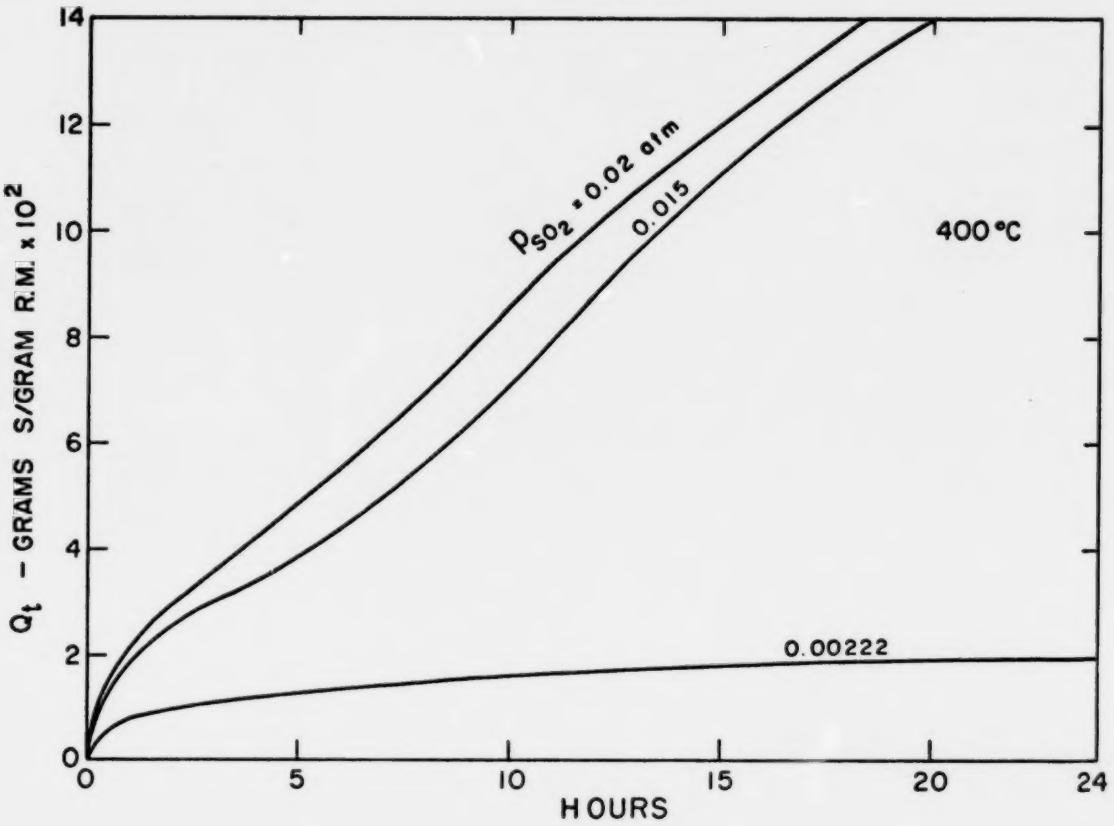


Figure 3. Sulfur absorption curve of dry red mud at 400°C.

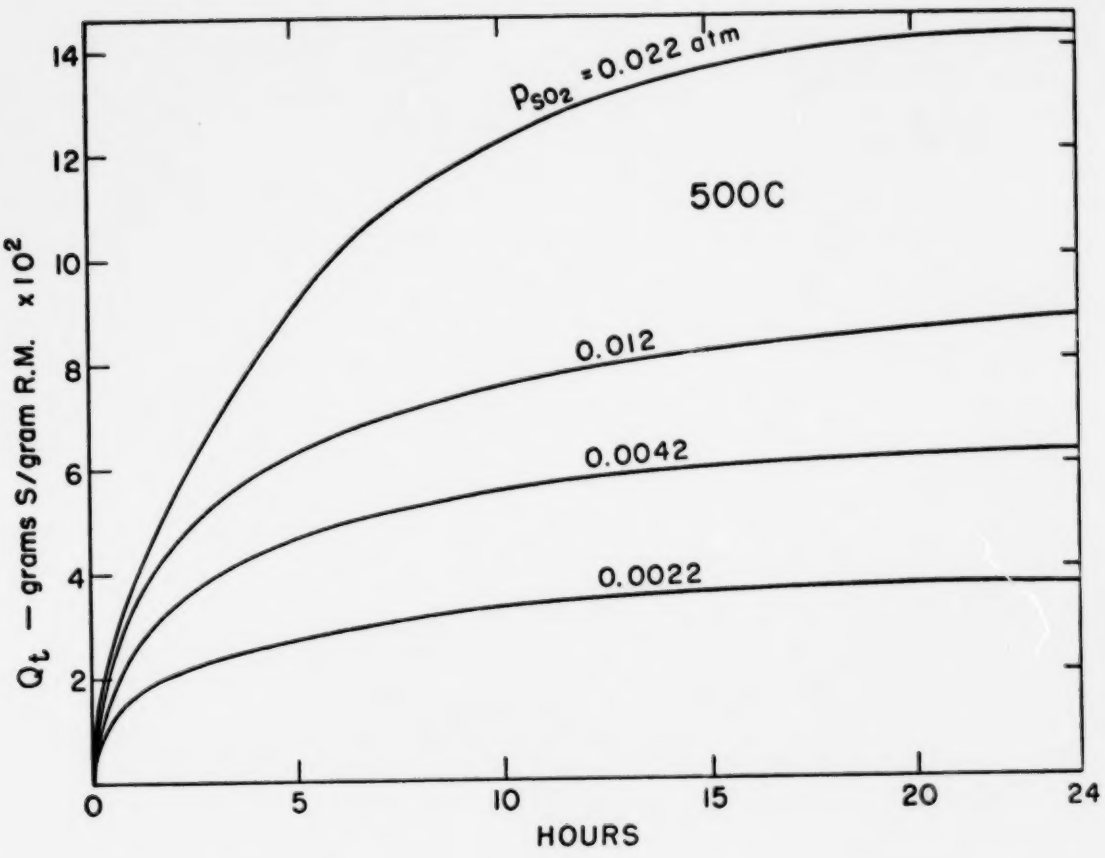


Figure 4. Sulfur absorption curve of dry red mud at 500°C.

concentration the sorption capacity of red mud can be increased by resting the sample in an atmosphere free of $SO_2$ and then re-exposing the sample to $SO_2$.

Sorption capacities in porous reacting solids are usually limited by complete stoichiometric reaction of one or more of the reactive components. The reaction with sodium and potassium oxides at 300°C apparently follows this pattern. The kinetics at sulfur dioxide concentrations above about 2% at 400°C show an inflection in the rate curve that is not observed at 500°C. However, the 24 hour sorption capacity is similar to the sorption capacity at 500°C. Below about 1.5% $SO_2$ concentrations at 400°C the sorption capacities are not much higher than the 300°C sorption capacity. This illustrates the very complex kinetics involved with the mixture of several oxides constituting dry red mud that preclude a detailed kinetic analysis.

Sorption capacities were arbitrarily defined as the sulfur absorbed in 24 hours. The changes in sorption capacity with $SO_2$ concentration are shown for several temperatures in Figure 5. At 500°C the sorption capacity experimentally observed appears to be proportional to $p_{SO_2}^{1/2}$. At 400 and 500°C sulfation of CaO is known to occur. The high sorption capacity suggests that aluminum is also being sulfated, see Figure 5. However, either or both $Al_2O_3$ and $Fe_2O_3$ may be partially sulfated at the higher temperatures and higher $SO_2$ concentrations, since both are thermodynamically possible.

Electron beam microprobe analysis was used to obtain structural evidence for the amorphous sulfation reaction products. Although the sulfur distribution was macroscopically uniform throughout partially or fully sulfated particles, there were localized areas of higher concentration. X-ray fluorescence images were photographed and compared for

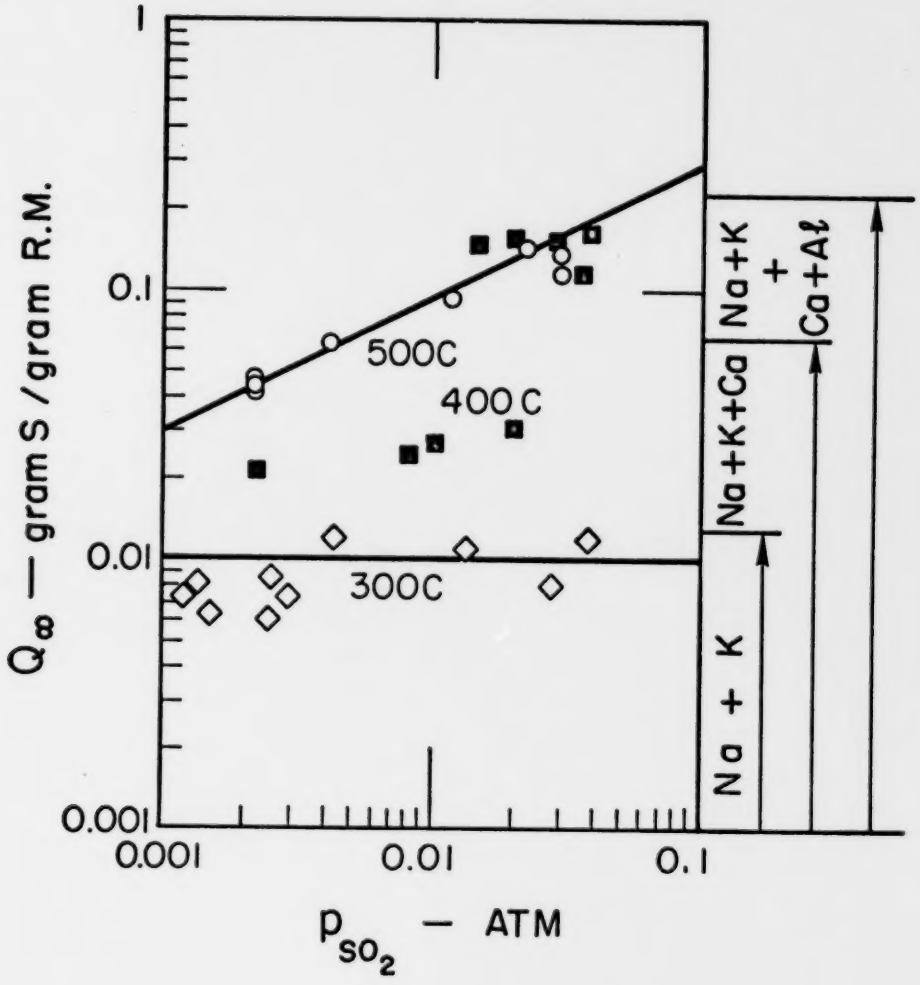


Figure 5. Sorption capacity after 24 hours for 300, 400 and 500°C.

sulfur and each of the constituent metals for several samples and at different locations within each sample. The metal oxides other than CaO and an occasional small grain of Aluminum oxide (probably undigested bauxite) were uniformly distributed at least to a scale of 2 microns. Lime does not derive from the bauxite but is introduced to remove $CO_2$ in the Bayer process circuit and is converted to $CaCO_3$. Consequently, discrete hydrated calcium oxide or calcium carbonate grains of a few microns diameter become suspended in the red mud. As these grains react with sulfur dioxide a calcium sulfate reaction product surrounds the unreacted core. This core/shell reaction morphology is illustrated in Figure 6, which shows the fluorescent X-ray images for calcium and sulfur from a partially reacted calcia grain. This particular grain was hollow, an unusual phenomenon, and the sulfate shell has formed on both the inside and outside surfaces. Extensive microprobe investigations of reacted specimens proved that calcia grains were not being sulfated at 300°C regardless of the $SO_2$ concentration. This result is consistent with the tentative conclusion from the kinetic experiments that sulfation is limited to the oxides of sodium and potassium at 300°C. When discrete alumina rich grains were found they were not sulfated at any of the experimental sulfation temperatures.

Regenerative use of red mud for removing $SO_2$ from stack gas is limited by its poor resistance to abrasion. Sorption capacities are too low for throw-away usage at 300°C. However, injection of red mud in boilers or prior to boiler plant economizers where the temperatures are higher, followed by removal with fly ash and discard, may be economically viable for power plants near sources of red mud or accessible to inexpensive ocean transport. Red mud is very effective in removing $SO_2$ to

Reproduced from best available copy.

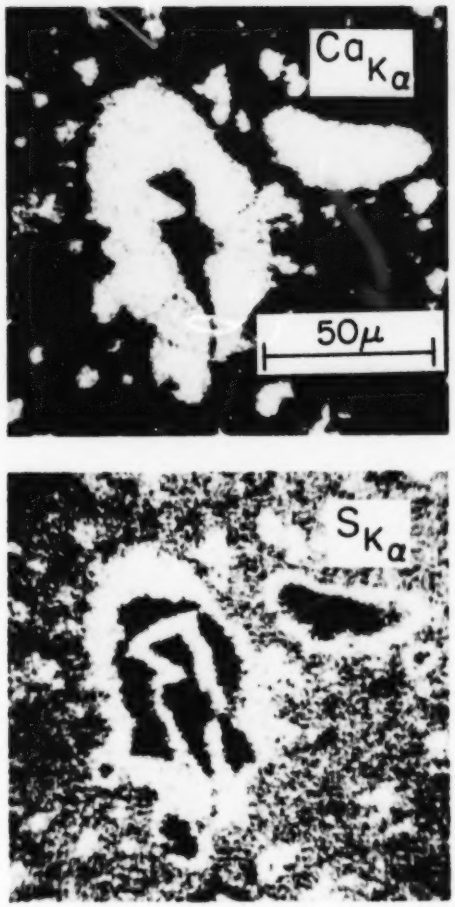


Figure 6. Calcium and sulfur fluorescent X-ray images from a partially reacted specimen.

very low residual levels, less than 0.02%, even at 300$^{o}$C provided its sorption capacity is not exceeded.

REFERENCES

(1) Lecis, P., and A. Guidi. Pyrogenic Attack of Bauxite. Extractive Metallurgy of Aluminum. Vol. 1. Ed. by G. Ferard and P.T. Stroup. Interscience Pubs. 1963. P. 231-49.

(2) Fursman, O.C., J.E. Mauser, M.O. Butler, and W.A. Stickney. Utilization of Red Mud Residues from Alumina Production. Bur. of Mines. Rep. of Inv. 7454. Nov. 1970.

(3) Abboud, H.I.. Successful Side Stream Causticization in an Alumina Plant. Extractive Metallurgy of Aluminum. Vol. 1. Ed. by G. Gerard and P.T. Stroup. Interscience Pubs. 1963. P. 265.

# DIMENSIONLESS PLOTS FOR MICROGRAIN MODELS OF REACTING POROUS SOLIDS WITH APPROXIMATIONS TO A SIMPLE LOGARITHMIC CONVERSION OF THE SOLIDS

## INTRODUCTION

The kinetic description of a catalytic reaction occurring on the internal surfaces of porous solids is generally expressed in terms of a surface rate and an effectiveness factor, which accounts for the reaction impedance due to diffusion through pores to and from the reacting surface. The specific surface area and pore structure are generally constant. When the porous solid is reacting, rather than only providing a catalytic surface of constant area, these conditions are not generally met and phenomenological description of the kinetic process is considerably complicated. The reaction may involve conversion of one solid to another solid reaction product, as in the reaction between sulfur dioxide and porous sodium aluminate to form sodium sulfate,[1] or the reaction product may be a fluid, as in the oxidation of coke[2] where CO or $CO_2$ are produced.

The porous solid can be reasonably described as a pellet consisting of a collection of micrograins often of variable size, at least partially surrounded by interconnecting pores. As with catalytic processes the rate may be completely or partially controlled by pore diffusion of reactants to and from the micrograins. The rate controlling step may also be either a chemical reaction at the surface of the micrograins or solid state diffusion through the solid reaction product layer surrounding the micrograin at a rate much slower than the pore diffusion limiting rate.

Pore diffusion through the micrograin reaction product shell can generally be eliminated since the diffusion distances involved are usually very much less than pore diffusion distances through the bulk of the pellet.[3] In either case, for each micrograin there is a shrinking core of unreacted material which may be surrounded by the solid reaction product. Reaction proceeds until the micrograin is consumed and smaller micrograins are consumed before larger ones. The extensive rate of reaction of the porous solid decreases with time because of the progressive elimination of active micrograins that have reacted completely. Even when the micrograin size distribution is uniform, the extensive rate will decrease with time either because of the decreasing surface area of each micrograin and its effect on the surface chemical reaction controlled rate or because of the increasing reaction product shell thickness surrounding the micrograins and its effect on the shell diffusion controlled reaction rate.

Szekely and Evans[4,5] have used this shrinking, quasi-spherical micrograin model and developed rate equations for the case involving both pore diffusion and a first order surface chemical reaction on the shrinking micrograin surface. By their model the micrograins are uniformly sized and diffusion through the micrograin shell is assumed to be rapid. They can treat pore diffusion controlled kinetics, surface chemical reaction controlled kinetics and mixed kinetic systems. Numerical solutions of the rate equations coupled with a computational program are required for each application of the model.

In the present paper porous solid reactions are considered using the quasi-spherical micrograin physical model for sufficiently slow reactions that pore diffusion in the pellet is not rate controlling, i.e., when the effectiveness factor, $\phi \approx 1$. Several possible micrograin size

distributions for porous solids are considered. In order to provide general rather than limited utility, the computed results are presented as dimensionless plots of the fractional conversion, F, versus the fractional reaction time, $t/\tau$, where $\tau$ is the time required for complete conversion of the porous solid, which is identically the time required for complete conversion of the largest micrograin in the porous pellet. For normal and log-normal micrograin size distributions $\tau$ is the time required for complete reaction of the average size micrograin. Dimensionless conversion curves are given for reacting systems where the rate controlling step is (a) solid-state micrograin shell diffusion and (b) surface chemical reaction of any reaction rate order. The surface chemical rate constant and shell diffusivities must remain constant during the reaction period, which usually constrains the results to isothermal conditions.

A uniform micrograin size and three classes of micrograin size distributions are considered: (a) the Gates-Gaudin-Schuhmann (GGS) distribution, which is an empirical equation describing the size distribution that results when dense brittle solids are fragmented,[6-8] (b) log-normal distributions, and (c) normal distributions. In each category various size distributions result, depending on the characteristic parameters of the size distribution equations. A primary goal of this paper is to describe how changes in these parameters effect extensive rates and in particular the shape of the dimensionless fractional conversion curves. Results are compared with the empirical logarithmic conversion rates (or quasi-first order solid conversion rates) in which the rate is proportional to the unreacted fraction of solid. This has been observed for several internally reacting porous solids.[1,9-11]

## KINETIC EQUATIONS AND MICROGRAIN SIZE DISTRIBUTIONS

Equations developed for heterogeneous chemical reactions involving discrete spherical pellets exhibiting the core/shell reaction morphology are reviewed by Levenspiel.[12] In a previous paper[13] these equations were coupled with the GGS particle size distribution to compute the extensive rate of conversion of an unattached aggregation of ground particles. This approach is now being applied to an aggregation of attached micrograins constituting a porous solid pellet. Rate expressions for surface chemical reaction and shell diffusion controlled rates are summarized in Table 1. For each particle radius, $R_i$, the fraction unreacted, $1-F(t,R_i)$, must be computed as a function of time. The aggregate fraction reacted, $F(t)$, depends on the fractional conversion of each micrograin size and the volume fraction of total initial micrgrains having the specified size. Expressed as discrete size fractions, which facilitate machine computation, the fractional reaction of the porous solid is,

$$F(t) = 1 - \underbrace{\sum \left|1-F(t,R_i)\right| \Delta Y(R_i)}_{\text{all } R_i \text{ with } \tau(R_i) > t} \qquad (1)$$

where $\tau(R_i)$ is the time required for complete conversion of micrograins with radius, $R_i$, and $\Delta Y(R_i)$ is the volume fraction of micrograins in the porous solid with radius between $R_i-\Delta R_i$ and $R_i$ subject to the normalizing condition that the sum of discrete fraction is

$$\sum_{\text{all } R_i} \Delta Y(R_i) = 1 \qquad (2)$$

In all computations $R_i$ is expressed as a fraction of $R_*$ and the radius increments were from $\Delta R_i = .0001\ R_*$ to $\Delta R_i = .01\ R_*$ depending on the range of sizes involved.

## The Gates-Gaudin-Schuhmann Distribution

Porous solids obtained by sintering or otherwise aggregating a mixture of uniformly sized micrograins will exhibit the same uniform micrograin size providing the sintering time and temperature are not sufficiently high to cause secondary grain growth or recrystallization. Oversintering will substantially lower the internal surface area and reactivity of the solid. Consequently, only the minimum amount of sintering required to yield adequate handling strength is normally used.

Porous solids produced by light sintering of comminuted particles should exhibit a Gates-Gaudin-Schuhmann micrograin size distribution, which is described by the following expression:

$$Y(R_i) = (R_i/R_*)^m \tag{3}$$

where $Y(R_i)$ is the cumulative volume fraction smaller than $R_i$ and $R_*$ is the largest micrograin size in the distribution. Differentiation gives the volume fraction of micrograins, $\Delta Y(R_i)$ in the size range between $R_i - \Delta R_i$ and $R_i$:

$$\Delta Y(R_i) = \frac{m(R_i)^{m-1} R_i}{(R_*)^m} \tag{4}$$

The size distribution is fixed by specification of $R_*$ and m.

The GGS parameter for comminuted solids is usually near 1 and hardly ever exceeds the range: $0.7 \leq m \leq 1.0$. Equation (4) conforms with the total summation requirement of equation (2).

Fractional conversion equations for surface chemical reaction and shell diffusion rate controlling processes are shown in Table 1. In making the computations $R_i$ and $\Delta R_i$ are expressed as fractions of $R_*$.

Table 1. FRACTIONAL CONVERSION EQUATIONS FOR POROUS SOLIDS WITH VARIOUS MICROGRAIN SIZE DISTRIBUTIONS

| Micrograin Rate Controlling Mechanism | Surface Chemical Reaction | Shell Diffusion |
|---|---|---|
| Rate Equation for a Single Micrograin | $1 - (1-F)^{1/3} = \dfrac{(M)/\rho)_c\ (-r_s)t}{R_i}$ <br> where: <br> $-r_s = k_c\ C_A^n$ | $1 + 2(1-F) - 3(1-F)^{2/3} = \dfrac{6(M/\rho)_c \nu D_{AB}\left(C_{A_o} - C_{A_c}\right)t}{R_i^2}$ |
| Volume Fraction Reacted for Uniformly Sized Micrograins $F(t,R_i)$ | $F(t,R_i) = 1 - \left(1 - \dfrac{t}{\tau(R_i)}\right)^3$ [for $t \leq \tau(R_i)$] <br> where: <br> $\tau(R_i) = \dfrac{R_i}{(M/\rho)_c(-r_s)}$ | $F(t,R_i) = 1 - \left\{\dfrac{1}{2} + \cos\left(\dfrac{\theta + 4\pi}{3}\right)\right\}^3$ [for $t \leq \tau(R_i)$] <br> where: <br> $\theta = \cos^{-1}\left[\dfrac{2t}{\tau(R_i)} - 1\right]$ <br> $\tau(R_i) = \dfrac{R_i^2}{6(M/\rho)_c \nu D_{AB}\left(C_{A_o} - C_{A_c}\right)}$ |
| Volume Fraction Reacted for a Gates-Gaudin-Schuhmann Size Distribution of Micrograins $F_{GGS}(t)$ | $F_{GGS}(t) = 1 - \sum\left(1 - \dfrac{t}{\tau(R_i)}\right)^3 \left(\dfrac{m(R_i)^{m-1}\ \Delta R_i}{R_*^m}\right)$ <br> all $R_i$ with $\tau(R_i) > t$ | $F_{GGS}(t) = 1 - \sum\left\{\dfrac{1}{2} + \cos\left(\dfrac{\theta + 4\pi}{3}\right)\right\}^3 \left(\dfrac{m(R_i)^{m-1}\ \Delta R_i}{R_*^m}\right)$ <br> all $R_i$ with $\tau(R_i) > t$ |

Table 1 (continued)

| Micrograin Rate Controlling Mechanism | Surface Chemical Reaction | Shell Diffusion |
|---|---|---|
| Volume Fraction Reacted for a Log-Normal Distribution of Micrograins $F_{LN}(t)$ | $F_{LN}(t) = 1 - \sum_{\substack{\text{all } R_i \text{ with} \\ \tau(R_i) > t}} \left(1 - \frac{t}{\tau(R_i)}\right)^3 \left( \frac{\Delta R_i}{\sqrt{2\pi}\ \sigma_g\ R_i} \cdot \exp\left[ \frac{-1}{2\sigma_g^2} \left( \ell n\ R_i - \ell n\ \bar{R}_{vg} \right)^2 \right] \right)$ | $F_{LN}(t) = 1 - \sum_{\substack{\text{all } R_i \text{ with} \\ \tau(R_i) > t}} \left\lvert \frac{1}{2} + \cos\left(\frac{\theta + 4\pi}{3}\right) \right\rvert^3 \left( \frac{\Delta R_i}{\sqrt{2\pi}\ \sigma_g\ R_i} \cdot \exp\left[ \frac{-1}{2\sigma_g^2} \left( \ell n\ R_i - \ell n\ \bar{R}_{vg} \right)^2 \right] \right)$ |
| Volume Fraction Reacted for a Normal Number Distribution of Micrograin Radii $F_N(t)$ | $F_N(t) = 1 - \sum_{\substack{\text{all } R_i \text{ with} \\ \tau(R_i) > t}} \left(1 - \frac{t}{\tau(R_i)}\right)^3 \left[ \frac{R_i^3\ \Delta n(R_i)}{\sum_{\text{all } R_i} [R_i^3\ \Delta n(R_i)]} \right]$ | $F_{NR}(t) = 1 - \sum_{\substack{\text{all } R_i \text{ with} \\ \tau(R_i) > t}} \left\lvert \frac{1}{2} + \cos\left(\frac{\theta + 4\pi}{3}\right) \right\rvert^3 \left[ \frac{R_i^3\ \Delta n(R_i)}{\sum_{\text{all } R_i} [R_i^3\ \Delta n(R_i)]} \right]$ |
| | where $\Delta n(R_i) = \frac{\Delta R_i}{\sqrt{2\pi}\ \sigma} \exp\left[ \frac{-1}{2\sigma^2} (R_i - \bar{R}_n)^2 \right]$ | |

## Log-Normal Distributions

Direct evidence of micrograin size distributions in porous solids is difficult to obtain. The pore size distribution can be obtained using adsorption-condensation techniques and mercury porosimetry. In highly porous solids, the pore volume and solids volume are usually comparable and when there is high internal surface area, the micrograin size distribution may be inferred from the pore size distribution.

The log-normal distribution law has been shown to adequately describe a number of ceramic microstructures, porous solids and other particulate systems.[14-15] The log-normal distribution written on a volume basis is

$$\frac{d(Y(R_i))}{dR_i} = \frac{1}{\sqrt{2\pi}\ \sigma_g\ R_i} \exp\left[\frac{-1}{2\sigma_g^2}\left(\ell n\ R_i - \ell n\ \bar{R}_{vg}\right)^2\right] \qquad (5)$$

where $R_{vg}$ is the geometric volume average micrograin radius and $\sigma_g$ is the standard deviation of the log-normal distribution. Hence, the fraction of micrograins, $Y(R_i)$, in the size range between $R_i - \Delta R_i$ and $R_i$ is

$$\Delta Y(R_i) = \frac{\Delta R_i}{\sqrt{2\pi}\ \sigma_g\ R_i} \exp\left[\frac{-1}{2\sigma_g^2}\left(\ell n\ R_i - \ell n\ \bar{R}_{vg}\right)^2\right] \qquad (6)$$

Fractional conversion equations are shown in Table 1. The volume mean radius is related to the number (population) mean radius, $\bar{R}_{ng}$, for the log-normal distribution by the relation

$$\ell n\ \bar{R}_{vg} = \ell n\ \bar{R}_{ng} + 3\sigma_g^2 \qquad (7)$$

For computational convenience the largest 1% by volume of the micrograins in the log-normal distributions were not considered within in the micrograin size range. In effect, the maximum radius $R_* = R_{99\%}$ where the subscript indicates the volume percent of solid less than the stipulated size. Also $\Sigma \Delta Y(R_i) = 0.99$. Since a small amount of material is involved, this simplification has a negligible effect on the results.

The log-normal volume distribution of micrograin sizes is fixed by specification of $\bar{R}_{vg} = R_{50\%}$ and $\sigma_g$. Both of these parameters as well as $R_i$ and $\Delta R_i$, can be specified in terms of the maximum radius, $R_* = R_{99\%}$, included in the computer iterations. This is illustrated by the log-normal probability plot of Figure 1 and Table 2, which represent a uniform micrograin size, five arbitrary log-normal distributions and two experimental log-normal distributions inferred by direct comparison with the volume distribution of measured pore sizes. The standard deviation, $\sigma_g$, is determined from the relation,

$$\sigma_g = \ell n \, R_{84.13\%} - \ell n \, \bar{R}_{vg} \tag{8}$$

The volume distribution of micrograin sizes for the arbitrary log-normal distributions are shown in Figure 2. For computing the extent of reaction it was necessary to normalize the micrograin sizes to the largest micrograin radius, arbitrarily taken as $R_{99\%}$. The standard deviation was similarly normalized; hence, the normalized standard deviation, $\Sigma_g$, is

$$\Sigma_g = \sigma_g / R_{99\%} \tag{9}$$

It is also interesting to display the radii normalized to the appropriate average micrograin radius and this has been done in plotting the curves for Figure 2. The extent of reaction will be similarly displayed.

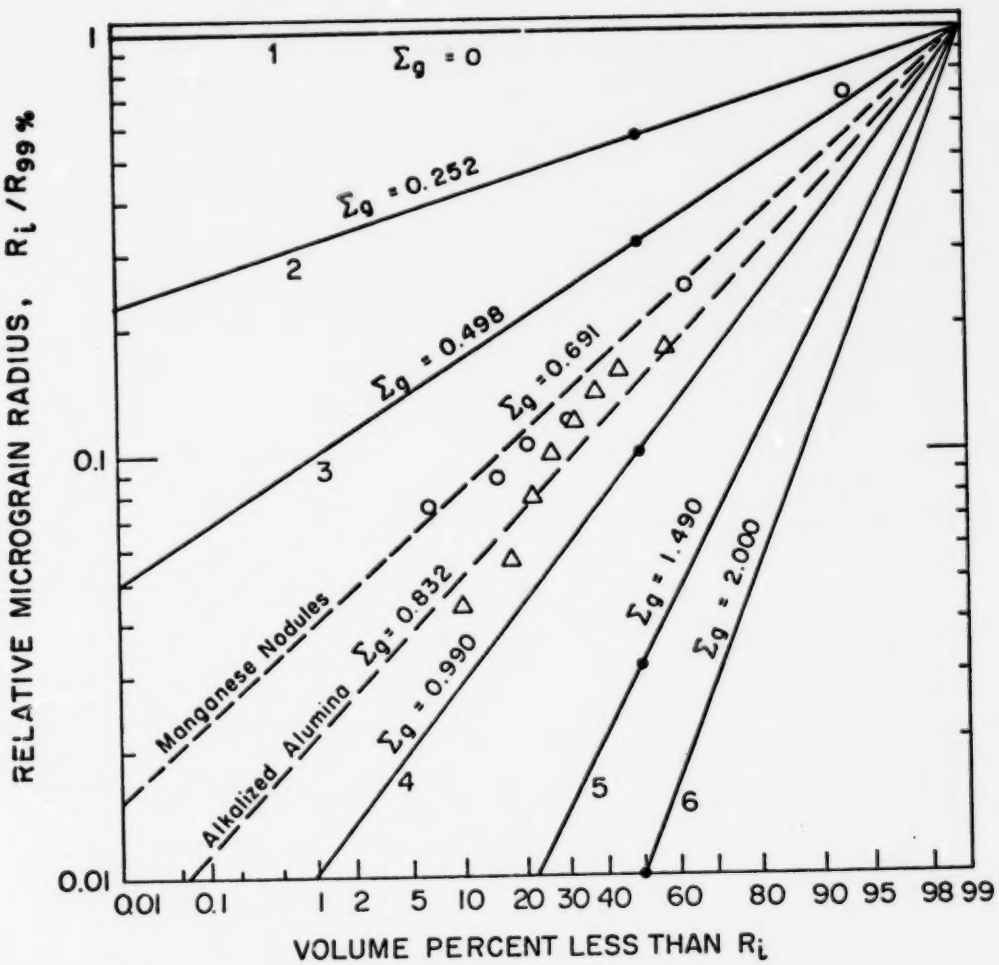


Figure 1. Log-normal probability plots of arbitrary and experimental micrograin size distributions. Refer to Table 2.

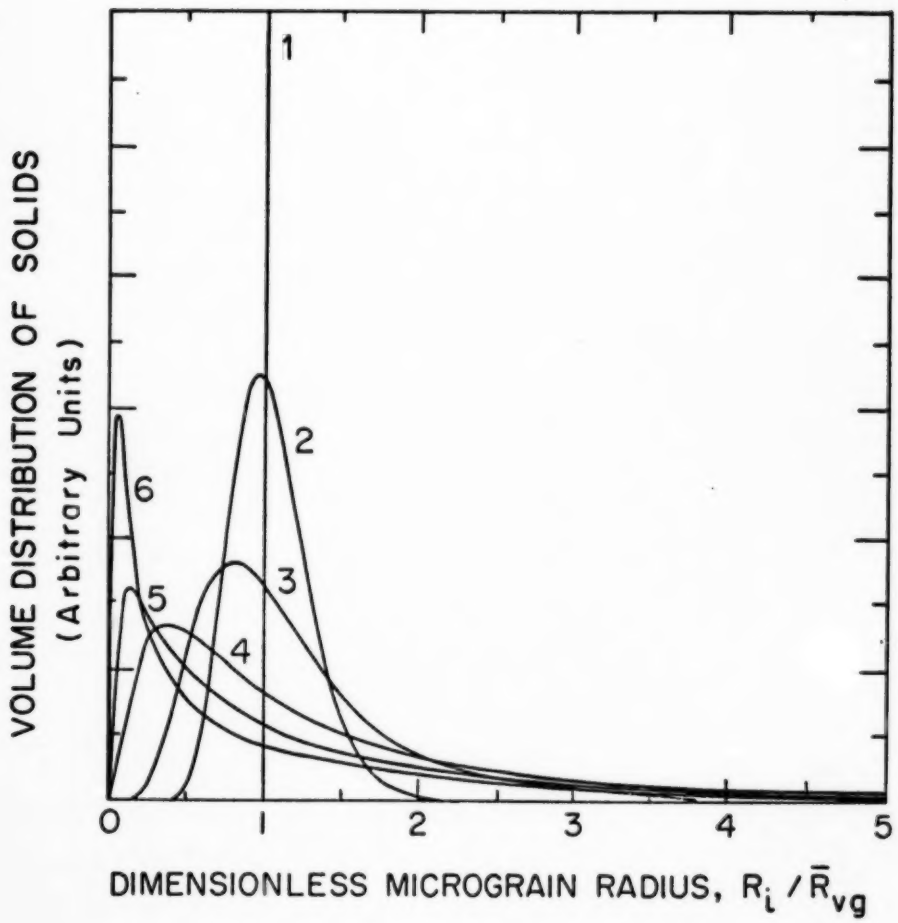


Figure 2. Volume distributions of solids for arbitrary log-normal volume distributions of micrograin radii.

Table 2. SUMMARY OF LOG-NORMAL SIZE DISTRIBUTIONS SHOWN IN FIGURES 1 AND 2

| Curve | Relative Size Distribution Range $\left(R_{99\%}/R_{1\%}\right)$ | Standard Deviation $\left(\Sigma_g=\sigma_g/R_{99\%}\right)$ | Relative Volume Mean Radius $\left(\bar{R}_{vg}/R_{99\%}\right)$ |
|---|---|---|---|
| 1 | 1.0 | 0 | 1.0 |
| 2 | 3.16 | 0.252 | 0.56 |
| 3 | 10 | 0.498 | 0.316 |
| 4 | 100 | 0.990 | 0.10 |
| 5 | 1,000 | 1.490 | 0.0316 |
| 6 | 10,000 | 2.000 | 0.010 |
| Manganese Nodules* | | 0.691 | 0.200 |
| Alkalized Alumina* | | 0.832 | 0.145 |

*Experimental Data

Normal Distributions

If the population of radii are normally distributed, then

$$\frac{dn}{dR_i} = \frac{1}{\sqrt{2\pi}\,\sigma} \exp\left[\frac{-1}{2\sigma^2}\left(R_i - \bar{R}_n\right)^2\right] \tag{10}$$

where $\sigma$ is the standard deviation and $\bar{R}_n$ is the number average radius. The volume fraction in the finite range between $R_i - \Delta R_i$ and $R_i$, subject to the normalizing constraint on the total volume, is

$$\Delta Y(R_i) = \frac{R_i^3\,(\Delta n(R_i))}{\underbrace{\sum}_{\text{all } R_i}[R_i^3\,\Delta n(R_i)]} \tag{11}$$

where $\Delta n(R_i)$ is obtained from equation (10),

$$\Delta n(R_i) = \frac{\Delta R_i}{\sqrt{2\pi}\,\sigma} \exp\left[\frac{-1}{2\sigma^2}\left(R_i - \bar{R}_n\right)^2\right] \tag{12}$$

Again, fractional conversion equations are shown in Table 1 where the fractional conversion for the normal number radius distribution is $F_N(t)$.

For computational convenience the largest 0.1% by number of the micrograin radii were not considered; hence $R_* = R_{99.9\%}$. Because of the volume bias toward the largest particle sizes elimination of the largest 1% of the micrograins, as was done for the log-normal volume distribution, significantly perturbed the results. Computations were made by expressing radii and standard deviation as a fraction of $R_{99.9\%}$; hence,

$$\Sigma = \sigma / R_{99.9\%} \tag{13}$$

Seven arbitrary values of the normalized standard deviation, $\Sigma$, were selected for making fractional conversion calculations, see Table 3.

Table 3. SUMMARY OF NORMAL DISTRIBUTIONS OF MICROGRAIN RADII; SEE FIGURES 3 AND 4

| Relative Size Distribution Range $\left(R_{99\%}/R_{10\%}\right)$ | Standard Deviation $\left(\Sigma = \sigma/R_{99.9\%}\right)$ | Number Mean Radius $\left(\bar{R}_n/R_{99.9\%}\right)$ |
|---|---|---|
| 1.11 | 0.021 | 0.932 |
| 1.24 | 0.041 | 0.867 |
| 1.61 | 0.084 | 0.732 |
| 2.3 | 0.128 | 0.60 |
| 4.0 | 0.170 | 0.47 |
| 20 | 0.215 | 0.337 |
| $(\infty)$ | 0.255 | 0.20 |

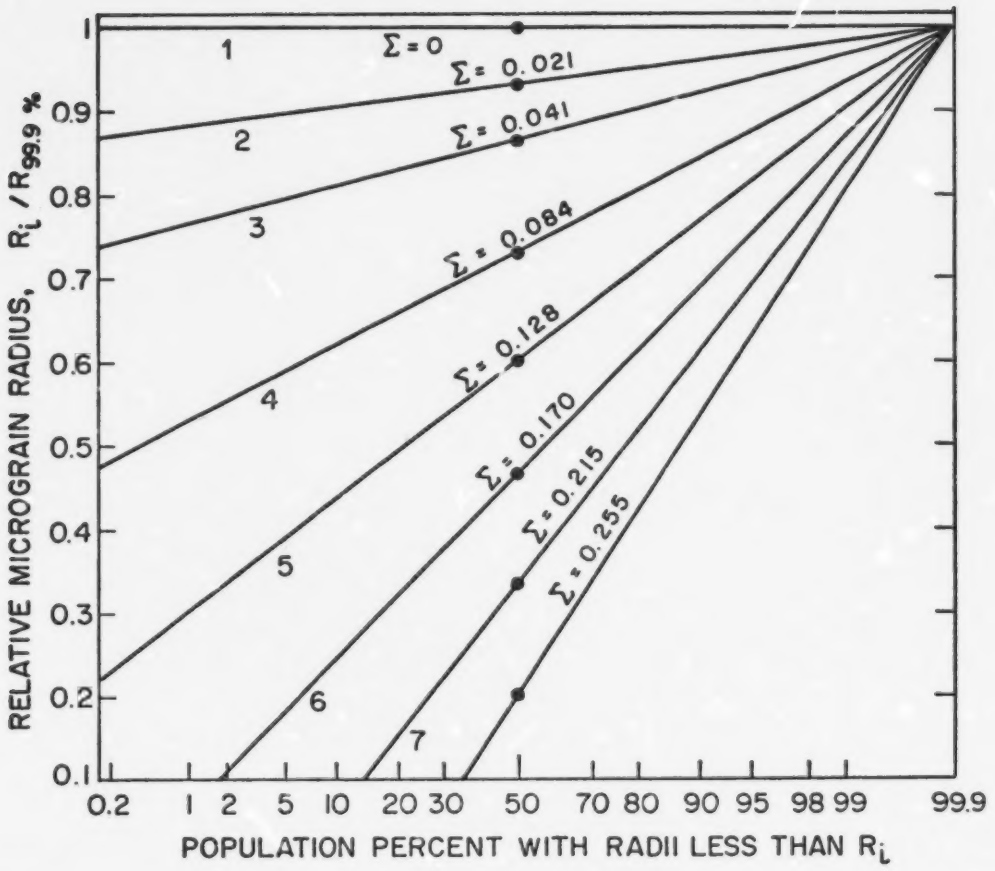


Figure 3. Normal probability plots of micrograin size distributions.

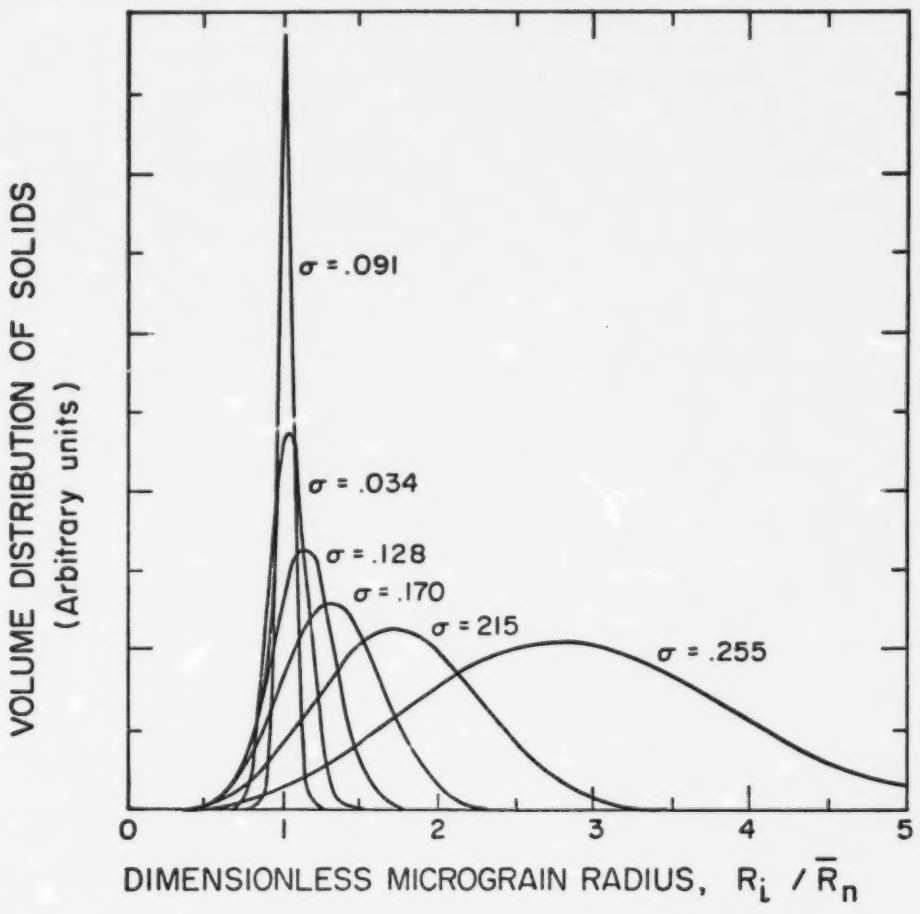


Figure 4. Volume distributions of solids for arbitrary normal number distributions of micrograin radii.

The corresponding normal probability plots are shown in Figure 3.

Volume distributions corresponding to these normal distributions with respect to micrograin radius are plotted in Figure 4. The radii are expressed in dimensionless form by normalizing with respect to the number average radius. The peaks shift to the right of $\bar{R}_n$ as $\sigma$ increases because the volume distribution, rather than number distribution, of these micrograins is being plotted in Figure 4.

## COMPUTED FRACTIONAL CONVERSIONS FOR POROUS SOLIDS

When large, nonporous, discrete particles are used, partially reacted specimens can be sectioned and examined to corroborate the kinetic mechanism determined from the rate data. However, it is generally not possible to section the micrograins of a porous solid and determine the reaction mechanism from the partial reaction morphology. Consequently, the reliability of a determination of the correct mechanism from only the experimental rates is even more critical for reacting porous solids than it is for reacting dense solids. Because the rate of reaction of a porous solid decreases with time and complete conversion is approached asymptotically, the functional plots of the aggregate fraction reacted, F, versus $t/\tau$ for each of the rate mechanisms and micrograin size distributions are all concave and the correct mechanism is difficult to resolve. Fortunately, when F is plotted against $(t/\tau)^{\frac{1}{2}}$ and $(t/\tau)^{\frac{1}{3}}$ strong differences in curvature develop that distinguish the rate mechanisms and plotting the data in this way proviues a useful tool for determining the correct rate mechanism. Consequently, dimensionless conversion curves have been computed with F plotted againt $t/\tau$, $(t/\tau)^{\frac{1}{2}}$ and $(t/\tau)^{\frac{1}{3}}$. Many porous solid reacting systems yield a straight line when log (1-F) is plotted against time. Consequently, computed conversion curves have

also been plotted as log (1-F) versus $t/\tau$.

Uniform Micrograins and the Gates-Gaudin-Schuhmann Micrograin Size Distribution

Fractional conversion, $F_{GGS}$, is plotted against dimensionless reaction time, $t/\tau(R_*)$, in Figure 5 for uniformly sized micrograins and for the GGS distribution with m=1. Solutions for an interface chemical reaction rate controlling process and for a shell diffusion rate controlling process are shown. In each of these four cases the rate decreases with reaction time and the conversion curves are concave downward.

Fractional conversion curves for these same functions are plotted against the half power and third power of dimensionless time in Figures 6 and 7, respectively. When F is plotted against $[t/\tau(R_*)]^{\frac{1}{2}}$ the shell diffusion controlled conversion rate curves remain concave for both a uniform size distribution and the GGS size distribution but the interface chemical reaction controlled rate curves are initially convex upward for both the uniform and GGS size distributions. When F is plotted against $[t/\tau(R_*)]^{\frac{1}{3}}$, only the shell diffusion controlled rate curve for a GGS distribution is always concave downward. The other three rate curves are initially convex upward. It is usually difficult to unambiguously determine $\tau(R_*)$ since complete conversion is approached asymptotically. Consequently, the preceding relationships can be used to distinguish rate controlling mechanisms in porous solids by plotting experimental fractional conversion versus real time to the first, half and one-third powers.

The rate of reaction of porous solids is often observed to be proportional to the unreacted fraction:

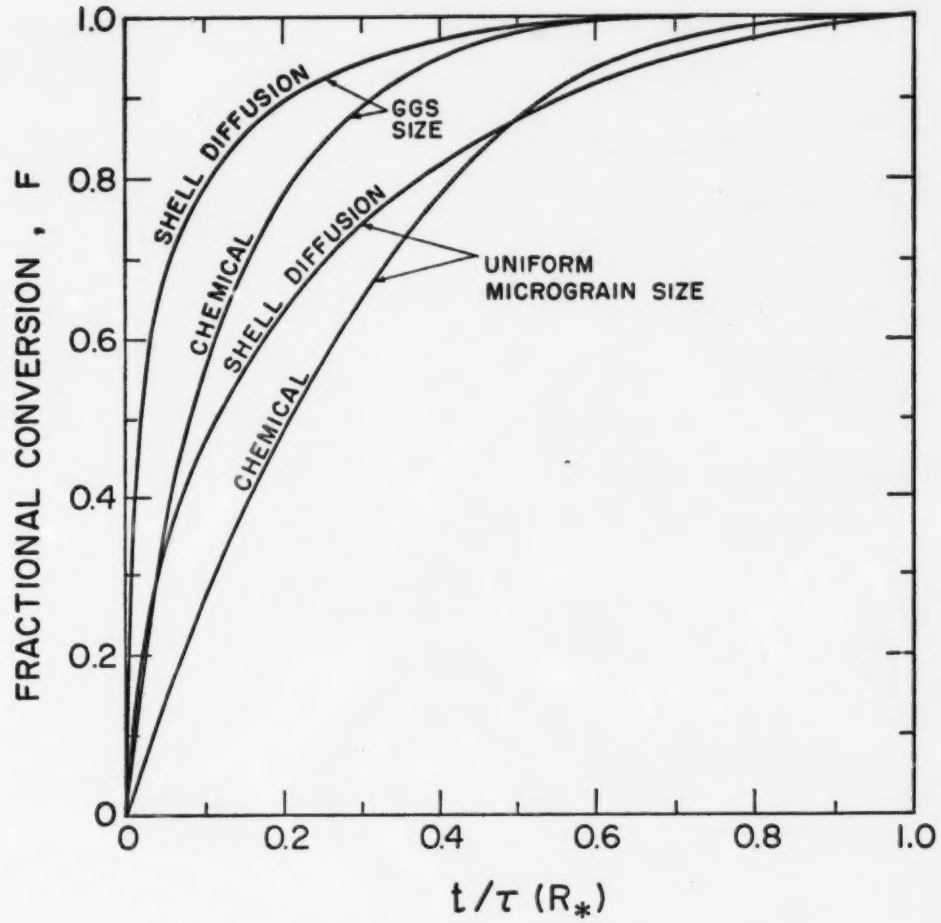


Figure 5. Aggregate reaction curves for uniform micrograin size and the Gates-Gaudin-Schuhmann distribution.

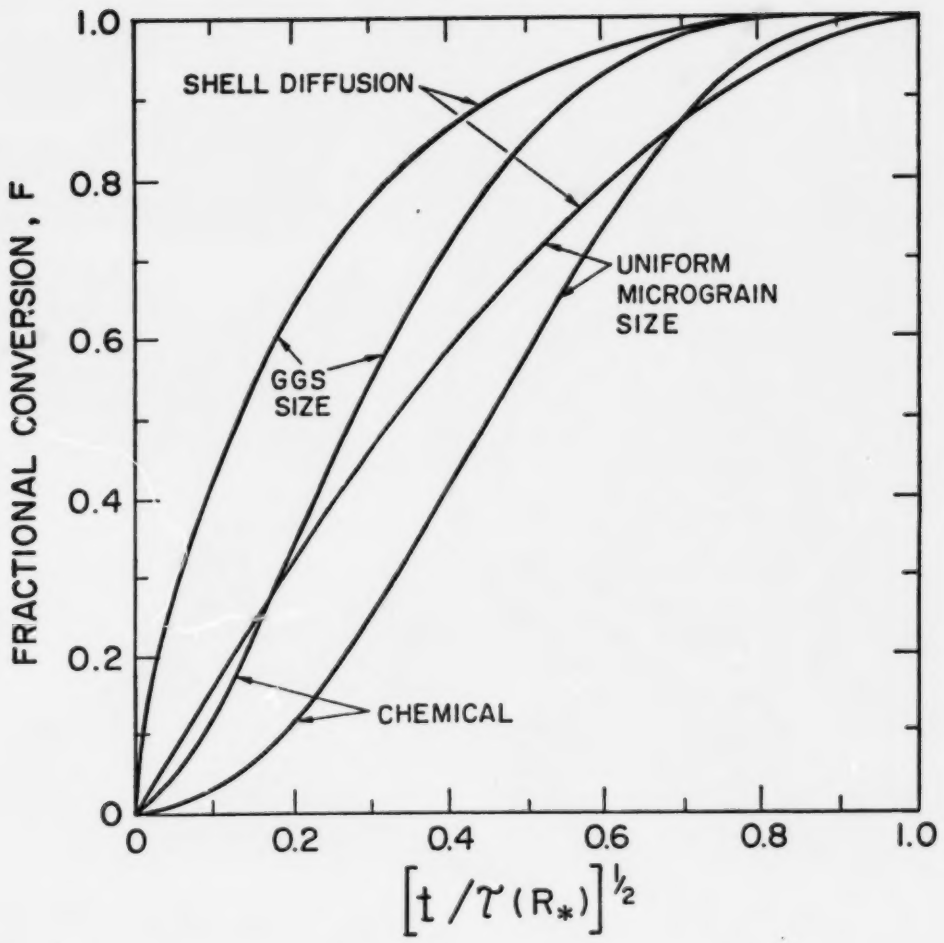


Figure 6. Aggregate reaction curves for uniform micrograin size and the Gates-Gaudin-Schuhmann distribution.

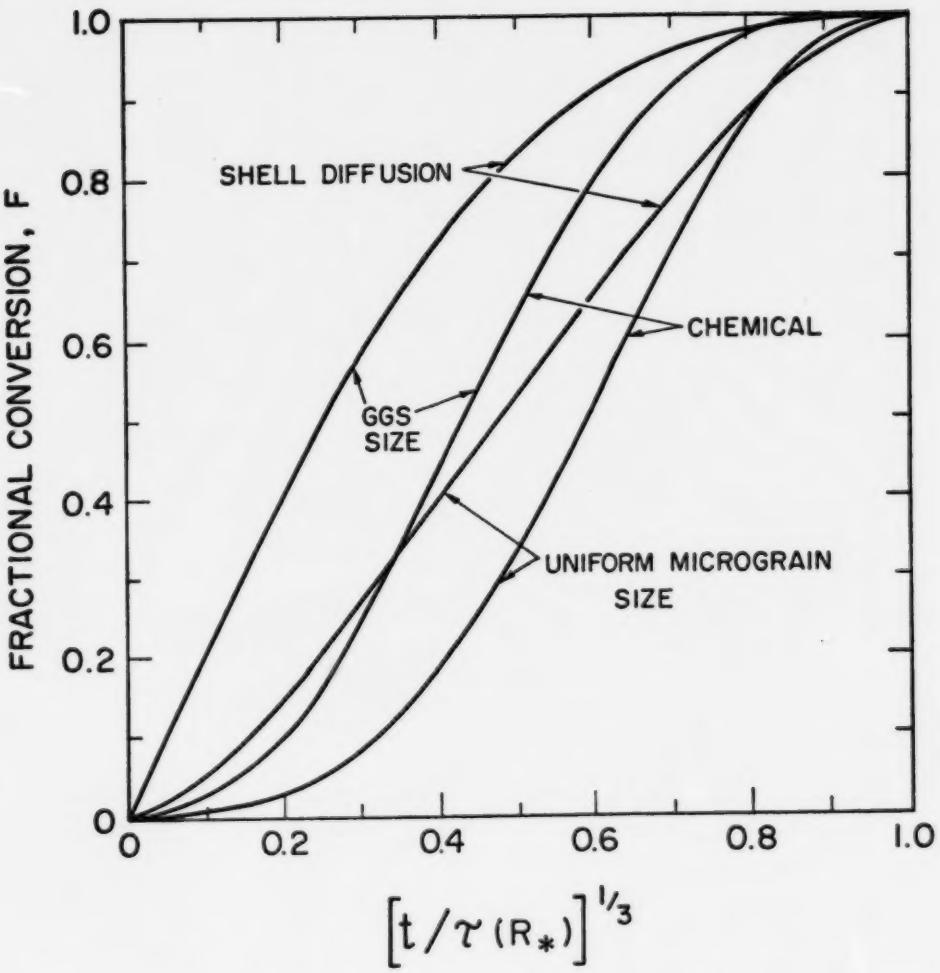


Figure 7. Aggregate reaction curves for uniform micrograin size and the Gates-Gaudin-Schuhmann distribution.

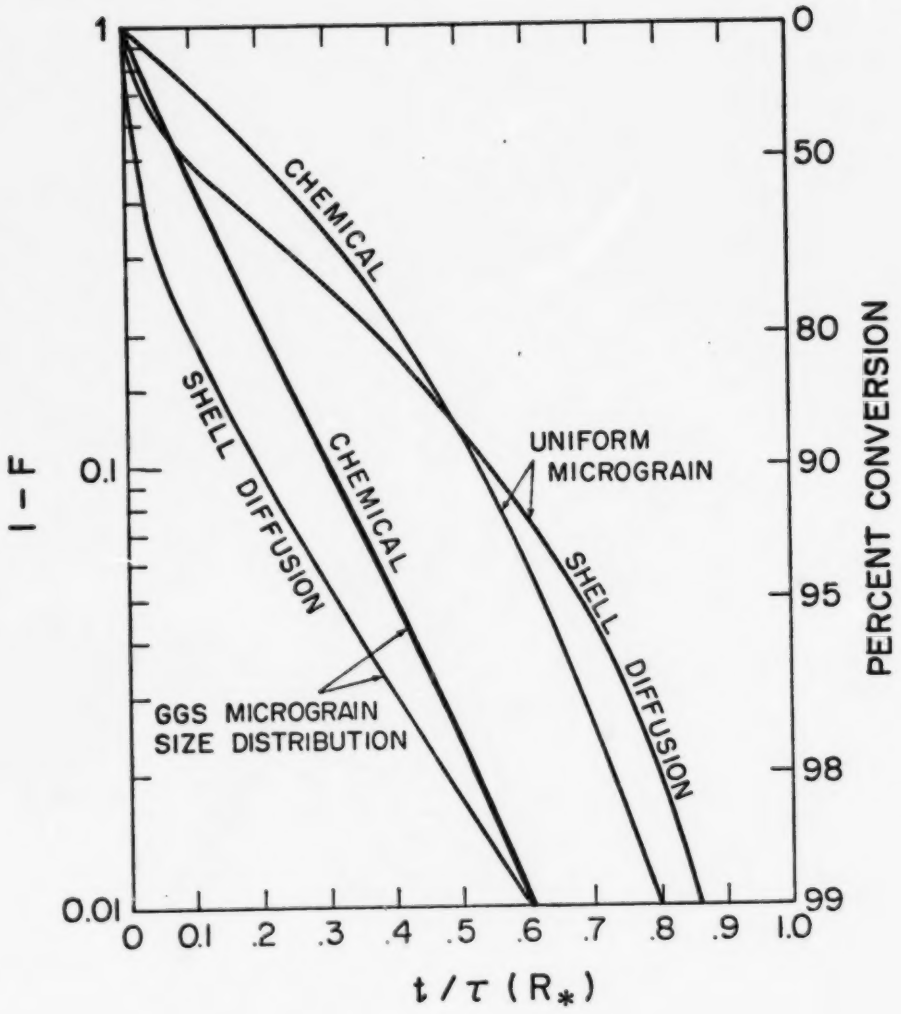


Figure 8. Logarithmic plot of aggregate reaction curves for uniform and GGS distribution.

$$-\frac{dF}{dt} \propto 1-F$$

and

$$\log (1-F) = -k_{exp}t \qquad (14)$$

A logarithmic plot of interface reaction and shell diffusion rate controlling processes for both uniform micrograins and the GGS size distribution is shown in Figure 8. The interface chemical reaction controlled rate for a GGS micrograin size distribution plots as a very nearly straight line. The other three functions show wide deviations from a straight line on a logarithmic plot and these mechanisms cannot be rate controlling for porous solid reactions that are observed to follow the logarithmic behaviour.

Log-Normal Micrograin Size Distribution

Our paramount interest in the computed results is the extent to which they approximate a straight line when displayed in the form of a logarithmic plot. If shell diffusion is rate controlling the logarithmic plots do not approximate straight lines, because of the rapid initial reaction rates and very slow terminal reaction rates of micrograins, regardless of the standard deviation used in defining the log-normal distribution.

The computations are more interesting when the surface chemical reaction occurring at the surface of the shrinking unreacted micrograin core is rate controlling. The results are plotted in Figures 9 and 10. Fractional conversion, $F_{LN}$, is plotted against dimensionless reaction time, $t/\tau(\bar{R}_{vg})$ in Figure 9. The logarithmic plots are shown in Figure 10. The reaction time has been normalized to the time required for complete reaction of a micrograin with radius equal to the volume mean

radius, $\bar{R}_{vg}$. The curves shown are the solutions to the equation,

$$F_{LN}(t) = 1 - \sum_{\text{all } R_i \text{ with } \tau(R_i) > t} \left(1 - \frac{t}{\tau(R_i)}\right)^3 \left(\frac{\Delta R_i}{\sqrt{2\pi}\,\sigma_g R_i} \exp\left[\frac{-1}{2\,\sigma_g^2}\left(\ell n\, R_i - \ell n\, \bar{R}_{vg}\right)^2\right]\right) \quad (15)$$

also summarized in Table 1, for the normalized standard deviations listed in Table 2 and used in Figures 1 and 2. Curve 1 represents the conversion of a porous solid containing uniformly sized micrograins and is identical with a conversion curve shown in Figure 5.

As the standard deviation increases from $\Sigma$=0, the distribution of micrograin sizes broadens into both smaller and larger sizes than the average size (see Figure 2). The effect of this on conversion is to accelerate the rate initially, when compared with a uniform micrograin size, because of the subaverage sized micrograins. However, as the reaction continues the aggregate conversion becomes less than that for a uniform micrograin size because of the much slower conversion of larger than average micrograins.

In the case of the empirical GGS distribution it has been shown that the size distribution parameter m is near m=1 for most systems where this distribution is an appropriate description of the size distribution. However, various choices of the size distribution parameters (standard deviations) for the log-normal and normal distributions need to be considered. Hence, plotting the computed conversions against dimensionless time raised to various fractional powers for a variety of $\Sigma$ values does not appear fruitful. However, the frequent observation of the empirical logarithmic conversion for porous solids prompts a display of the computed conversions on this basis. Such a plot for conversion by a surface chemical reaction rate controlling mechanism is shown

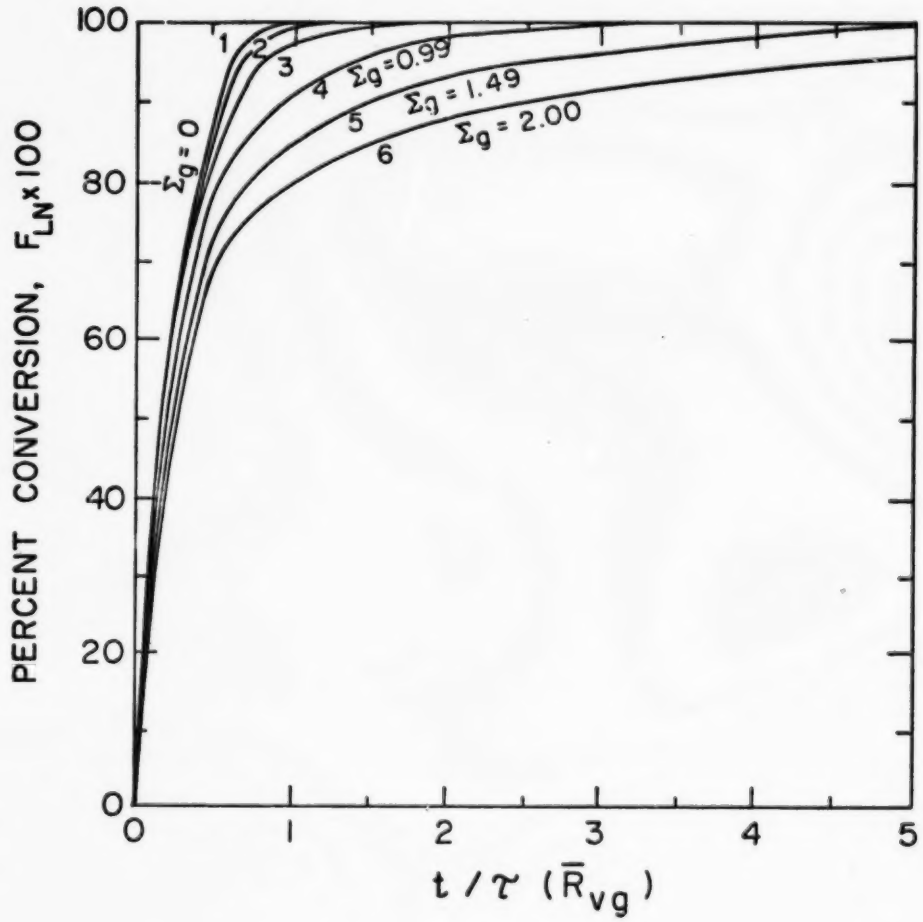


Figure 9. Aggregate conversion by surface chemical reaction for log-normal distributions of micrograin sizes.

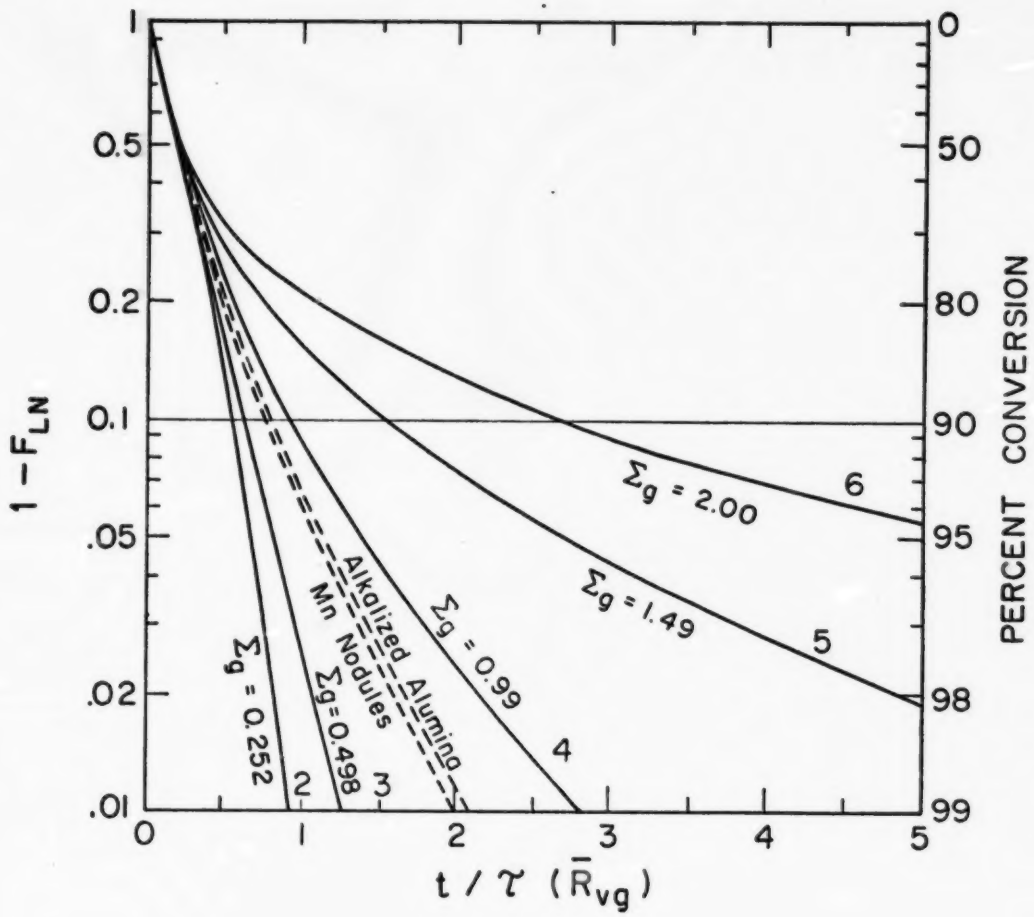


Figure 10. Logarithmic plot of conversion by surface chemical reaction for log-normal distributions of micrograin sizes.

in Figure 10. Several curves corresponding to various values of $\Sigma$ previously used are shown. Conversion for a uniform micrograin size plots as a slightly concave downward curve. However, as the standard deviation increases, the conversion curve becomes straighter and for a fairly wide variation in the micrograin size range it would not be experimentally possible to distinguish the correct log-normal curvature from a straight line plot. The conversion plot for the size distribution of curve 3 of Figure 2, $\Sigma = 0.498$, is virtually a straight line.

As the particle size distribution continues to broaden further, the logarithmic conversion curve becomes concave upward. However, for most experimental data plotted out to 90% conversion this curvature would not be noticeable unless the standard deviation was about that of curve 4 of Figure 2 ($\Sigma = 0.99$), or perhaps somewhat larger. In this connection it is important to note that the conditions of curve 4 involve a very wide distribution of micrograin sizes. The size separating the largest 1% from the remainder is 100 times larger than the size separating the smallest 1% from the remainder. Hence, it seems reasonable to expect that real size distributions that conform reasonably well with a log-normal distribution will usually be less broadly distributed than the arbitrary example of curve 4. Furthermore, in most real cases there will be some deviation in sizes; hence, $\Sigma > 0$. Consequently, the experimental logarithmic fractional conversion plots for many natural porous reacting systems, where the rate is controlled by a surface chemical reaction at the micrograin wall, are expected to plot as a nearly straight line.

Normal Micrograin Size Distributions

When the number of micrograin radii are normally distributed and the

standard deviation is increased, the volume distribution is both broadened and shifted so that the volume peak occurs at ever higher values of the radii. Consequently, for the same average radius, $\bar{R}_n$, the rate of aggregate fractional conversion decreases with an increase in standard deviation. This is shown in Figure 11 which is a plot of the solution to

$$F_N(t) = 1 - \sum_{\substack{\text{all } R_i \text{ with} \\ \tau(R_i) > t}} \left(1 - \frac{t}{\tau(R_i)}\right)^3 \left[\frac{R_i^3 \, \Delta n(R_i)}{\sum_{\text{all } R_i} R_i^3 \, \Delta n(R_i)}\right] \tag{16}$$

Standard deviations used previously in Figures 3 and 4 were used. Unlike the case for a log-normal volume distribution which tends to maximize the numbers of small particles, an increase in standard deviation of the normal distribution decreases the aggregate conversion rate later in the reaction period as well as at the beginning of reaction.

Logarithmic plots of the computed results are shown in Figure 12. The resulting curves are always slightly concave downward. Hence, if a reacting porous solid has a normal micrograin size distribution and its rate of reaction is controlled by a surface chemical reaction, agreement with the simple logarithmic plot should not be observed. Conversely, experimental compliance with the logarithmic plot indicates that the actual micrograin size distribution is probably better described by a log-normal distribution than a normal distribution.

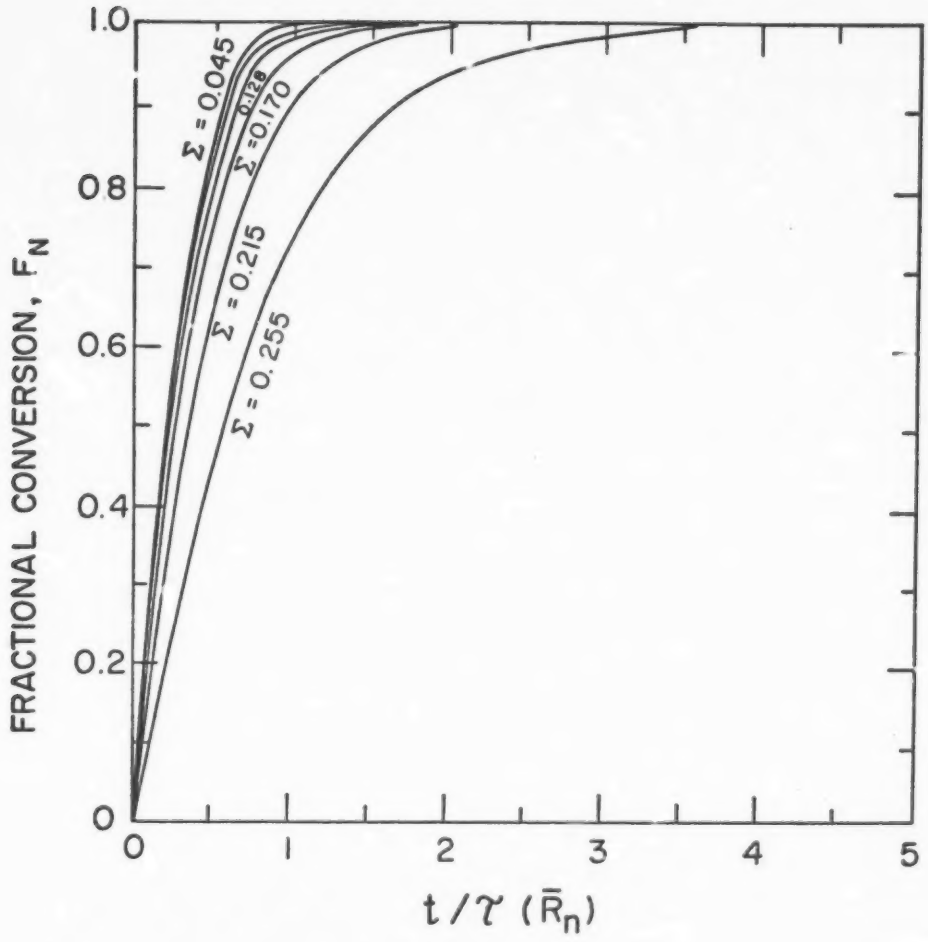


Figure 11. Aggregate conversion by surface chemical reaction for normal distributions of micrograin sizes.

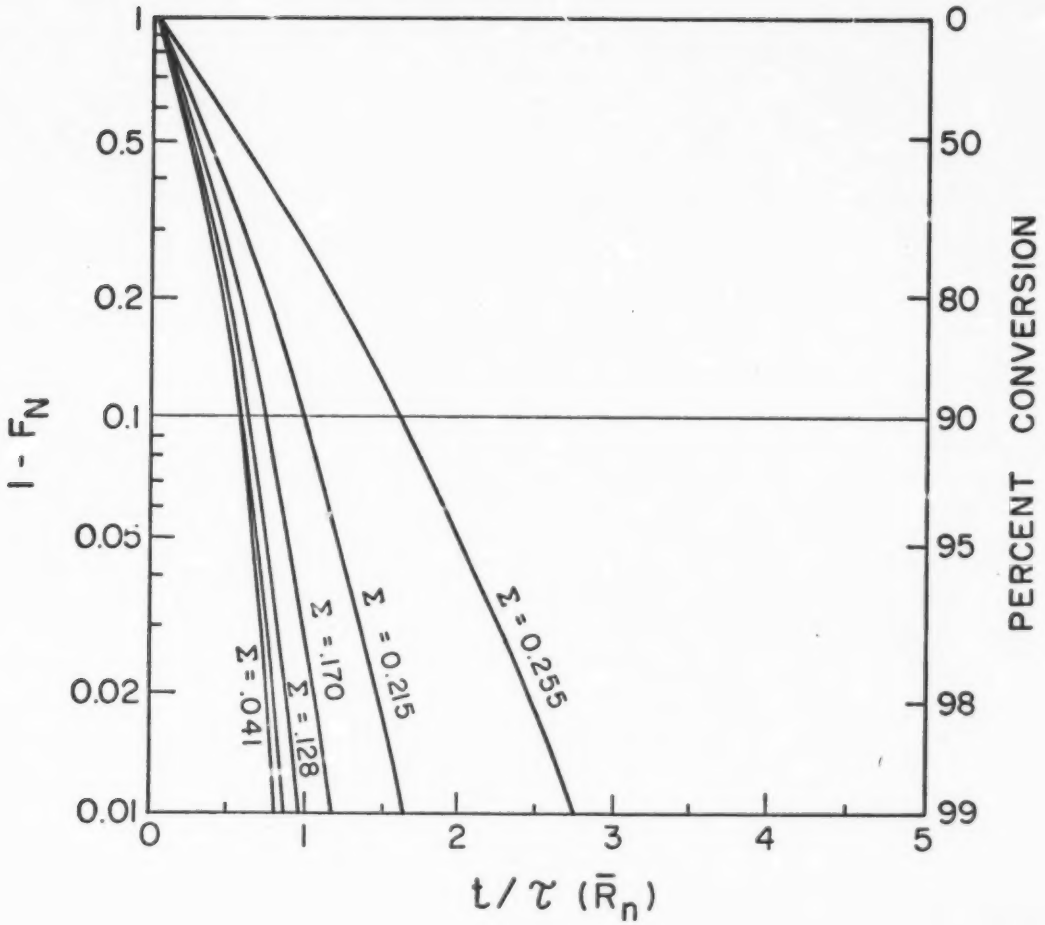


Figure 12. Logarithmic plot of conversion by surface chemical reaction for normal distributions of micrograin sizes.

NOMENCLATURE

| | |
|---|---|
| $F(t)$ | = Fraction of Solid Reacted in Time, t. |
| $F_{GGS}$ | = Fraction Reacted for a Gates-Gaudin-Schuhmann Micrograin Size Distribution. |
| $F_N$ | = Fraction Reacted for a Normal Number Distribution of Micrograin Radii. |
| $F_{LN}$ | = Fraction Reacted for a Log-Normal Distribution of Radii. |
| $k_{exp}$ | = Experimental Rate Constant in a Logarithmic Rate Expression (eqn. 14). |
| $n$ | = Number of Micrograins. |
| $\Delta n(R_i)$ | = Number of Micrograins With Radius Between $R_i - \Delta R_i$ and $R_i$. |
| $m$ | = Gates-Gaudin-Schuhmann Size Distribution Parameter. |
| $R_i$ | = Radius of i indexed micrograins. |
| $\bar{R}_{vg}$ | = Volume Mean Radius in a Log-Normal Distribution of Micrograin Radii. |
| $\bar{R}_n$ | = Number Mean Radius in a Normal Distribution of Micrograin Radii. |
| $R_*$ | = Maximum Radius of Micrograins in the Range of Sizes Computed. |
| $R_{99\%}$ | = Radius of Micrograins Such That 99% of the Total Volume in a Log-Normal Distribution Consists of Smaller Micrograins. |
| $R_{99.9\%}$ | = Radius of Micrograins Such That 99.9% of the Total Number of Micrograins in a Normal Distribution Are Smaller. |
| $t$ | = Time. |
| $\tau$ | = Time Required for Complete Reaction. |
| $\tau(R_i)$ | = Time Required for Complete Reaction of Micrograins With Radius $R_i$. |
| $\Delta Y(R_i)$ | = Volume Fraction of Solid With Radius Between $R_i - \Delta R_i$ and $R_i$. |
| $\sigma$ | = Standard Deviation of a Normal Size Distribution. |

$\sigma_g$ = Standard Deviation of a Log-Normal Size Distribution.

$\Sigma$ = Normalized Standard Deviation of a Normal Distribution, $\Sigma=\sigma/R_*$.

$\Sigma_g$ = Normalized Standard Deviation of a Log-Normal Distribution, $\Sigma_g=\sigma_g/R_*$.

$n$ = Reaction Rate Order.

$-r_s$ = Heterogeneous Chemical Reaction Rate.

$k_c$ = Heterogeneous Reaction Rate Constant.

$C_A$ = Concentration of Reacting Species A.

$C_{A_o}-C_{A_c}$ = Concentration Difference Across Reaction Product Shell.

$D_{AB}$ = Micrograin Shell Diffusion Coefficient.

$(M/\rho)_c$ = Molar Volume of the Reacting Solid.

| | |
|---|---|
| $\eta$ | effectiveness factor |
| $\lambda$ | thermal conductivity |
| $\nu$ | appropriate stoichiometric ratio relating diffusion equivalents to reaction equivalents |
| $\Phi_s$ | Thiele modulus |
| $\Phi$ | dimensionless modulus containing only observable or predictable quantities |
| $\tau$ | tortuosity |

REFERENCES


(1) Chapter 2 of this Report.

(2) Tien, R.H. and E.T. Turkdogan. Carbon. 8:607. 1970.

(3) Satterfield, C.N. Mass Transfer in Heterogeneous Catalysis. M.IKT. Press, Cambridge, Mass. p. 204.

(4) Szekely and J.W. Evans. Met. Trans. 2:169. 1971.

(5) Szekely and J.W. Evans. Chem. Eng. Sci. 25:1095. 1970.

(6) Harris, C.C. Trans. SME-AIME. 241:343. 1968.

(7) Schuhmann, R. Trans. SME-AIME. 217:22. 1960.

(8) Herbst, J.A. and D.W. Fuerstenau. Trans. SME-AIME. 241:538. 1968.

(9) Turkdogan, E.T. and J.V. Vinters. Met. Trans. 2:3175. 1971.

(10) Chapter 3 of this Report.

(11) Chapter 4 of this Report.

(12) Levenspiel, O. Chemical Reaction Engineering. J. Wiley & Sons, New York. 1962. Chapt. 12.

(13) Bartlett, R.W. Met. Trans. 2:2999. 1971.

(14) Aitchison, J. and J.A.C. Brown. The Log-Normal Distribution. Cambridge University Press, Cambridge, England. 1963. p. 176.

(15) Underwood, E.E., A.R. Colcord, and R.C. Waugh. Quantitative Relationships for Random Microstructures. In Ceramic Microstructures. Ed. R.M. Fulrath and J.A. Pask. J. Wiley & Sons, New York. 1968. Chapt. 1.

## APPENDIX

## MASS AND HEAT TRANSFER DURING SULFATION

### ESTIMATION OF EFFECTIVE DIFFUSION COEFFICIENT

The bulk diffusion coefficient $D_{12}$($SO_2$ in $O_2$) was estimated using the Chapman-Enskog theory.

The Knudsen equation was used for the Knudsen diffusion coefficient

$$D_k = 9.7 \times 10^3 \, r_e \sqrt{\frac{T}{M}} \qquad \text{(A1)}$$

where

$r_e$ is the average pore radius,

$T$ is the temperature

and $M$ is the molecular weight.

The effective diffusion coefficients for both diffusions in porous solids are given by

$$D_{12_{eff}} = D_{12} \theta / \tau$$

$$D_{k_{eff}} = D_k \, \theta^2 / \tau$$

where

$\theta$ is the void fraction of the porous solid

and $\tau$ its tortuosity.

The total effective diffusion coefficient $D_{eff}$ was estimated by the Bosanquet interpolation formula, which is

$$\frac{1}{D_{eff}} = \frac{1}{D_{12_{eff}}} + \frac{1}{D_{k_{eff}}} \qquad \text{(A2)}$$

With the use of the above relations the effective diffusion

coefficient of $SO_2$ in alkalized alumina pellets was calculated at 300°C and at 500°C under the following conditions: $p_t$=1.0 atm, $\theta$=0.6, $\tau$=3 and $r_e$=200 A. The results are:

| | 300°C ($cm^2\ sec^{-1}$) | 500°C ($cm^2\ sec^{-1}$) |
|---|---|---|
| $D_{12}$ | 0.387 | 0.606 |
| $D_k$ | 0.057 | 0.062 |
| $D_{eff}$ | 0.006 | 0.0068 |

ESTIMATION OF EFFECTIVENESS FACTOR FOR PORE DIFFUSION

The extent to which a diffusion effect is present is represented by an effectiveness factor $\eta$, which is the ratio of the average reaction rate within the pore to the maximum rate if pore diffusion is absent. This can be calculated from the Thiele modulus,[1] but this relation requires knowledge of the rate constant $k_v$, which is frequently unknown explicitly. To formulate a parameter containing only quantities that can be observed or calculated, the observed rate of disappearance of $SO_2$ is expressed as

$$-\frac{dn}{dt} = k_v v_c c_s \eta \quad \left[\text{moles/sec}\right] \tag{A3}$$

for the first order $SO_2$ reaction. $k_v$ is eliminated by solving this relation with the equation for the Thiele modulus. This yields a new dimensionless modulus defined as

$$\Phi = \frac{R^2}{D_{eff}} \left(-\frac{1}{v_c}\frac{dn}{dt}\right) \frac{1}{c_s} = \phi_s^2 \eta \tag{A4}$$

Assuming an isothermal solid particle, $\eta$ was estimated from a published[2] plot of $\eta$ versus $\Phi$. The effectiveness factor at one of the fastest rates, 500°C and at 0.025 atm $SO_2$, was found to be between 0.8 to 0.9. At all other conditions in our investigation the effectiveness factor would be closer to 1 for alkalized alumina.

When experimental data are available for two particle sizes, the effectiveness factor can be determined without knowledge of $k_v$ or $D_{eff}$. The ratio of the rates per unit volume of particle on the two particle sizes as determined experimentally is $\eta_{small}/\eta_{large}$. The ratio of the pellet is $\Phi_{small}/\Phi_{large}$. With the aid of $\eta$ vs. $\Phi$ plots these could be solved by successive approximations. This is done by initially assuming that $\eta_{small}=1$ for the smaller particle, and calculating $\eta_{large}$ for the larger particle. From the plot then, $\Phi_{large}$ is found and $\Phi_{small}$ is calculated from that. With the new value of $\Phi_{small}$, $\eta_{small}$ is found from the plot. Using the rate data for 8-10 mesh and -100 mesh particles at 300°C and at 0.003 atm of $SO_2$, their effectiveness factors were calculated and found to be between 0.8 and 0.9 for the 8-10 mesh particles and between 0.9 and 1 for the -100 mesh particles.

## ESTIMATION OF TEMPERATURE EFFECT ON EFFECTIVENESS FACTOR

The sulfation of sodium oxide is exothermic. A relationship relating the temperature and concentration of the reactant may be derived by considering a boundary surface surrounding some portion of the porous structure. Under steady state conditions, diffusion of the reactants across the surface equals the rate of reaction within the surface. The reaction heat must all be transferred across the same boundary. Hence,

$$D_{eff} \frac{dc}{dR} \cdot \Delta H = \lambda \frac{dT}{dR} \qquad \text{(A5)}$$

or in integrated form

$$\Delta T = T_i - T_s = \frac{(-\Delta H)(D_{eff})}{\lambda} (c_i - c_s) \qquad \text{(A6)}$$

where $T_i$ is the temperature at any point within the particle, $c_i$ (moles/$cm^3$) is the concentration of the reactant at that point, $\Delta H$ is the enthalpy of the reaction, and $\lambda$ is the thermal conductivity of the porous solid. From this a parameter $\beta$ is formulated which is the maximum temperature difference that can exist between the particle surface and the interior.

$$\beta = \frac{c_s(-\Delta H)\, D_{eff}}{\lambda T_s} = \frac{\Delta T_{max}}{T_s} \qquad \text{(A7)}$$

From the values given by Sehr[3] the thermal conductivity is estimated to be $5 \times 10^{-3}$ cal $sec^{-1}$ $cm^{-1}$ $^oK^{-1}$. At a temperature of 500°C, the factor $\beta$ for the sulfation of $Na_2O$ is 0.00042. Since $\beta = \Delta T_{max}/T_s$, the maximum temperature difference that could exist between the particle surface, and interior under any conditions, is about 0.4°C. Consequently, the assumption of isothermal operation is valid.

NOMENCLATURE

| | |
|---|---|
| $c$ | concentration of diffusing reactant |
| $c_i$ | concentration of reactant inside the particle at point i - (gm-moles·cm$^{-3}$) |
| $c_s$ | concentration of reactant at outside particle surface - (gm-moles.cm$^{-3}$) |
| $D_{12}$ | bulk diffusion coefficient of species 1 in a mixture of species 1 and 2 - (cm$^2$.sec$^{-1}$) |
| $D_K$ | Knudsen diffusion coefficient for a straight round pore - (cm$^2$.sec$^{-1}$) |
| $D_{eff}$ | total effective diffusion coefficient for a porous solid - (cm$^2$.sec$^{-1}$) |
| $D_{12_{eff}}$ | effective bulk diffusion coefficient for a porous solid - (cm$^2$.sec$^{-1}$) |
| $D_{K_{eff}}$ | effective Knudsen diffusion coefficient for a porous solid (cm$^2$.sec$^{-1}$) |
| $\Delta H$ | enthalpy change on reaction - (cal.mole$^{-1}$) |
| $k_v$ | intrinsic reaction rate constant per unit volume of the pellet - (sec$^{-1}$) |
| M | molecular weight |
| $-dn/dt$ | rate of disappearance of $SO_2$ - (moles sec$^{-1}$) |
| $r_e$ | equivalent radius of pore - (cm) |
| R | radius of the pellet - (cm) |
| T | temperature - ($^oK$) |
| $T_s$ | temperature at outside surface of particle - ($^oK$) |
| $\Delta T_{max}$ | maximum temperature difference within the particle - ($^oK$) |
| $T_i$ | temperature inside the particle at point i - ($^oK$) |
| $v_c$ | particle volume - (cm$^3$) |
| $\theta$ | void fraction |
| $\beta$ | dimensionless parameter, see Eq. (A7) |

## REFERENCES

(1) Thiele, E.W. Ind. Eng. Chem., 31:916, 1939.

(2) Satterfield, C.N. and T.K. Sherwood. The Role of Diffusion in Catalysis. Addison-Wesley Publishing Co., Inc., 1963. p. 66-69.

(3) Sehr, R.A. Chem. Eng. Sci., 9:145. 1958.